# THE DEFORMATION BEHAVIOR OF A MULTI-LAYERED ALUMINUM CORRUGATED STRUCTURE AT INCREASING IMPACT VELOCITIES

**A Thesis Submitted to**
**The Graduate School of Engineering and Sciences of**
**İzmir Institute of Technology**
**in Partial Fulfilment of the Requirements for the Degree of**

**MASTER OF SCIENCE**

**in Mechanical Engineering**

**by**
**Mustafa Kemal SARIKAYA**

**December 2017**
**İZMİR**

We approve the thesis of **Mustafa Kemal SARIKAYA**

**Examining Committee Members:**

_____

**Prof. Dr. Mustafa GÜDEN**
Department of Mechanical Engineering, Izmir Institute of Technology

_____

**Prof. Dr. Hasan YILDIZ**
Department of Mechanical Engineering, Ege University

_____

**Assoc. Prof. Dr. İzzet ÖZDEMİR**
Department of Civil Engineering, Izmir Institute of Technology

**5 December 2017**

_____

**Prof. Dr. Mustafa GÜDEN**
Supervisor, Department of
Mechanical Engineering
İzmir Institute of Technology

_____

**Prof. Dr. Alper TAŞDEMİRCİ**
Co-Supervisor, Department of
Mechanical Engineering
İzmir Institute of Technology

_____

**Prof. Dr. Metin TANOĞLU**
Head of the Department of
Mechanical Engineering

_____

**Prof. Dr. Aysun SOFUOĞLU**
Dean of the Graduate School of
Engineering and Sciences

# ACKNOWLEDGEMENTS

I would like to thank to my supervisor Prof. Dr. Mustafa GÜDEN for accepting me to his research team, instructive comments, trust, encouragement and support during the entire thesis study. Secondly, thank to my co-supervisor Prof. Dr. Alper TAŞDEMİRCİ for his supports. I would also thank to Dr. Cenk KILIÇARSLAN who works in Norm Civata A.Ş. for his technical support and contributions to my thesis study.

Thanks to all members of Dynamic Testing and Modelling Laboratory; Kıvanç TURAN, Alper ÇANKAYA, Erkan GÜZEL, Fırat TÜZGEL, Semih Berk SEVEN, Çetin UYSAL, Fulya AKBULUT, İlker CANBAZ, Mesut BAYHAN, Sevkan ÜLKER, Muhammet ÇELİK and Doğuş ZEREN for their endless supports and associations.

Last but not least, I would like to express my deepest and sincere gratitude to my family, my father Tayyip SARIKAYA, my mother Ayten SARIKAYA, my older brother Dr. Şakir SARIKAYA, my aunt Prof. Dr. Fatma Süreyya CEYLAN, my uncles Kubilay SARIKAYA, Hasan AHAT(deceased) and Mustafa SARIKAYA(deceased).

# ABSTRACT


## THE DEFORMATION BEHAVIOR OF A MULTI-LAYERED ALUMINUM CORRUGATED STRUCTURE AT INCREASING IMPACT VELOCITIES

The compression impact deformation of a layered 1050 H14 aluminum corrugated sandwich structure was determined both experimentally and numerically under low, intermediate and high velocities to investigate the validity of the perfect and imperfect models. Three-dimensional finite element models of the tested specimens were developed using the LS-DYNA. At increasing velocities from quasi-static velocity to 200 m $s^{-1}$, the tested corrugated structures showed three distinct deformation modes: between 0.0048 and 22 m $s^{-1}$ the deformation was quasi-static homogenous mode; between 22 and 60 m $s^{-1}$ a transition mode and above 90 m $s^{-1}$ a shock mode. These observations were also confirmed by the camera records and model layer strain profiles. The imperfect models predicted the deformation behavior in homogeneous and transition modes, while the imperfect and perfect models both well predicted the shock mode. Layer strain profiles showed that as the velocity increased, the crushed layer densification strains increased. The numerical models and experiments of direct impact tests showed that distal end crushing stress increased with increasing velocity. The increase of the stress within the homogeneous and transient mode velocities was ascribed to the micro-inertia effect and the tested corrugated structure showed a Type II behavior. The rigid perfectly plastic locking (r-p-p-l) model prediction using quasi-static plateau stress and densification strain and quasi-static plateau stress and numerically determined densification strain at that specific velocity resulted higher velocities and full densification, while the r-p-p-l model based on varying plateau stress and densification strain well predicted in the shock mode.

# ÖZET

## ÇOK KATMANLI VE KATLANMIŞ ALÜMİNYUM BİR YAPININ ARTAN DARBE HIZLARINDA DEFORMASYON DAVRANIŞI

Katmanlı 1050 H14 alüminyum dalgalı sandviç yapının basma darbe deformasyonu hem mükemmel hem de kusurlu modellerin geçerliliğini araştırmak için düşük, orta ve yüksek hızlarda deneysel ve nümerik olarak belirlendi. Test edilen örneklerin üç boyutlu sonlu elemanlar modeli LS-DYNA kullanılarak geliştirildi. Yarı statik hızdan 200 m $s^{-1}$'ye yükselen hızlarda, test edilen dalgalı yapılar üç farklı deformasyon modu göstermiştir: 0,0048 m $s^{-1}$ ve 22 m $s^{-1}$ arasındaki deformasyon, yarı statik homojen mod; 22 m $s^{-1}$ ve 60 m $s^{-1}$ arasında geçiş modu ve 90 m $s^{-1}$'in üzerinde bir şok modudur. Bu gözlemler, kamera kayıtları ve model katman gerinim profilleri ile de doğrulanmıştır. Kusurlu modeller, homojen ve geçiş modlarında deformasyon davranışını öngörürken, şok modunda kusurlu ve mükemmel modellerin her ikisi de iyice tahmin edilmiştir. Katman deformasyon profilleri, hız arttıkça ezilmiş tabaka densifikasyon gerinimlerinin arttığını gösterdi. Direkt darbe testi nümerik modelleri ve deneyleri uzak uç çarpışma geriliminin hız arttıkça arttığını gösterdi. Homojen ve geçici mod hızlarındaki gerilim artışı, mikro atalet etkisine bağlıydı ve test edilen katmanlı yapı Tip II davranışı gösterdi. Yarı statik plato gerilimi ve densifikasyon gerinimi ve yarı statik plato gerilimi ve belirli bir hızda sayısal olarak belirlenen densifikasyon gerinimi kullanan katı mükemmel plastik kilitleme (r-p-p-l) modeli tahmini, daha yüksek hızlara ve tam densifikasyona neden olurken, değişen plato gerilimi ve densifikasyon gerinimine dayanan r-p-p-l modeli şok modunda iyice öngörüldü.

# TABLE OF CONTENTS

# LIST OF FIGURES

**Figure** **Page**

# LIST OF TABLES

**Table** **Page**

# CHAPTER 1

# INTRODUCTION

The experimental and numerical studies on the dynamic deformation of metallic cellular structures have shown three distinct, sequential deformation modes at increasing velocities [1-4]. In the quasi-static and low velocity range, the structure deforms by random, discrete, non-contiguous crush bands, which is called quasi-static mode. The initial crushing in quasi-static mode starts at the weakest region of cellular structure and the initial peak or crushing stress is prone to the imperfections [5]. The stresses at the impact (proximal) and distal (rear) end are almost equal to each other. For that reason, this mode is also referred as to a homogenous mode. At the intermediate velocities, the crush bands form near the impact end rather than the distal end, while the progress of the crush band is not planar. The local crush band strain in this transition mode is diffusive and less than the densification strain. The densification strain is the critical strain in the quasi-static stress-strain curve of a cellular material, after which the stress increases sharply following an almost constant stress long plateau region. Above a critical velocity, the cellular structure deforms by forming sequential, planar crush band propagating from the impact end [4, 6]. This is known as the shock mode and was previously observed in the impact testing wood [7, 8], urethane foam [9], aluminum foam [6, 10], aluminum honeycomb [4] and multilayer corrugated structures [11]. The stress developed at the impact end in this mode is far greater than that at the distal end and increases with increasing impact velocity. The stain in the crush bands is at or above the densification strain. The stress enhancement above the critical velocity is attributed to the inertia caused by the strain localization associated with shock formation at the impact end. The stress enhancement below the critical velocity was ascribed to the Type-II micro inertia, which was reported to be relatively weak above the critical velocity [3, 6, 12, 13]. The recent studies have also shown that the densification strain increases with increasing impact velocity as similar with the stress [4, 14-17]. The strains in the crush bands are either measured from the deformation images [15, 16] or numerically determined in the crush band [4].

The experimental and numerical studies on the metallic cellular structures have been mostly on aluminum open and closed cell foams [10, 12, 18-26] and aluminum honeycombs [1, 2, 4, 27-31]. One problem with testing Al foams is that the dispersion in the strength measurement is relatively high, up to 20%, and may cover the increase in strength at increasing strain rates/velocities [23]. This puts a difficulty in differentiating the strain rate effect form the intrinsic strength of structure. The modelling cellular structures is also problematic as the numerical models are usually constructed with the perfect geometry, but the real structure has random or local imperfections/defects or irregularities in the cells. The presence of imperfections tends to reduce the bending and buckling stresses, as a result, the perfect models overestimate the stiffness and strength values. To account the imperfections various methods have been numerically implemented including distortion in the mesh, node shaking, pre-buckling of cell walls, modelling the actual size of the cell wall [32], implementing random mechanical properties [33] and deflection in the truss strut [5]. The effects of imperfections on the crushing behavior of aluminum foams [34, 35] and honeycombs [36, 37] were previously investigated; however, their effects on the response of multi-layered cellular structures at increasing velocities have not been fully explored.

The aim of present study was to investigate both experimentally and numerically the deformation of a multi-layered 1050 H14 aluminum corrugated sandwich core structure under low, intermediate and high velocities. The validity of the investigated perfect and imperfect models as function velocity and layer crush sequences were also determined. The investigated sandwich corrugate core structure differs from the previously investigated corrugated cores in that it was made of multi corrugated layers (fins). The structure was previously shown to exhibit repeatable responses to mechanical forces under compression at both low and high velocities [11, 38, 39]. This allows accurate determination of the effect of strain rate on the mechanical properties. More importantly, the homogeneous layers of a multi-layered structure make it possible to construct 3D full models in order to monitor the velocity and strain histories of each layer during the course of deformation.

In the thesis, four different tests were performed and the test results were compared with the model results. The quasi-static compression test was performed at ~$5x10^{-3}$ $s^{-1}$; the Split Hopkinson Pressure Bar (SHPB) tests were performed between 6 and 10 m $s^{-1}$; the direct impact tests were performed between 9 and 90 m $s^{-1}$ and the Taylor-like impact tests were performed at 135, 150 and 200 m $s^{-1}$. Three-dimensional

finite element models of the tested specimens were developed using the LS-DYNA. The stress-time histories of the tests were verified by the simulations in the explicit finite element code of LS-DYNA. The perfect geometry model was coded as perfect model I, the fully bent fin wall model coded as perfect model II, the model with one layer bent fin coded as one layer imperfect model and the model with two layers of bent fin layers coded as two layer imperfect model. The validities of the implemented two perfect and two imperfect models were discussed along with the deformation velocity, high speed camera records and stress-time profiles.

In the thesis, the quasi-static and high strain rate compression deformation of cellular metals are given in Chapter 2. Chapter 3 is on the materials and tests and Chapter 4 gives the details of the models implemented. The results of tests and models are given in Chapter 5. And, finally the results are discussed in Chapter 6 and the conclusions are made in Chapter 7.

# CHAPTER 2

# DEFORMATION OF CELLULAR METALS

## 2.1. Cellular Structures

Cellular metal structures are made of regularly arranged and homogeneously distributed cells and have multifunctional features such as high energy absorption and heat dissipation [40-44]. As with other light-weight structures, cellular metal structures exhibit relatively high bending strength to weight ratios [41] and relatively high resistances to frontal impacts as compared with equal-mass monolithic panels, when used as cores in sandwich panels [45]. Cellular metal structures are classified in two main groups of random and periodic as shown in Figure 2.1 [42]. Examples to random cell structures include open and closed cell metal alloy foams in which the cell size and the geometry vary with the location, inherited from the manufacturing routes used to produce them. The periodic metallic cellular structures encompass honeycombs, corrugated (prismatic) and lattice truss structures, Figure 2.1. Typical lattice truss topologies include tetrahedral, pyramidal, kagome, diamond textile, diamond collinear and square collinear [43]. The repeating unit topology may be in 2D, as in the case of honeycomb, or in 3D, as in the case of lattice truss. Honeycomb structures have high out-plane compression and transverse shear strength; therefore, they are widely used for designing with light weigh sandwich panels as cores. These structures allow the fluid flow only in one direction. The lattice truss structures exhibit high bending stresses and stretch-dominant deformation behavior. These structures allow 3D fluid flow through the sandwich panels when used as cores.

Corrugated structures are relatively cheap materials. They are widely used in the building and ship construction. The corrugation may be straight, trapezoidal, triangular and curvilinear as seen in Figure 2.2. Each topology has geometry-specific response to mechanical loads as well as the direction of the loading. A multilayer form is also possible by applying appropriate joining processes of corrugated layers such as brazing and bonding. The investigated multi-layer corrugated structure in this thesis has a zig-zag form which enables the fluid flow in 3D. The multi-layering transforms

the compression deformation mechanism from global bending of a single layer [46] to the progressive crushing of multi layers as similar with foam metals [11 , 38, 39, 47].

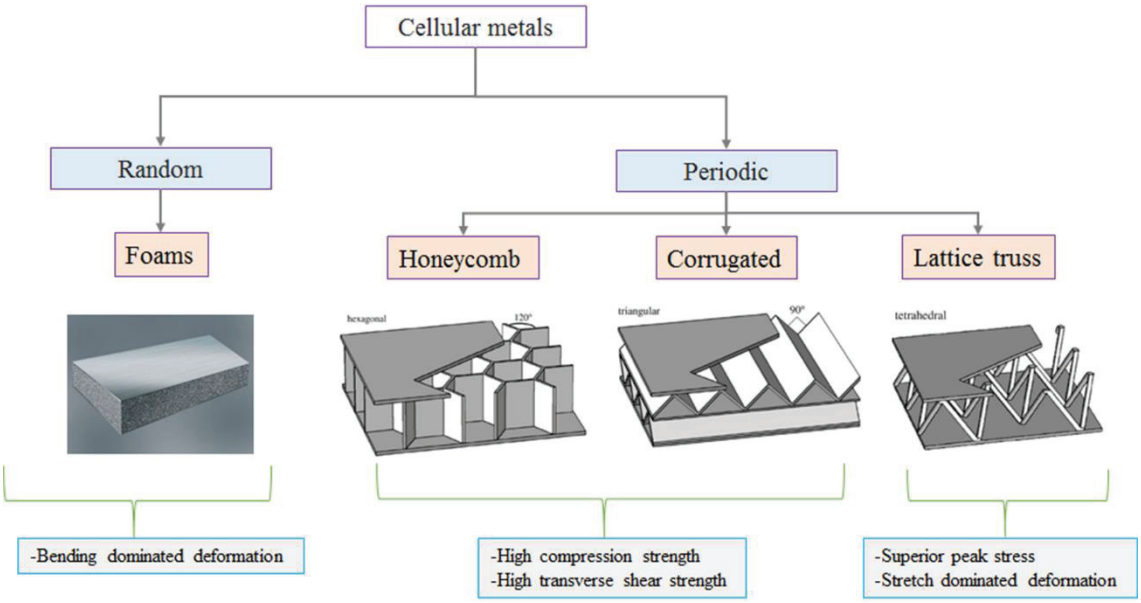


Figure 2.1. Broad classification of cellular metals (honeycomb, corrugated and lattice structure pictures) are taken from [27]

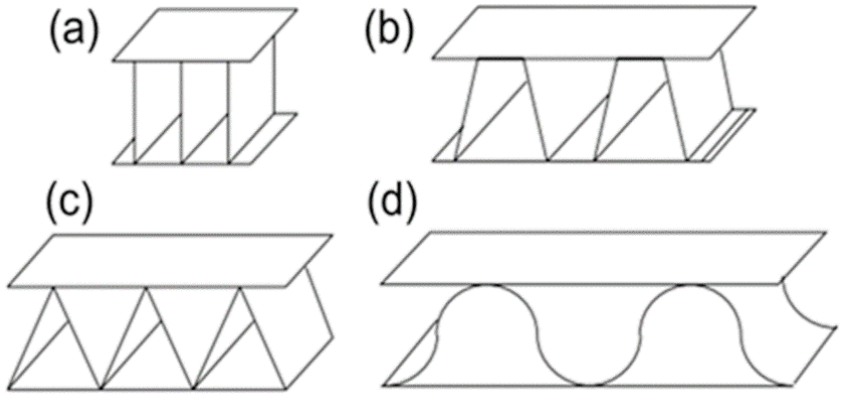


Figure 2.2. Examples to corrugated topologies: (a) straight, (b) trapezoidal, (c) triangular and (d) curvilinear

## 2.2. Quasi-Static Compression Behavior Metal Foams

The cellular metals show characteristic stress-strain behavior under compression. A typical stress-strain curve composes of three sequential distinct deformation regions: (i) linear elastic, (ii) plateau and (iii) densification [40] as depicted in Figure 2.3. In the linear elastic region, the cellular material deforms elastically until about a crushing stress($\sigma_{cr}$).

Following the crushing stress, the localized deformation in the form of cell wall bending and/or stretching starts. When the cells in a local region collapse, a deformation band or crush band forms. The initial collapse of the cells leading to the formation of a crush band at quasi-static strain rates starts in a region weakest in strength [23], then progresses to the uncrushed sections. The crush bands may be sequential, i.e. the crush band jumps to the neighboring cells, or discrete, i.e. the crush band jumps to the sections far from the initially formed crush band. The discrete bands are commonly observed at low velocities, while sequential bands are observed above a critical velocity at which a shock deformation occurs. The progression of the deformation bands throughout the cellular structure with increasing strain may result in stress oscillations between peak and valley stresses, which correspond to the start and end of a deformation band, respectively. This region of cell crushing is called plateau region. The stress in the plateau region is known as plateau stress ($\sigma_p$) (Figure 2.3). The crushing of metallic cellular materials in the plateau region is dominated by the cell wall buckling and stretching. After the crush of all cells in the form of crushing bands, the material starts to densify at a critical strain known as densification strain ($\varepsilon_d$). In the densification region, crushed layers are compressed together, leading to an abrupt increase in the stress. The imperfections in the cellular structure such as density variations, cell wall curvature and cell wall corrugations tend to decrease the crushing and plateau stress [48].

## 2.3. Dynamic Deformation of Cellular Structures

Wu and Jiang in 1997 [49] experimentally investigated the quasi-static and impact loading (10 and 20 m $s^{-1}$) behavior of an aluminum honeycomb through out-of-plane. Stress enhancement up to 74% was observed in the crushing stress of the dynamically loaded samples (Figure 2.4(a)). The stress enhancement was found to be proportional to the initial striking velocity of blunt projectiles (Figure 2.4(b)).

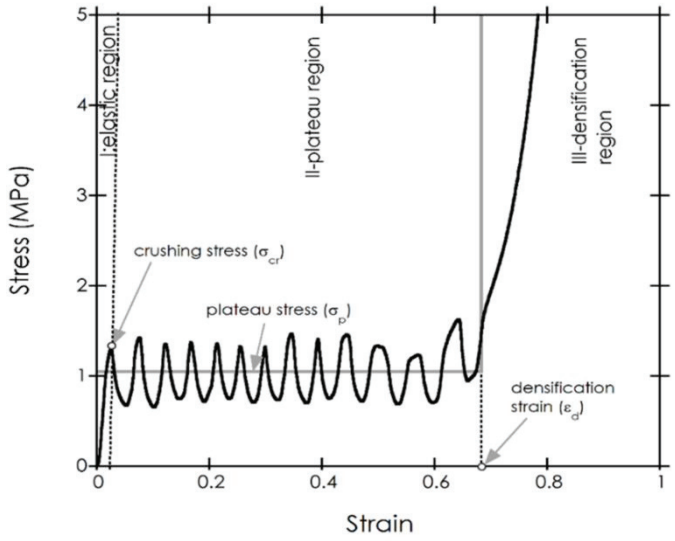


Figure 2.3. Quasi-static stress-strain behavior of a cellular metal

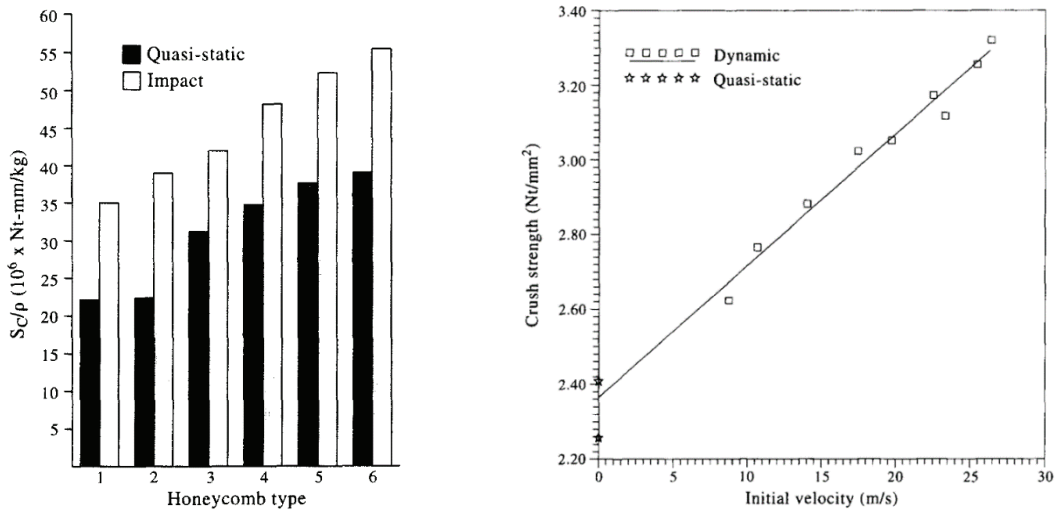


(a) (b)

Figure 2.4. (a) the areal crushing strength of the tested 6 honeycombs under quasi-tatic and impact loads and (b) the variation of crushing strength with the initial impactor velocity [49]

Zhao and Gary [27] investigated the out-of-plane and in-plane quasi-static and dynamic (2, 10 and 28 m $s^{-1}$) compression behavior of an aluminum honeycomb. The dynamic mean crushing stress in out-of-plane direction showed 40% increase as compared with the quasi-static mean crushing stress (Figure 2.5(a)), while no stress enchantment was detected in the samples tested in the in-plane-direction within the studied velocity range (Figure 2.5(b)). The densification strain was found to be independent of velocity at directions both out-of-plane and in-plane.

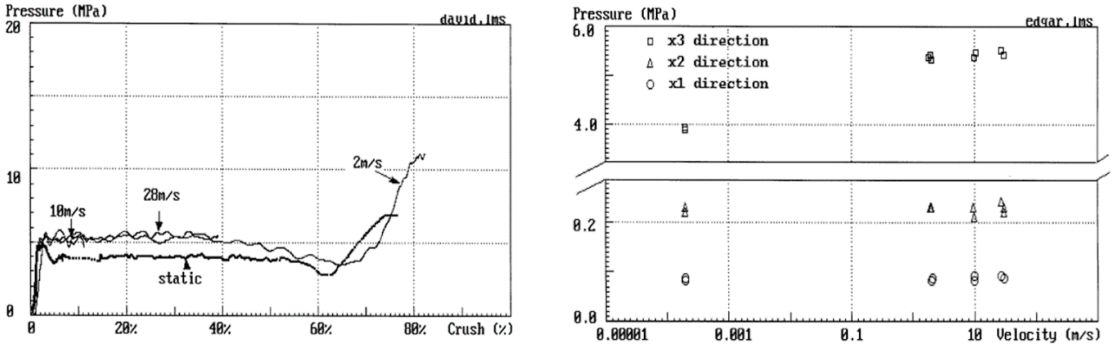


(a) (b)

Figure 2.5. (a) stress-strain curve in out-of-plane direction and (b) stress-velocity graph of out-of-plane (x3) and in-plane (x2 and x1) of an aluminum honeycomb

Harrigan et. al. [50] direct impact tested (up to ~300 m $s^{-1}$) a 5050 Al honeycomb with and without aluminum backing mass and with and without lateral confinement in the out-of-plane direction. The initial crushing and plateau stresses were shown to increase with increasing impact velocity (Figures 2.6(a) and (b)). The increase in the initial peak stress (initial crushing stress) was reported to be governed by uniaxial plastic wave effect, while the increase in the plateau stress was well-predicted by rigid perfectly plastic locking (r-p-p-l) model developed by Reid and Peng in 1997 [7] (Figures 2.7(a) and (b)). It was also noted that full-confinement had no effect on the stress enhancement, while the samples tested with backing was showed slightly higher stresses than the samples tested without backing disc due to the inertial effects. The presence of initial stress pike in the dynamic loading of the pre-crushed samples tended to conclude that the initial stress pike was due to inertia.

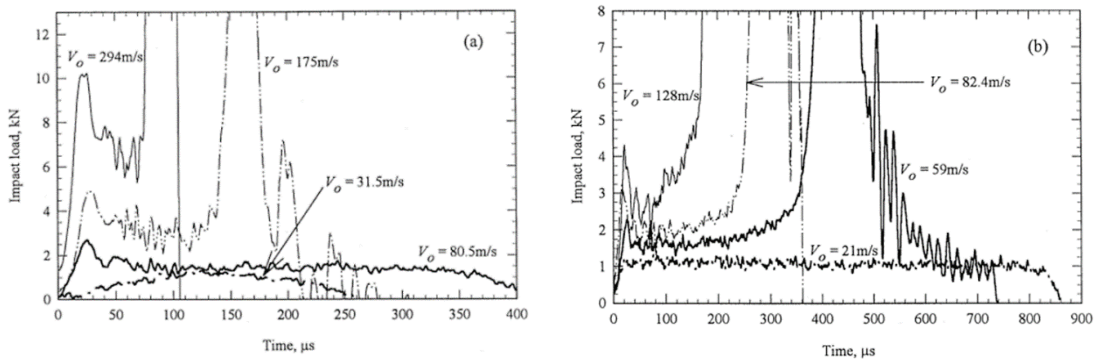


(a) (b)

Figure 2.6. Force vs. time graphs of pre-crushed honeycomb specimens: (a) laterally free specimens without backing masses and (b) laterally free specimens with backing masses [50]

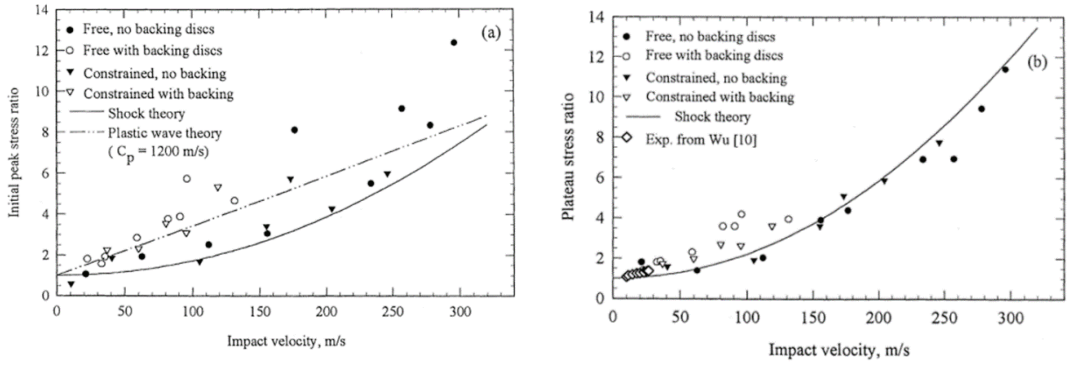


(a) (b)

Figure 2.7. Comparisons between the shock theory (r-p-p-l model) and the experiments (a) initial peak stress ratios of uncrushed honeycombs and (b) plateau stress ratios of uncrushed honeycomb [50]

The high strain rate compression behavior of cellular aluminum alloys (Alulight and Duocel) were investigated by Deshpande and Fleck in 2000 [23] between $10^{-3}$ and 5000 $s^{-1}$. The dynamic stress was determined by the SHPB compression and direct impact tests. The direct impact tests were performed at the velocities less than 50 m $s^{-1}$ (Figure 2.8(a)). Almost no increase in the plateau stress was observed within the investigated strain rate interval (Figure 2.8(b)). In the direct impact tests, the measured impact and distal end stresses were nearly equal to each other, showing that shock wave did not form in these tests. The deformation was found to procced as weak bands in the Alulight foam but it was spatially uniform in the Duocel foam.

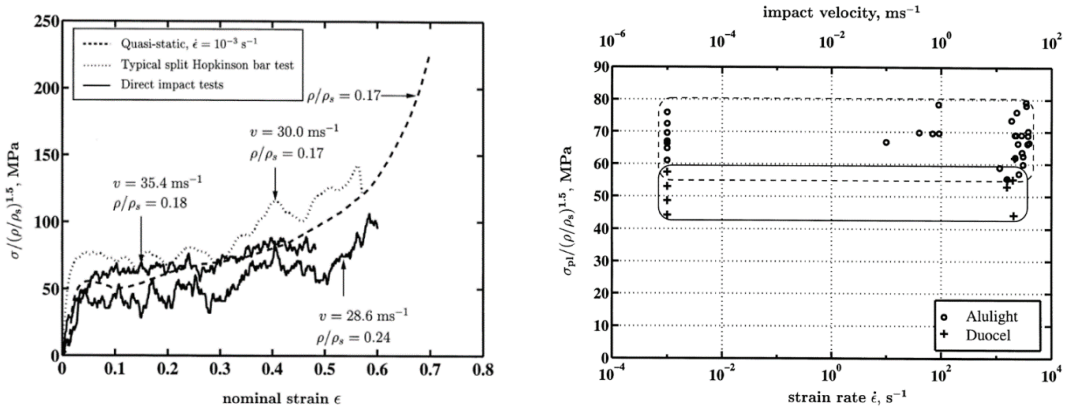


(a) (b)

Figure 2.8. (a) stress-strain responses of Alulight foam from quasi-static to high strain rates (30 m $s^{-1}$ corresponds to an average strain rate of 3000 $s^{-1}$ and (b) the variation of plateau stress with strain rate for Alulight and Duocel foams [23]

Hall et. al. [51] performed quasi-static ($10^{-3}$ $s^{-1}$) and high strain rate (up to 2000 $s^{-1}$) SHPB compression tests on a closed cell 6061-Al alloy foam processed by a powder

metallurgical method. No effect of strain rate on the compression stress of the foam was detected within the studied strain rate regime (Figure 2.9(a)). Metallographic observations confirmed that the deformation proceeded with progressive cell wall collapse, including cell wall buckling and tearing modes (Figure 2.9(b)).

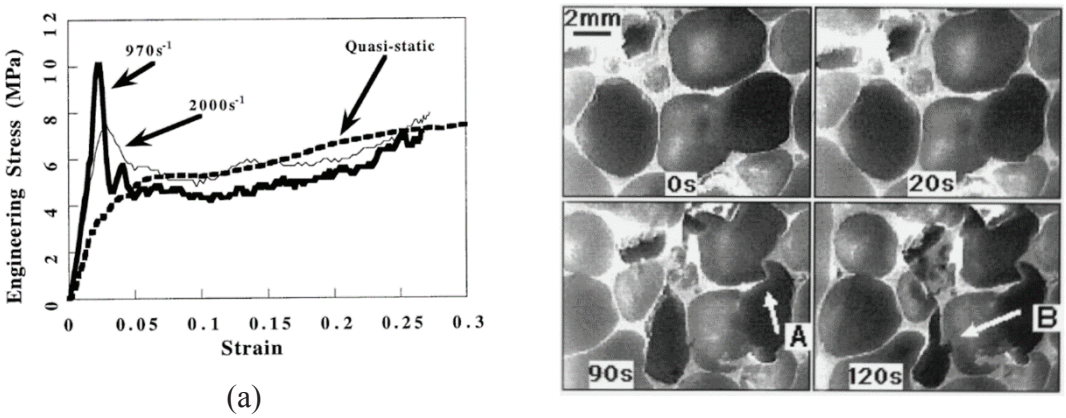


(a) (b)

Figure 2.9. (a) stress-strain responses of 6061 Al foam from quasi-static to high strain rates (2000 $s^{-1}$) and (b) the cell wall failure A: bending and B tearing [51]

Honig and Stronge [52] conducted FE analysis on the crush band initiation and wave trapping in the impact of an aluminum honeycomb in in-plane direction. The determined stress enhancement with increasing impact speed was shown mainly due to the translational micro-inertia and not due to the micro-rotational inertia. The stress enhancement for a uniaxial stress state was found to start at about 10 m $s^{-1}$. At the velocities above this critical velocity, crush bands initiated at the impact surface, while at lower speeds the location of the initial crush band was determined by the distribution and extent of initial imperfections. Using the theory of wave trapping, the critical impact speed was determined greater than 7.6 m $s^{-1}$ which was close to the critical speed calculated in the finite element simulations.

Radford et. al. [10] direct impact tested Alporas aluminum foam with a relative density of 0.11 between quasi-static velocity and 500 m $s^{-1}$. The velocity dependent peak and mean stresses values were well-fitted with following relation (Figure 2.10(a)),

$$\sigma^* = \sigma_p + \frac{\rho_o}{\varepsilon_d} {v_o}^2 \tag{2.1}$$

where $\sigma^*$ is the peak stresses and $\rho_o$ is the initial density. The mean stress ($\sigma_m{}^*$) however showed a well agreement with the following relation (Figure 2.10(a)),

$$\sigma_m{}^* = \sigma_p + 0.66\frac{\rho_o}{\varepsilon_d}{v_o}^2 \tag{2.2}$$

The arrest time ($\tau$) was shown to be well-fitted with the following relation. (Figure 2.10(b)).

$$\tau = \frac{\varepsilon_d l_o}{v_o} \tag{2.3}$$

where, $l_o$ is the initial length of the specimen.

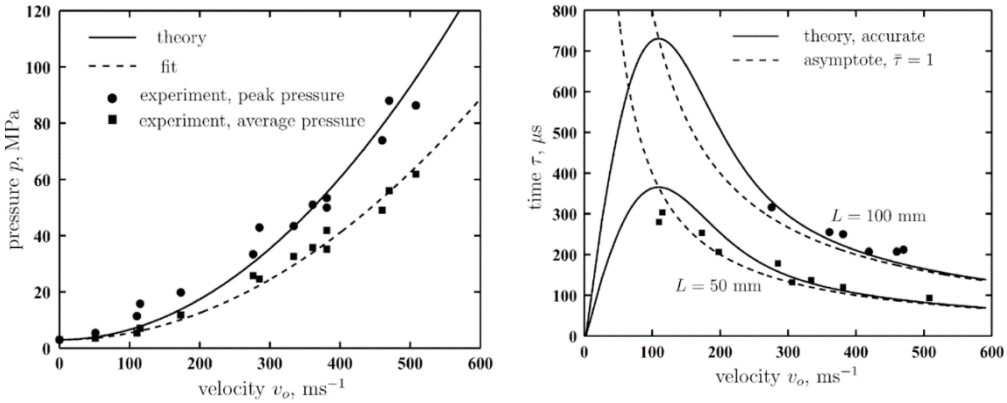


(a) (b)

Figure 2.10. (a) the measured peak and mean pressures of 0.11 relative density Alporas metal foam as a function of the impact velocity and (b) the measured pulse duration as a function of the impact velocity [10]

Tan et. al. [6, 12] direct impact tested (between 10 and 210 m $s^{-1}$) small and large size Hydro/Cymat aluminum closed cell foams and fitted the resultant increase in the crushing strength with the r-p-p-l model. Furthermore, a method for the determination of the densification strain was proposed in the same study based on the maximum energy absorption efficiency. The dynamic deformation was similar to that of the quasi-static at subcritical velocities; the collapse started from the weakest band of cells, usually in interior of the samples, while the cell collapse always started from the impact end and sequentially propagated to the uncrushed sections in a planner manner above the supercritical velocities. A critical velocity for shock deformation ( $v_{cr}$) was proposed based on the thermo-mechanical approach as

$$v_{cr} = \sqrt{\frac{2\sigma_1 \varepsilon_d}{\rho_o}} = \sqrt{\frac{2C_p \sigma_{ys} \varepsilon_d}{\rho_s}} \left(\frac{\rho_o}{\rho_s}\right)^{1/4} \tag{2.4}$$

where, $C_p$ is the plastic wave speed, $\sigma_{ys}$ is the yield strength of cell wall material and $\rho_s$ is the density of cell wall material. The calculated critical velocities for the small and large cell foams, 108 and 41 m $s^{-1}$, were found to be well agreed with the experimentally determined critical velocities. It was shown that both the crushing strength and plateau stress variations with impact velocity were well agreed with the r-p-p-l model (Figures 2.11(a) and (b)), except at 200 m $s^{-1}$. It was proposed that inertial effects associated with the dynamic localization of the crushing were responsible for the enhancement of the dynamic strength properties in the supercritical velocity regime.

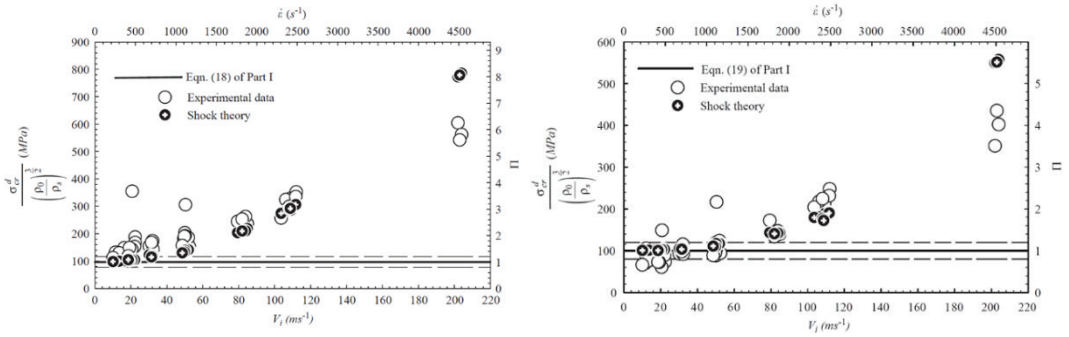


(a) (b)

Figure 2.11. The comparison between theory and experimental data for the normalized plastic collapse stress of small size foam (a) crushing stress and (b) plateau stress [12]

Zhao et. al. [53] experimentally investigated the impact responses of aluminum honeycombs, IFAM and Cymat aluminum foams and nickel and iron hollow sphere agglomerates. The honeycombs, foams and hollow spheres showed velocity dependent stresses, as sequentially shown in Figures 2.12(a-c). Rate insensitive aluminum alloys of honeycombs and IFAM and Cymat foams exhibited a strength enhancement of about 15% (Figures 2.12(d) and (e)) under impact loading. It was further shown that the stress enhancement due to the shock front in the tested cellular materials was experimentally proven to be negligible for impact velocities below 45 m $s^{-1}$. The stress enhancement was therefore attributed to the micro-inertia effect of the successive folding process.

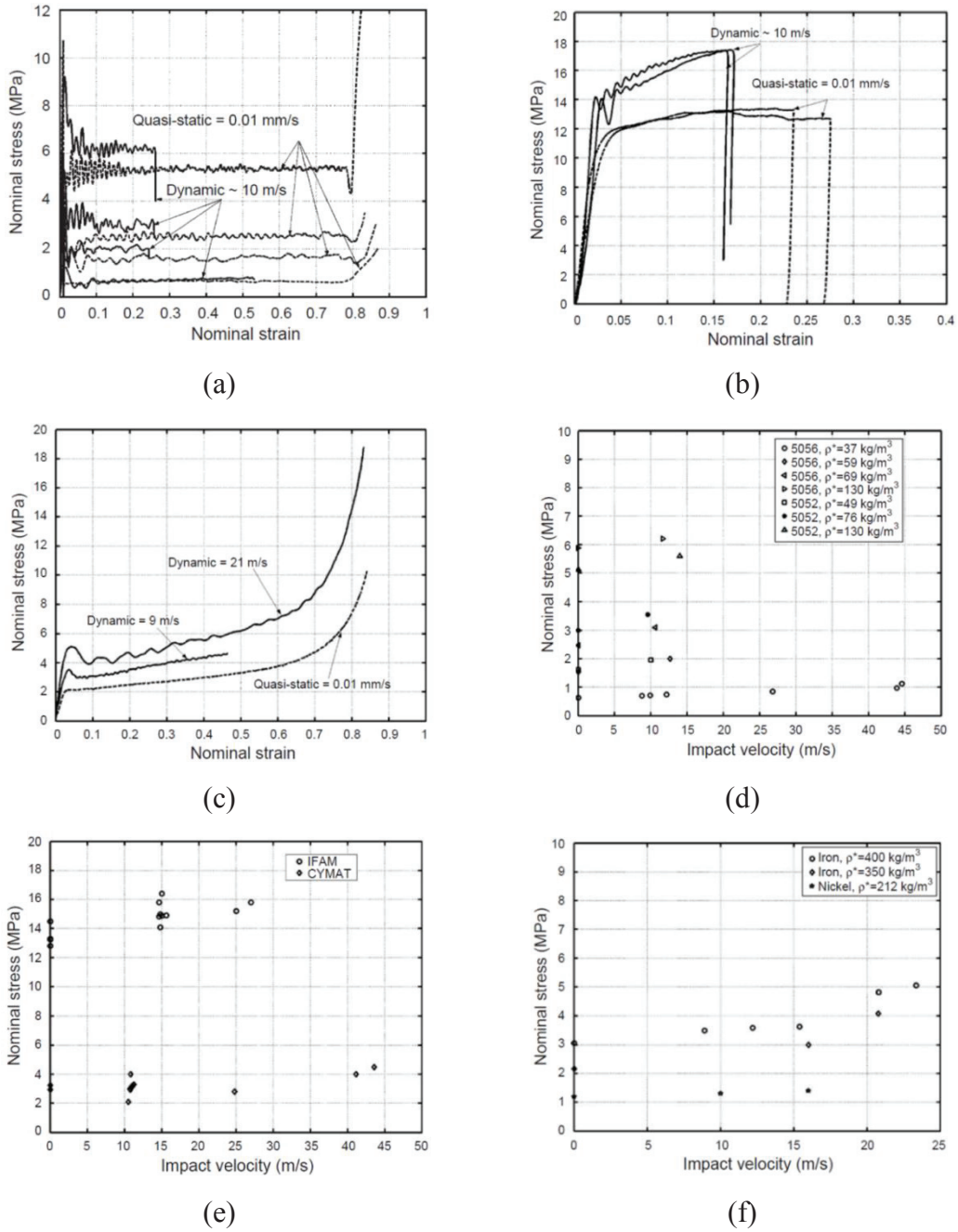


Figure 2.12. The stress-strain curves of (a) 5056 Al honeycomb, (b) IAM foam and (c) iron hollow sphere agglomerates at different velocities and the strength enhancement in (d) Al honeycomb, (e) Al foams and (f) nickel and iron hollow sphere agglomerates [53]

Zheng et. al. [2] investigated the dynamic crushing behavior of 2D cellular structures by FE method including the effect of cell irregularity and impact velocity on the deformation mode and the plateau stress. Three deformation modes depending on the impact velocity were demonstrated in the regular and irregular honeycombs shown in Figures 2.13(a) and (b). These were as follows: 1) at a low impact velocity, the quasi-static mode with the random collapse of weak shear bands, 2) at an intermediate impact

velocity, a transition mode with localized shear bands and transverse bands and 3) at a high impact velocity (where the inertial effects dominated the deformation), a dynamic mode or shock mode with layer-wise collapse of transverse bands.

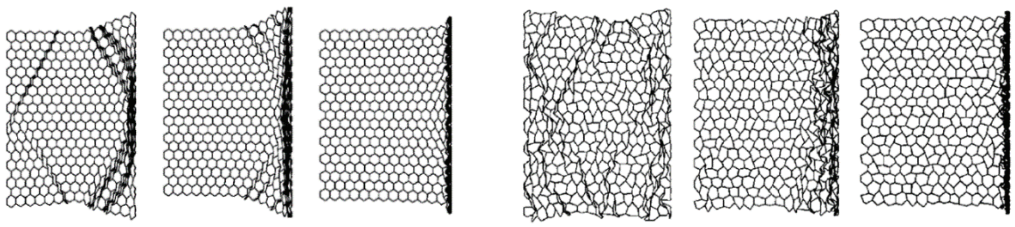

(a) (b)

Figure 2.13. Three patterns of a regular honeycomb crushed in the in-plane direction sequentially in the picture at 5, 20 and 80 m $s^{-1}$; (a) ordered and (b) disordered honeycomb structure

Zhao et. al. [54] investigated the strengthening mechanisms of 5056 and 5052 aluminum honeycombs (out-of-plane) and IFAM and Cymat foams in SHPB up to 14 m $s^{-1}$. Although a strengthening of 15% was found in the impact testing of honeycombs and IFAM foam, no strengthening was found in Cymat foam. The strengthening of honeycombs and IFAM foam was attributed to the micro-inertia effect of the successive folding (Figure 2.14(a)). The rate insensitivity of Cymat foam was ascribed to the cell wall fracture in the compression test (Figure 2.14(b)).

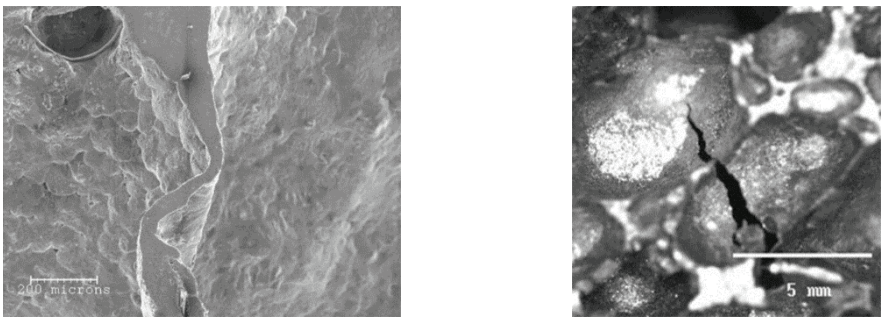


(a) (b)

Figure 2.14. (a) progressive cell wall bending in IFAM foam and (b) cell fracture in Cymat foam [54]

Elnasri et. al. [25] and Pattofatto et. al. [55] experimentally and numerically investigated the dynamic strengthening in Alporas aluminum foam, nickel hollow sphere agglomerates and aluminum honeycomb and Cymat foam up to 55 m $s^{-1}$. In the first test configuration, the sample was inserted in front of incident bar of a SHPB and a projectile impinged the sample (direct impact test) and in the second configuration

the sample with a mass fired to the end of the incident bar (Taylor-like impact test). It was reported that the rate sensitivity of Alporas foam and honeycomb was due to the micro-inertia effects of the successive buckling of the cell walls. The rate sensitivity of Nickel hollow spheres was ascribed to the rate sensitivity of the cell wall material. There was no clear rate sensitivity in Cymat foam.

Liu et al. [3] and Zou et al. [4] performed numerical modelling on the direct impact crushing of 2D Voronoi honeycomb and in-plane dynamic crushing of honeycomb. Three deformation modes were numerically identified at varying crushing speeds. These were (a) homogeneous mode, (b) transition mode and (c) shock mode (Figure 2.16). The effect of micro-inertia was shown to be weak for Voronoi structure at high velocities and the strain rate sensitivity of the cell wall material contributed little to the increased plateau stress at increasing velocities [3]. It was shown that the increased compressive stress in the in-plane direction of honeycomb at increasing impact velocities induced higher densification strains and longer plateau stresses [4]. The densification strain increased as the velocity increased and reached a limit which was 15% higher than that of the quasi-static value when a steady-shock front formed (Figure 2.17(a)). It was also shown that the r-p-p-l model overestimated the crushing stresses (Figure 2.17(b)) [4].

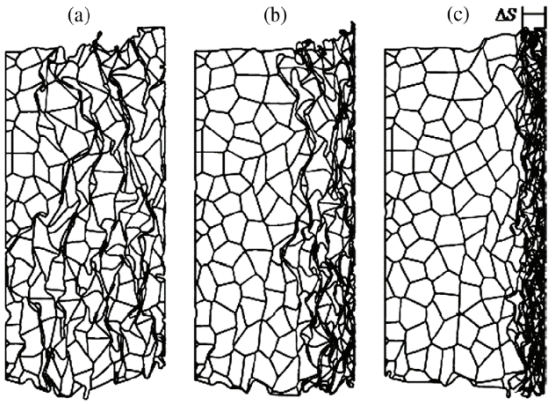


Figure 2.15. Three deformation modes of Voronoi honeycomb (a) homogeneous mode (low velocity), (b) transition mode (medium velocity) and (c) shock mode (high velocity) [3]

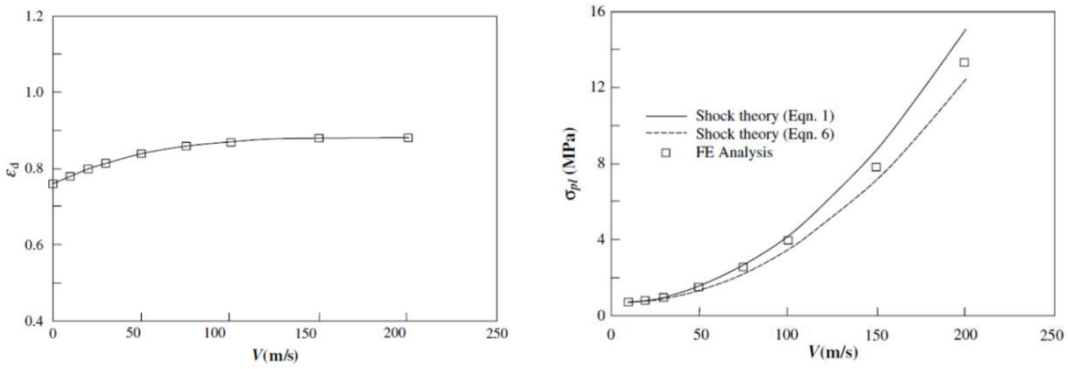


(a) (b)

Figure 2.16. (a) densification strain vs. velocity and (b) comparison of plateau stress with r-p-p-l model (Equation 2.1) in Voronoi honeycomb [4]

Karagiozova et. al. [56] investigated the compaction behavior of cellular materials showing strain hardening under decreasing impact velocities. The numerical results were then verified with the experimental results of Alporas and Cymat Al foams. It was shown that the r-p-p-l model overestimated the energy absorption capacity for the observed stroke. This was due to the non-uniform strains along the compacted zone of the actual material as the r-p-p-l model used a constant densification strain. The assumption of a constant densification strain resulted in an overestimation of the maximum stress.

Zheng et. al. [57] developed continuum based models for the transitional and shock modes in cellular materials. The results showed that for a shock mode the initial strain remained constant and the initial stress varied proportionally with the square of the impact velocity. However, the initial strain and stress behind the front decreased linearly with the reduction of velocity for the transitional mode. The critical impact velocities for transitional and shock modes were determined using rigid-linearly hardening plastic locking model as

$$v_{c1} = \frac{\sigma_{cr}}{9\rho_o C_1} \tag{2.5}$$

and

$$v_{c2} = \varepsilon_d \sqrt{\frac{E_1}{\rho_o}} = \varepsilon_d C_1 \tag{2.6}$$

where $v_{c1}$ is the velocity to the passage to the transitional mode, $v_{c2}$ is the velocity for shock mode and $E_1$ is the hardening modulus.

Liao et. al. [31] developed a method to calculate the local strain field of a deformed cellular structure based on the optimal local deformation gradient using a cell-based finite element model. A comparison between the cell-based finite element model and continuum-based shock model indicated that the shock model based on the post-locking behavior was found more accurate in predicting the shock wave velocity.

Barnes et. al. [15] studied the crushing behavior of open-cell 6061 Al foams in direct and Taylor-like impact tests in the range of 20-160 m $s^{-1}$. The strain behind the shock, densification strain, extracted directly from the high-speed images increased with increasing impact velocity (Figure 2.17(a)). The specimens impacted at 60 m $s^{-1}$ and above showed shock deformation, while the specimens impacted below 40 m $s^{-1}$ showed very similar crushing mode with the specimens tested at quasi-static velocity shown in Figure 2.17(b).

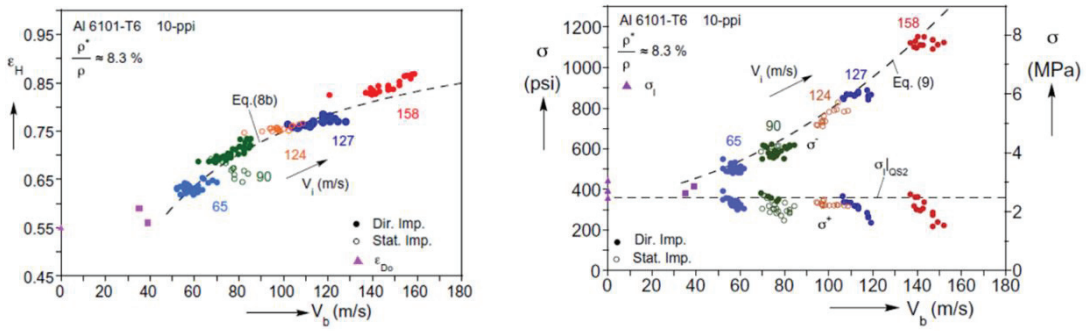


(a) (b)

Figure 2.17. The variations of (a) the strain behind shock wave and (b) the stress behind and front of the shock wave front with the impact velocity [15]

Tao et. al. [30] investigated out of plane quasi-static and dynamic compression behavior of an Al3003 H18 honeycomb up to 19 m $s^{-1}$. Within the investigated velocity range, the plateau stress increased by 38 to 57%. A strain rate dependent r-p-p-l model was shown to well-fitted with the dynamic plateau stress within the investigated strain rate regime. The dynamic plateau stress was divided in three parts; static, inertia and strain rate sensitivity of the cell wall material. It was concluded that the strain rate effect played an important role in the dynamic enchantment of metallic honeycomb at relatively low velocity regime. The lower plateau stress prediction by r-p-p-l model was attributed to the lack of strain rate sensitivity of the cell wall material in the model.

Wang et. al. [58] investigated the dynamic behavior of an aluminum foam at 16, 63 and 113 m $s^{-1}$. The front and distal end stresses of the samples were measured. Three different deformation regions were identified. At 16 m $s^{-1}$, the sample's back and font surface stresses were found to be equal corresponding to the homogeneous mode and at 113 m $s^{-1}$, the front surface stress was higher than that of the back surface showing the inertial effect or shock deformation mode. At the intermediate velocity the transition mode was detected.

## 2.4. Strain Rate Sensitivity of Cellular Metals

The strain rate sensitivity of cellular materials may be due to (1) strain rate sensitivity of cell wall material, (2) entrapped gas pressure, (3) micro-inertia and (4) inertia or shock wave [3, 54]. The rate sensitivity of the cell wall material affects the dynamic crushing stress of the cellular materials at increasing velocities [59-61]. It was shown that the initial peak stress of an Al foam increased with strain rate up to 500 $s^{-1}$ due to micro-inertia, while the plateau stress remained almost constant at increasing strain rates. On the other side, both initial peak stress and plateau stress of a Ni/Al foam increased with strain rate; the latter was attributed to the cell wall material strain rate sensitivity [60]. It was also shown numerically that the effect of strain rate sensitivity of the cell wall material on the dynamic crushing stress diminished as the porosity increased and for practical purpose the effect of rate sensitivity of the cell wall on the crushing stress might be taken negligible for high porosity foams [61, 62].

For Al foams there existed confusing results on the strain rate effect as reported in ref. [3]. The reason is the lack of or very low strain rate sensitivity of Al and Al alloys [63]. Since the cellular structures deform through forming crush bands, it is also difficult to correlate the nominal strain rate with the local strain rate. The local strain rate may be far excess of the nominal strain rate. In the present thesis, the effect of strain rate sensitivity of the cell wall material was not taken into account as the cell wall material was made of 1050 Al and the tested corrugated samples had a low relative density (0.12) as similar with low density Al foams.

The entrapped gas pressure may increase the stress when the loading rate is high due to the limited time for the gas to escape. The upper limit for the increase of the strength with the entrapped gas pressure in an Al foam with a 0.1 relative density was

calculated 0.2 MPa which may be neglected particularly at high velocities [23]. A recent study has however shown that the effect of entrapped gas pressure may contribute to the dynamic strength of a low relative density Al foam (4%) as much as 50% [64]. The use small size and higher relative density foam test samples tends to decrease the entrapped gas pressure effect.

The increased crushing strengths of the cellular structures at increasingly high deformation rates are ascribed to the micro-inertia effects. Calladine and English [65] classified the energy absorbing structures as Type I and Type II. Type I structures show a flat-topped load-displacement curve, while Type II structures shows an initial peak following a softening behavior (Figure 2.19). Tubes deforming along the long axis by forming folding are typical examples to the Type II structures. Figure 2.20 shows the force-displacement and strain rate-displacement of a thin walled (0.3 mm) Al tube 40 mm in length and 20 mm in diameter. The tube is deformed at a lower strain rate ($\sim 10^{-3}$ $s^{-1}$) until about 15 mm displacement; thereafter, the strain rate increases 100 times (approximately $10^{-1}$ $s^{-1}$). A magnification of the force axis clearly shows the micro-inertia effect within the quasi-static strain rate range (shown by arrow shown in Figure 2.19). The Type II structures are found to be more sensitive to impact velocity than Type I structures [65]. The increased deformation forces at increasing deformation rates in the compression of aluminum honeycomb structures through out of plane [53], metallic columnar structures [66], aluminum foams [67] and balsa wood in the axial direction [7, 68] were reported to be resulted from the micro-inertia effects. V-frame corrugated structures were shown to be more inertia sensitive than Y-frame, as the deformation in V-frame structure is the stretching-governed buckling, while in Y-frame core it proceeds with the bending of one of the legs [69]. It was also shown that U-, X- and V-frame cores exhibiting buckling mode of deformation showed higher crushing strengths and energy absorptions than Y-frame cores exhibiting the bending mode of deformation [70]. Tam and Calladine [71] analyzed the deformation of Type II structures based on a rigid-plastic analysis in two phases. The first phase involves the plastic compression of the structure, while the second phase involves the rotations of plastic hinges. It was reported that the inertia was the dominant in the first phase and the strain rate sensitivity was dominant in the second phase. Su et al. [72, 73] proposed an elastic plastic model for the compression of Type II structures and concluded that inertia and strain rate sensitivity were dominant in the entire deformation processes. It was also reported in the same studies that an elastic analysis was necessary in order to determine

the magnitude of the peak load. The corrugated structures tested in the present study also showed inertia-sensitive Type II behavior. The propagation of the plastic wave at high strain rates delays the overall buckling of the member and the member needs to form kinks [74].

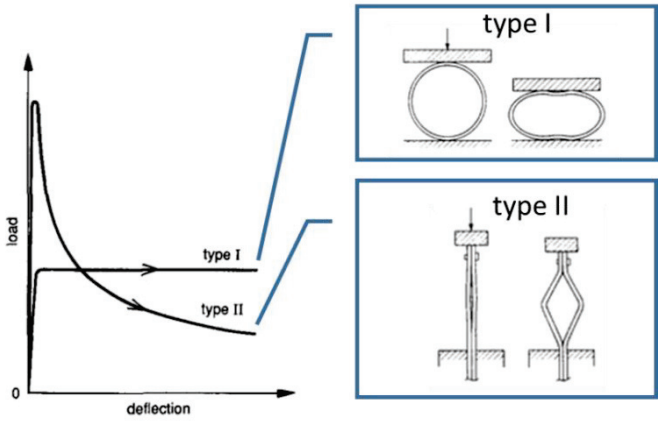


Figure 2.18. Load-displacement curve of type I and type II structures and the schematic deformation modes [65]

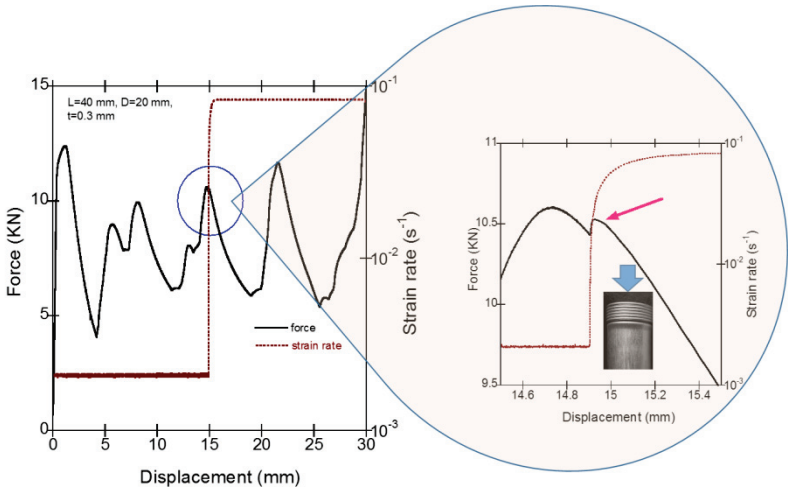


Figure 2.19. The effect of micro-inertia in an Al tube

At relatively high impact velocities, a shock mode occurs. A well-known characteristic of metallic ductile cellular structures is the concave-up rise of the compressive stress after the densification strain. Due to this, the direct and Taylor-like impact tests with and without backing mass result in shock wave initiation and propagation after a critical velocity from the impact end. The shock stresses induces crushing stresses higher than quasi-static crushing stress and the crushing stress increases with increasing velocity above the critical velocity.

The shock wave propagation in cellular materials was initially analyzed by Reid and Peng in 1997 using the r-p-p-l idealization model. The r-p-p-l model assumes a constant plateau stress and a well-defined densification strain. Later, various material models including elastic-perfectly-plastic-rigid [24], elastic and rigid softening hardening [8] and strain hardening models [56] were developed to elaborate the shock wave propagation in cellular materials. The r-p-p-l shock model was previously applied to cellular material including wood (e.g. [8]), aluminum foam (e.g. [6, 10]) and honeycomb (e.g. [4, 50 ]). The model details can be found in refs. [7, 10] and is also given in the next section.

## 2.5. Perfectly Plastic Locking Model for Shock Deformation

The shock deformation starts from the impacted end and progresses sequentially. In the shock loading the crushed and densified region attains a stress of $\sigma^*$ and the elastically deformed region attains a stress of $\sigma_p$ as shown in Figure 2.20. In figure 2.20 u is the displacement, h is the length of the densified region, $x$ is the uncrushed length, $x_o$ is the initial length of the crushed region, $\rho$ is the density of the crushed region and $\rho_o$ is the initial density and $l_o$ is the initial length.

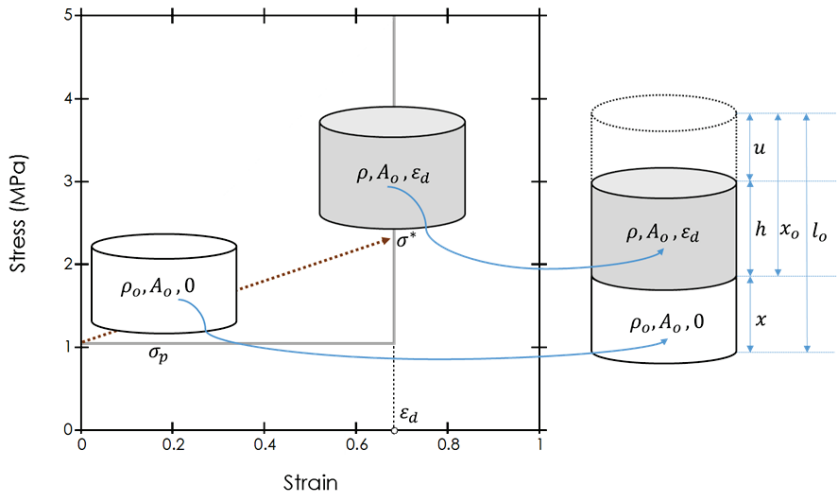


Figure 2.20. The schematic of r-p-p-l model stress-strain behavior and the deformed and undeformed part of foam sample

The initial length is therefore

$$l_o = u + h + x \tag{2.7}$$

and $x_o$ is

$$x_o = u + h \tag{2.8}$$

Then, $u$ and $h$ are

$$u = x_o \varepsilon_d \tag{2.9}$$

and

$$h = x_o(1 - \varepsilon_d) \tag{2.10}$$

From the unit mass ratio of the initial uncrushed and crushed regions, the following relation is written

$$\frac{x_o A_o \rho_o}{h A_o \rho} = 1 \tag{2.11}$$

The relation between initial density and crushed region density is therefore

$$\rho_o = \rho(1 - \varepsilon_d) \tag{2.12}$$

Consider a cellular projectile with a backing mass of M is fired to a fixed wall at an initial velocity of $v_o$ as shown in Figure 2.21 schematically. Applying mass and momentum conservations between crushed and uncrushed regions and the Newton's second rule to the uncrushed section the following relations are obtained

**Mass conservation: Mass in=Mass out**

Mass in: $\rho_o A_o(u_s + v)dt$

Mass out: $\rho A_o(u_s)dt$

$$\rho_o(u_s + v) = \rho(u_s)$$

$$u_s = \frac{\rho_o}{\rho - \rho_o} v = \frac{\rho(1 - \varepsilon_d)}{\rho - \rho(1 - \varepsilon_d)} v$$

$$u_s = \frac{(1-\varepsilon_d)}{\varepsilon_d} v \tag{2.13}$$

**Momentum conservation: $\mathbf{m\Delta v = \Delta F dt}$**

$$\rho A_o (u_s) dt.\, 0 - \rho_o A_o (u_s + v) dt.\, (-v) = (\sigma^* - \sigma_p) A_o dt$$

$$\rho_o (u_s + v) v = \sigma^* - \sigma_p$$

$$\sigma^* = \sigma_p + \rho_o (u_s + v) v$$

$$\sigma^* = \sigma_p + \rho_o \left[\frac{(1-\varepsilon_d)}{\varepsilon_d} + 1\right] v^2$$

$$\sigma^* = \sigma_p + \frac{\rho_o}{\varepsilon_d} v^2 \tag{2.14}$$

**Applying Newton's second rule to the uncrushed section**

$$F = m\frac{dv}{dt}$$

$$-\sigma_p A_o = [M + \rho_o A_o x]\frac{dv}{dt} = [M + \rho_o A_o (l_o - x_o]\frac{dv}{dt} = \left[M^* - \rho_o A_o \frac{u}{\varepsilon_d}\right]\frac{dv}{dt}$$

$$\frac{dv}{dt} = \frac{du}{dt}\frac{dv}{du} = v\frac{dv}{du} = \frac{-\sigma_p A_o}{(M^* - \rho_o A_o \frac{u}{\varepsilon_d})}$$

$$\int_{v_o}^{v} v dv = \int_0^u \frac{-\sigma_p A_o}{(M^* - \rho_o A_o \frac{u}{\varepsilon_d})} du$$

$$v^2 = v_o^2 + \frac{2\sigma_p \varepsilon_d}{\rho_o} \ln\left(1 - \frac{\rho_o A_o u}{M^* \varepsilon_d}\right)$$

$$v = \sqrt{v_o^2 + \frac{2\sigma_p \varepsilon_d}{\rho_o} ln\left(1 - \frac{\rho_o A_o u}{M^* \varepsilon_d}\right)} \tag{2.15}$$

Inserting Equation 2.15 into Equation 2.14 gives,

$$\sigma^* = \sigma_p + \frac{\rho_o}{\varepsilon_d}\left[v_o^2 + \frac{2\sigma_p \varepsilon_d}{\rho_o} ln\left(1 - \frac{\rho_o A_o u}{M^* \varepsilon_d}\right)\right] \tag{2.16}$$

The material completely densifies when $u = l_o\varepsilon_d$ and $x$ and $\dot{x} = 0$. Then, using Equations 2.7 and 2.8, the critical velocity for densification is determined as

$$x = l_o - x_o$$

$$\dot{x} = -\dot{x_o} = -\frac{\dot{u}}{\varepsilon_d} = -\frac{v}{\varepsilon_d} = -\sqrt{\frac{v_o^2}{{\varepsilon_d}^2} + \frac{2\sigma_p}{\varepsilon_d\rho_o} ln\left(1 - \frac{\rho_o A_o l_o}{M^*}\right)} = 0$$

$$v_o'^2 = -\frac{2\sigma_p\varepsilon_d}{\rho_o} ln\left(\frac{M + \rho_o A_o l_o - \rho_o A_o l_o}{M + \rho_o A_o l_o}\right) = \frac{2\sigma_p\varepsilon_d}{\rho_o} ln\left(\frac{M + \rho_o A_o l_o}{M}\right)$$
$$= \frac{2\sigma_p\varepsilon_d}{\rho_o} ln\left(1 + \frac{m_F}{M}\right)$$

$$v_o' = \sqrt{\frac{2\sigma_p\varepsilon_d}{\rho_o} ln\left(1 + \frac{m_F}{M}\right)} \tag{2.17}$$

where, $m_F$ is the mass of the cellular material and $M$ is the backing mass. When $M$=0, $v_o'$ is infinity, implying that the cellular test specimen will not densify without backing mass in a Taylor-like impact test. The critical mass for the complete densification ($M_{cr}$) is calculated using and modifying Equation. 2.17 as

$$\frac{M_{cr}}{m_F} = \frac{1}{\left[e^{\frac{v_o^2\rho_o}{2\sigma_p\varepsilon_d}} - 1\right]} \tag{2.18}$$

The time of the deformation ($t$) is calculated as

$$t = \int_0^u \frac{du}{\sqrt{v_o^2 + \frac{2\sigma_p\varepsilon_d}{\rho_o} ln\left(1 - \frac{u}{\varepsilon_d L_o}\right)}} \tag{2.19}$$

The final displacement or arrest distance ($u_f$) of the sample is

$$u_f = \varepsilon_d L_o \left[1 - e^{\left(\frac{-v_o^2 \rho_o}{2\sigma_p \varepsilon_d}\right)}\right] \tag{2.20}$$

The arrest distance varies between 0 and $\varepsilon_d L_o$. Note that inserting the full compaction of the sample, $u_f = \varepsilon_d L_o$ , into Equation 2.20 results in an infinite time. This shows that the shock generated is arrested before it reaches the end of the sample. The arrest time ($\tau$) is given as

$$\tau = \frac{u_f}{v_o} \tag{2.21}$$

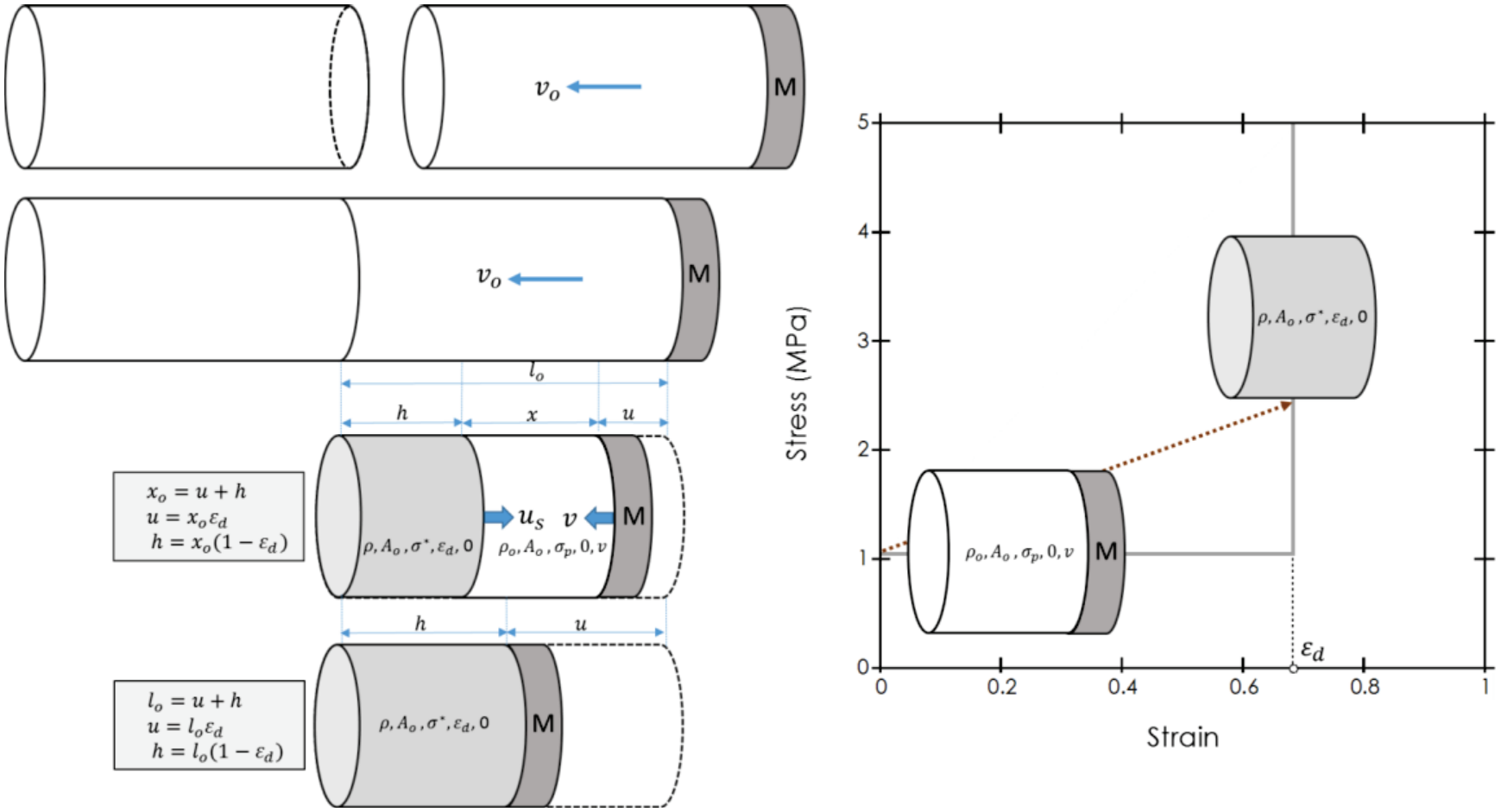


Figure 2.21. Direct impact of cellular material projectile with a backing mass to a rigid wall and the velocities developed in the crushed and uncrushed regions

Consider a cellular projectile standing in front of a rigid wall is impacted with a projectile with a mass of M and an initial velocity of $v_o$ as shown in Figure 2.22 schematically. Applying mass and momentum conservations between crushed and uncrushed regions and the Newton's second rule to the crushed section following relations are obtained.

**Mass conservation: Mass in=Mass out**

Mass in: $\rho_o A_o u_s dt$

Mass out: $\rho A_o (u_s - v) dt$

$$\rho_o u_s = \rho(u_s - v)$$

$$u_s = \frac{\rho}{\rho - \rho_o} v = \frac{\rho}{\rho - \rho(1 - \varepsilon_d)} v$$

$$u_s = \frac{v}{\varepsilon_d} \tag{2.22}$$

**Momentum conservation: $\mathbf{m\Delta v = \Delta F dt}$**

$$\rho A_o (u_s - v) dt . v - \rho_o A_o u_s dt . 0 = (\sigma^* - \sigma_p) A_o dt$$

$$\rho(u_s - v)v = \sigma^* - \sigma_p$$

$$\sigma^* = \sigma_p + \frac{\rho_o}{(1 - \varepsilon_d)} \left( \frac{v}{\varepsilon_d} - v \right) v$$

$$\sigma^* = \sigma_p + \frac{\rho_o}{(1 - \varepsilon_d)} \left( \frac{1 - \varepsilon_d}{\varepsilon_d} \right) v^2$$

$$\sigma^* = \sigma_p + \frac{\rho_o}{\varepsilon_d} v^2 \tag{2.23}$$

**Applying Newton's second rule to the crushed section**

$$F = m \frac{dv}{dt}$$

$$-\sigma^* A_o = [M + \rho A_o h] \frac{dv}{dt} = \left[ M + \frac{\rho_o}{(1 - \varepsilon_d)} A_o \left( \frac{1 - \varepsilon_d}{\varepsilon_d} \right) u \right] \frac{dv}{dt} = \left[ M + \rho_o A_o \frac{u}{\varepsilon_d} \right] \frac{dv}{dt}$$

$$\frac{dv}{dt} = \frac{du}{dt} \frac{dv}{du} = v \frac{dv}{du} = \frac{-\sigma^* A_o}{\left( M + \rho_o A_o \frac{u}{\varepsilon_d} \right)} = \frac{-\left( \sigma_p + \frac{\rho_o}{\varepsilon_d} v^2 \right)}{\left( \frac{M}{A_o} + \frac{\rho_o u}{\varepsilon_d} \right)}$$

$$-\int_{v_o}^{v}\frac{vdv}{\left(\sigma_p+\frac{\rho_o}{\varepsilon_d}v^2\right)}=\int_0^u\frac{du}{\left(\frac{M}{A_o}+\frac{\rho_o u}{\varepsilon_d}\right)}$$

$$-\frac{\varepsilon_d}{2\rho_o}ln\left(\sigma_p+\frac{\rho_o}{\varepsilon_d}v^2\right)=\frac{\varepsilon_d}{\rho_o}ln\left(\frac{M}{A_o}+\frac{\rho_o u}{\varepsilon_d}\right)$$

$$ln\left(\frac{\sigma_p+\frac{\rho_o}{\varepsilon_d}{v_o}^2}{\sigma_p+\frac{\rho_o}{\varepsilon_d}v^2}\right)=ln\left(\frac{\frac{M}{A_o}+\frac{\rho_o u}{\varepsilon_d}}{\left(\frac{M}{A_o}\right)^2}\right)$$

$$v=\sqrt{\frac{\varepsilon_d}{\rho_o}\left[\frac{\left(\frac{M}{A_o}\right)^2\left(\sigma_p+\frac{\rho_o}{\varepsilon_d}{v_o}^2\right)}{\left(\frac{M}{A_o}+\frac{\rho_o u}{\varepsilon_d}\right)^2}-\sigma_p\right]} \tag{2.24}$$

Inserting Equation 2.15 into Equation. 2.23 gives,

$$\sigma^*=\frac{\left(\frac{M}{A_o}\right)^2\left(\sigma_p+\frac{\rho_o}{\varepsilon_d}{v_o}^2\right)}{\left(\frac{M}{A_o}+\frac{\rho_o u}{\varepsilon_d}\right)^2} \tag{2.25}$$

The material completely densifies when $u=l_o\varepsilon_d$ and $v=0$. Then, using Equations 2.1 and 2.2, the critical velocity for densification is determined as,

$$v_o'=\sqrt{\frac{\sigma_p\varepsilon_d}{\rho_o}\left[\left(1+\frac{\rho_o A_o l_o}{M}\right)^2-1\right]} \tag{2.26}$$

$$v_o'=\sqrt{\frac{\sigma_p\varepsilon_d}{\rho_o}\left[\left(1+\frac{m_F}{M}\right)^2-1\right]} \tag{2.27}$$

when M=0, $v_o'$ is infinity gain.

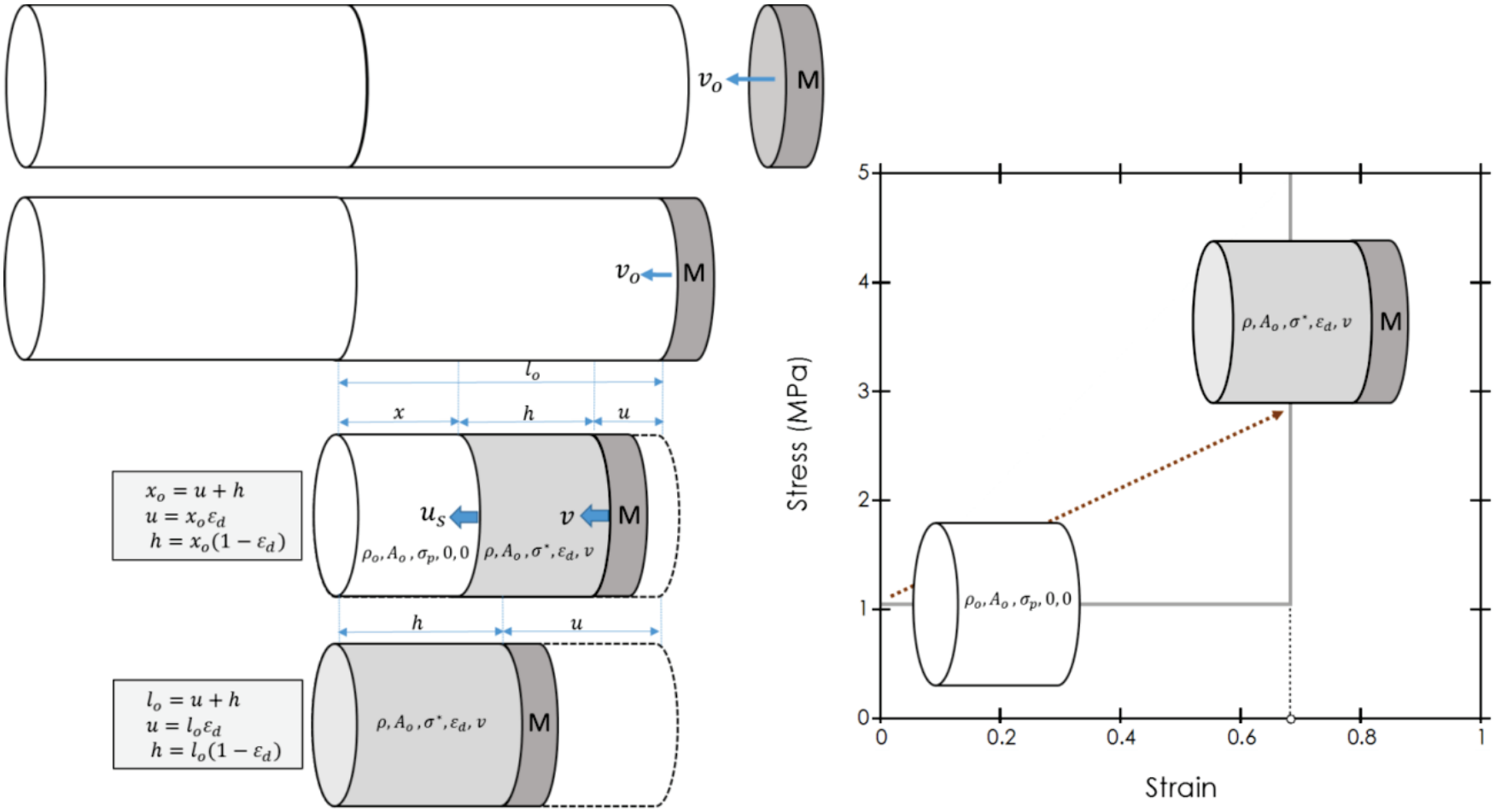


Figure 2.22. The impact of cellular material with a rigid projectile and the velocities developed in the crushed and uncrushed regions

# CHAPTER 3

# MATERIALS AND EXPERIMENTS

## 3.1. Multi-Layered Corrugated Trapezoidal Zig-Zag Core Structure

The investigated multi-layered sandwich core structure was made of 1050 H14 Al trapezoidal zig-zag corrugated layers (fins) as seen in Figure 3.1(a) and constructed using 15 zig-zag fin layers. The height, width, length and thickness of a fin are sequentially 3.20, 1.6, 2.4 and 0.170 mm (Figure 3.1(b)). The corrugated Al fin layers were produced by a local factory using a sheet-forming process in which the sheet metal is formed by the help of a press into a regular trapezoidal shape. Later, the fin layers were assembled by a brazing process. The brazing was performed in a furnace at 600 $^{o}$C (10 min) using a 4343 Al filler (~7 wt%). The zig-zag form enhances the heat conduction between the fin layers in a multi-layered construction. The brazed multi-layered corrugated sandwich panel shown in Figure 3.1(a) is 500x500x50 mm in size and assembled in 0/90 fin layer configuration. The face sheets, 1 mm thick 1050 H14 sheet, prevent the mechanical damaging of the layers in brazing and subsequent machining operations.

A cylindrical compression test sample 19.40 mm in diameter is shown in Figure 3.2(a). These tests samples were extracted from the sandwich plate by means of an electro-discharge machine. The test samples had a height of 48 mm and a density of 326 kg m$^{-3}$ without face sheets. In the SHPB tests, the samples were tested without face sheets. In the direct impact tests in order to make a full contact between the sample and the bar, the samples had a face sheet on the incident bar side, while in the Taylor impact tests, the samples had a face sheet at the rear/back end. The test sample shown in Figure 3.2(a) contains typical fin wall imperfections induced during brazing and cutting processes. The fin walls are slightly bent in as-received sandwich (white arrows in Figure 3.2(b)). During sample cutting, the fin walls at the outer surface are significantly bent (Figure 3.2(c)). These imperfections are likely to change the location of the layer collapse and crushing stress values. In order to simulate the effect of fin wall imperfection, as will be explained in the modelling section, a bending type imperfection was introduced to the fin layers. Second, the fin walls are thicker at the fin contact

points which were attributed to the filler accumulation at these sites (black arrows shown in Figures 3.2(b) and (c)). The thick contact points may affect the densification strain and also crushing stress values.

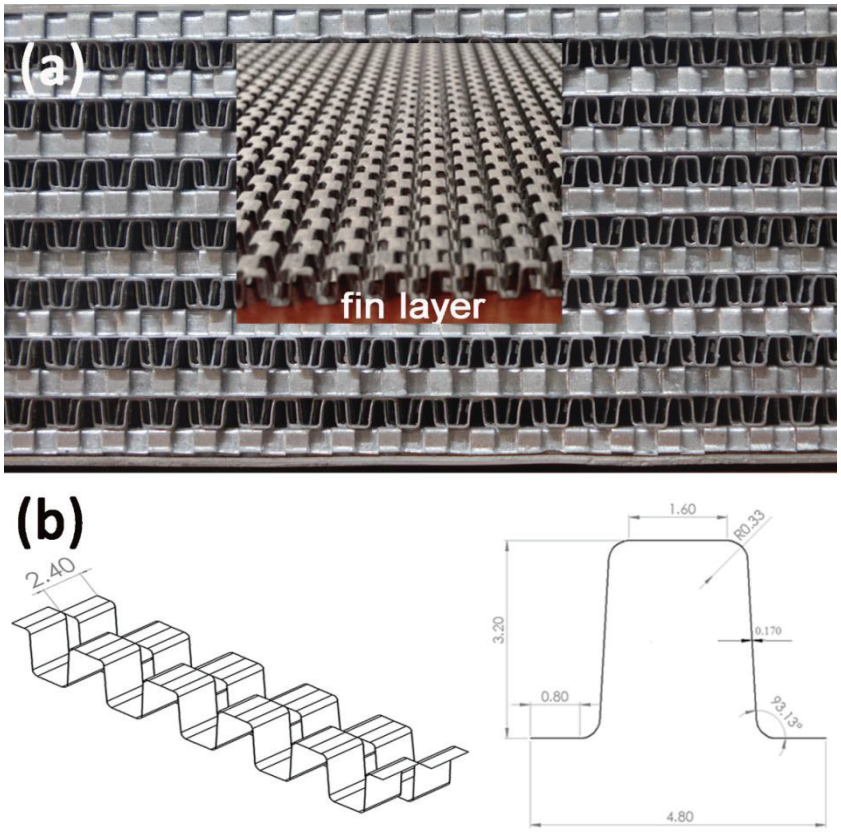


Figure 3.1. (a) the multi-layered corrugated layer and core sandwich plate cross-section and (b) fin geometrical sizes

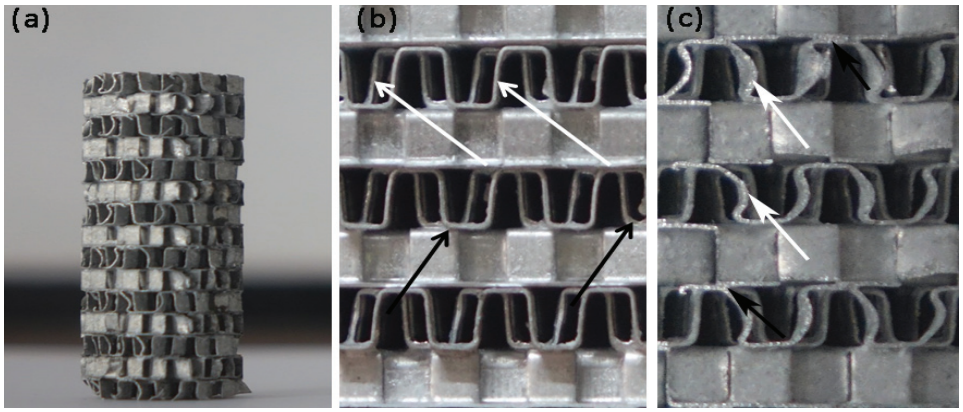


Figure 3.2. (a) test sample 19.40 mm in diameter and 48 mm in length and (b) slightly bent fin walls (white arrows) and increased thickness near the contact/brazing region (black arrows) of the as-received sandwich and (c) the surface of core-drilled sample

## 3.2. Static and Dynamic Tests

The quasi-static compression tests were performed at nominal strain rate of $10^{-1}$ $s^{-1}$. The tests at lower quasi-static strain rates however increased the simulation solution time substantially. A video extensometer synchronized with the Shimadzu Universal test machine was used to record the displacement of the sample. The compression test plates were lubricated using a thin layer of grease before each test. The sample deformation during a test was recorded with a video camera in order to determine the start and sequences of the layer crushing.

Three different dynamic tests were conducted. In the first test, the sample was directly compressed in a conventional compression SHPB between incident and transmitter bars. These tests are called SHPB tests. In the second type of dynamic test, the sample was inserted in front of the incident bar and the striker bar is directly impinged the corrugated test sample with an initial velocity. These tests are referred to as the direct impact tests. In the last group, the corrugated sample was directly impacted with an initial velocity to the end of the incident bar. These tests are called Taylor-like impact tests as they are very much similar to the Taylor impact tests.

### 3.2.1. SHPB Tests

The SHPB testing method was developed by Kolsky in 1948 to determine the high strain rate deformation behavior of metals [75]. The test is also known as the Kolsky's Bar. Before Kolsky, Bertham Hopkinson [76] used a similar testing configuration in 1914 to measure the momentum trapped by the samples attached to a long bar, while Kolsky divided this long bar in two and inserted a cylindrical test sample in between the split bars, later known as incident and transmitter bars. This allowed him to directly measure stress, strain, and strain rate developed in the test sample. Although originally developed for metals, SHPB testing method has been determined one of the most convenient and easiest techniques of testing of metals, polymers, ceramics and composites at increasingly high strain rates between broadly 500-5000 $s^{-1}$. The strain rate may vary depending of the test material type. The principles of SHPB testing are based on uniaxial elastic wave propagation in long bars.

The schematic of SHPB testing, composing of three bars (striker, incident and transmitter), is shown in Figure 3.3. The specimen is sandwiched between the incident and transmitter bar. When the striker bar having an initial velocity of $v_o$ strikes another standing long bar (incident bar) having the same elastic modulus and diameter as the striker bar, a rectangular elastic compressive stress pulse is produced on the incident bar. The developed stress wave on the incident bar propagates along the bar; when it comes cross with the specimen interfaces, part of the wave is reflected as tensile wave into the incident bar and the rest is transmitted to the transmitter bar as a compressive wave. The relative amounts of the reflected and transmitted stress waves are function of the mechanical impedance difference between the bars and the sample tested. The incident and reflected waves are measured by means of a same strain gage mounted on the incident bar, while the transmitted wave is measured with a separate strain gage mounted on the transmitter bar. Since the distance between the specimen and strain gage locations on the bars are the same ($x_1 = x_2$ in Figure 3.3), the starting points of the reflected and transmitted waves on the time axis are the same. This makes the data analysis for stress, strain and strain rate easy.

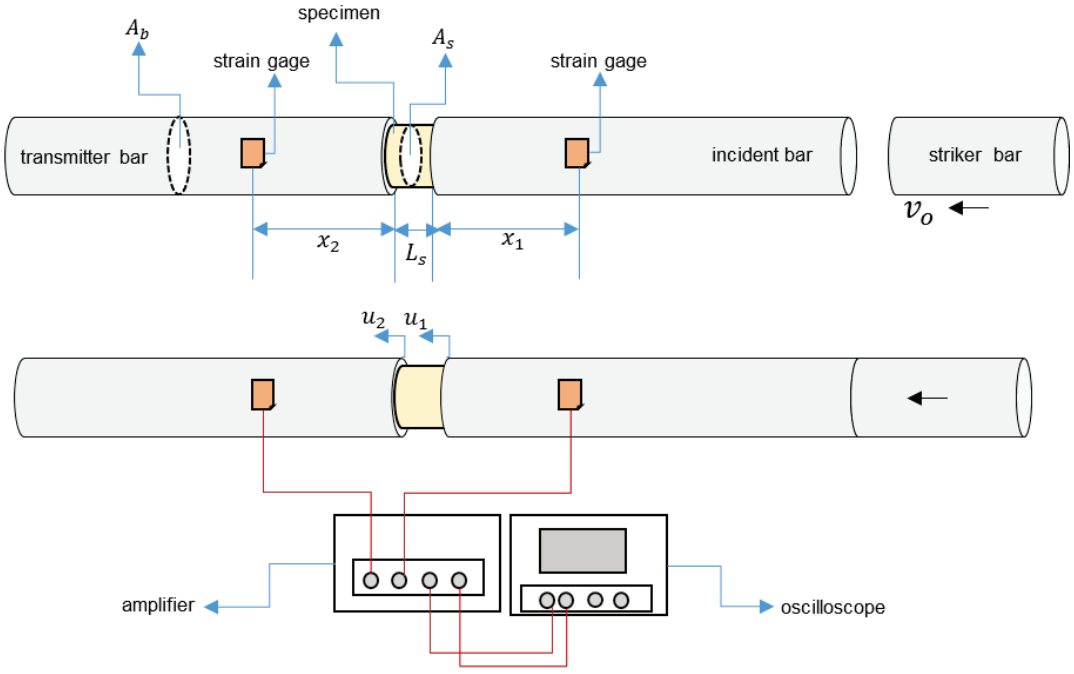


Figure 3.3. The schematic of SHPB test

The relative magnitude of the incident stress and strain is direct function of the striking bar velocity and the incident bar modulus ($E$) and bar's elastic wave velocity ($c$). The maximum stress ($\sigma_b$) and the maximum strain ($\varepsilon_b$) on the incident bar are

$$\sigma_b = \frac{E v_o}{2c} \tag{3.1}$$

and

$$\varepsilon_b = \frac{v_o}{2c} \tag{3.2}$$

As opposite to the theory, the experimental incident wave is not perfect rectangular in shape. The wave reaches the maximum stress/strain after a certain time called the *rise time*. The rise time is important in the testing brittle materials such as ceramics. The brittle materials fail during the rise time leading to the stress in-equilibrium (the sum of the incident and reflected waves is not equal to the transmitted wave) in the specimen. The increased rise time; however, results in a gradual loading of the test specimen and allows the specimen to establish stress equilibrium. The stress on the incident bar also should not exceed the yield strength of the bar material, otherwise the stress propagation occurs plastically invalidating both the stress and strain calculations based on elastic wave propagation. Therefore, the selection of the bar material is of critical importance in order not to go beyond the yield strength of the bar material. The typical velocities of the striker bar in SHPB testing range 2-20 m $s^{-1}$ and the specimen sizes 5-10 mm, corresponding to the strain rates ranging 200-4000 $s^{-1}$.

The displacements of the incident and transmitter bars $u_1$ and $u_2$ shown in Figure 3.3 is calculated using the following equations

$$u_1(t) = c \int_0^{\tau} (-\varepsilon_I + \varepsilon_R) dt \tag{3.3}$$

and

$$u_2(t) = -c \int_0^{\tau} \varepsilon_T dt \tag{3.4}$$

where *I, R* and *T* refer to the incident, reflected and transmitted bars, respectively. The strain ($\varepsilon_s$) in the specimen is

$$\varepsilon_s(t) = \frac{u_2(t) - u_1(t)}{L_s} = \frac{c \int_0^{\tau} (-\varepsilon_T + \varepsilon_I - \varepsilon_R) dt}{L_s} \tag{3.5}$$

where, $L_s$ is the specimen length. The loads ($P$) on each interface, incident bar/specimen (1) and specimen/transmitter bar (2) are

$$P_1 = A_b E(\varepsilon_I + \varepsilon_R) \tag{3.6}$$

$$P_2 = A_b E \varepsilon_T \tag{3.7}$$

where, $A_b$ in the cross-section area of the bar. It is assumed that the wave propagation in a short sample may be neglected, so that $P_1$=$P_2$ .Therefore, Equation 3.5 is written as

$$\varepsilon_s(t) = \frac{-2c \int_0^{\tau} \varepsilon_R dt}{L_s} \tag{3.8}$$

Accordingly, the stress ($\sigma_s$) in the test specimen is

$$\sigma_s(t) = \frac{A_b E \varepsilon_T}{A_s} = \frac{A_b E(\varepsilon_I + \varepsilon_R)}{A_s} = \frac{A_b E(\varepsilon_T + \varepsilon_I + \varepsilon_R)}{2A_s} \tag{3.9}$$

where, $A_s$ is the specimen area. In Equation 3.9, the first, second and third formulations are sequentially one, two and three-wave methods of specimen stress calculation. The specimen strain rate is calculated using the following relation

$$\dot{\varepsilon}_s(t) = \frac{-2c\varepsilon_R}{L_s} \tag{3.10}$$

Before each test, the specimen size, length and diameter should be measured to calculate strain, strain rate and stress. In the experiments, the strain in the bars is calculated using the following relation

$$\varepsilon_s = -\frac{2c}{L_s}\left[\frac{2\int \varepsilon_R(V)dt}{GKV(1+v)}\right] \tag{3.11}$$

where *G*, *K*, *V* and *v* were the strain gage conditioner gain, strain gage factor, excitation voltage of the strain gage bridge and Poisson's ratio of the bar material, respectively. The above formulation is only valid for a ''Full-Bridge'' strain gage circuit. Similarly the stress in the specimen is calculated using

$$\sigma_s = \frac{A_b}{A_s}E_b\left[\frac{2\varepsilon_T(V)}{GKV(1+v)}\right] \tag{3.12}$$

The SHPB apparatus used in the tests consisted of a 19.40 mm diameter Inconel 718 bar; 3110 mm long incident bar, 2050 mm long-transmitter bar and 500 and 750 mm long striker bars (Figure 3.4). The values *G*, *K* and *V* in a typical test were 20, 2.09 and 10 V, respectively. The striker bar velocity in testing corrugated samples in the SHPB tests ranged between 6 and 10 m $s^{-1}$. The sample deformation was captured by a Fastcam Photron high speed camera at 20,000 fps.

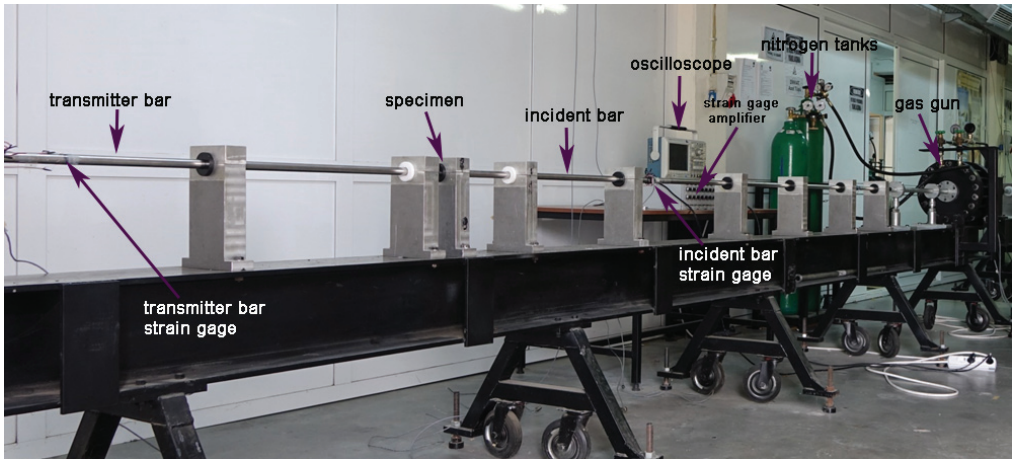


Figure 3.4. The used SHPB apparatus

### 3.2.2. Direct Impact Tests

In the SHPB direct impact test, the test specimen is placed in front of incident bar and striker bar with an initial velocity impinge the specimen, deforming it until about large strains (Figures 3.5(a) and (b)). The stress and strain analyses of the test in the direct impact test are based on the assumption of the stress equilibrium between incident-specimen and striker bar-specimen interfaces as the areas of the incident and striker bars are the same; $\sigma_2=\sigma_1$ (Figure 3.5(a)) [77]. Then, the strains on the bars, striker and incident bars, are equal to each other $\varepsilon_2=\varepsilon_1$, if the striker and incident bars are made of the same material. The strain in the specimen is

$$\varepsilon_s(t) = \frac{u_2(t) - u_1(t)}{L_s} \tag{3.13}$$

where $u_2$ and $u_1$ was the displacement of the striker and incident bars, respectively. The strain in the incident bar is given as

$$\varepsilon_1(t) = \frac{v(t)}{c} \tag{3.14}$$

where $v = \frac{du}{dt}$. The displacement of the incident bar is

$$u_1(t) = c \int_0^{\tau} \varepsilon_1 dt \tag{3.15}$$

Similarly, the displacement of the striker bar is

$$u_2(t) = v_o t - c \int_0^{\tau} \varepsilon_2 dt \tag{3.16}$$

Inserting Equation 3.15 and 3.16 into Equation 3.13 gives the specimen strain as

$$\varepsilon_s(t) = \frac{v_o t - c \int_0^{\tau} \varepsilon_2 dt - c \int_0^{\tau} \varepsilon_1 dt}{L_s} \tag{3.17}$$

Due to the stress equilibrium, Equation 3.17 can be written as

$$\varepsilon_s(t) = \frac{v_o t - 2c\int_0^\tau \varepsilon_T dt}{L_s} \tag{3.18}$$

By measuring the strain on the incident bar, the specimen's strain as function of time can be calculated using Equation 3.18. The stress on the specimen is directly calculated using the strain on the incident bar. In this case, the specimen stress is

$$\sigma_s(t) = \frac{A_b E \varepsilon_T}{A_s} \tag{3.19}$$

The strain rate is

$$\dot{\varepsilon}_s(t) = \frac{d\varepsilon_s(t)}{dt} = \frac{v_o - 2c\varepsilon_T(t)}{L_s} \tag{3.20}$$

The test specimen in the experiments was attached to the center of the incident bar using a lubricant which was strong enough to hold the specimen in front of the incident bar as seen in Figure 3.5(b). During the test, the stress on the incident bar was measured using two full-bridge strain-gage circuits; one was 300 mm and the other was 1110 mm away from impact end. The former gage is coded as the front strain gage and the latter as the back strain gage (Figure 3.5(a)). The striker bar velocity was measured just before the impact of the striker bar to the test sample using two laser diodes placed at the exist of the gas gun barrel (Figure 3.5(b)). The velocity of the striker bar was altered by changing the SHPB gas gun pressure. At higher gas gun pressures, the velocity of the striker bar will be higher and vice versa. In the direct impact tests, the velocity of the striker bar ranged between 9 and 90 m $s^{-1}$. The striker bars were made of different materials and lengths, while all the striker bars had the same diameter of 19.40 mm with the incident bar. The Inconel striker bar 250 mm-long was used for 9 m $s^{-1}$ and 22 m $s^{-1}$ tests, aluminum striker bars of 200 and 100 mm long for 40 m $s^{-1}$ and 60 m $s^{-1}$ tests respectively. And a wood striker bar of 200 mm-long was used for 90 m $s^{-1}$ test.

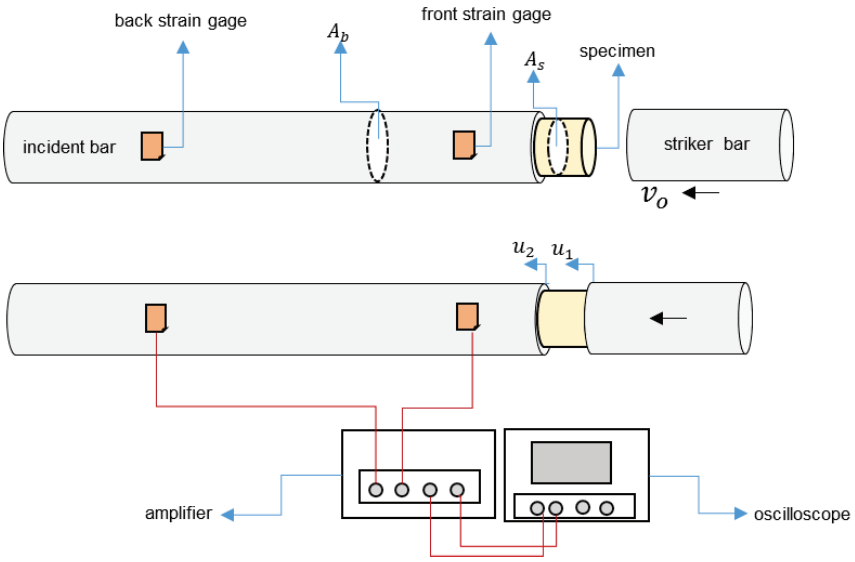


(a)

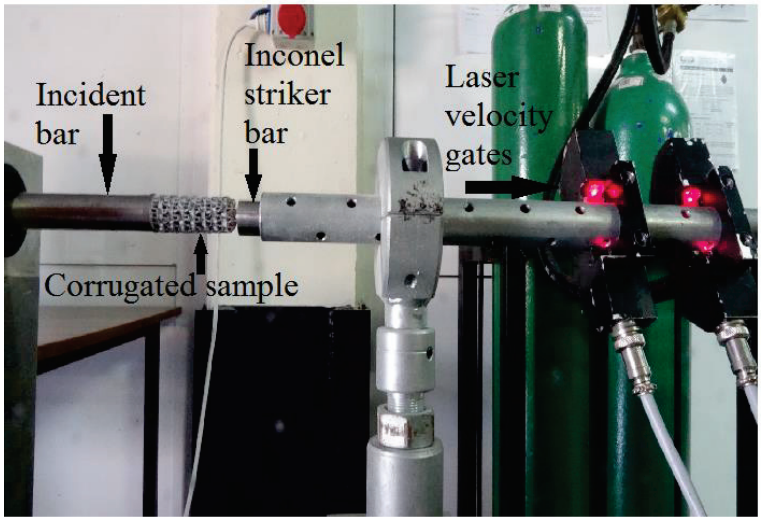


(b)

Figure 3.5. (a) the schematic of direct impact test and (b) the picture of experimental direct impact set-up

### 3.2.3. SHPB Taylor-like Impact Tests

In the Taylor-like impact tests, the corrugated sample was directly fired to end of the incident bar with a velocity as depicted in Figure 3.6. In this case, the stress in the specimen is

$$\sigma_s(t) = \frac{A_b E \varepsilon_I}{A_s} \tag{3.21}$$

and the strain of the specimen is

$$\varepsilon_s(t) = \frac{v_o t - 2c\int_0^\tau \varepsilon_I dt}{L_s} \tag{3.22}$$

In the Taylor-like impact tests, the velocity of the specimen varied between 135 to 200 m $s^{-1}$. Similar to direct impact tests, the stress in the Taylor impact tests was measured by means of full-bridge strain gages mounted 300 and 1110 mm away from the impact end.

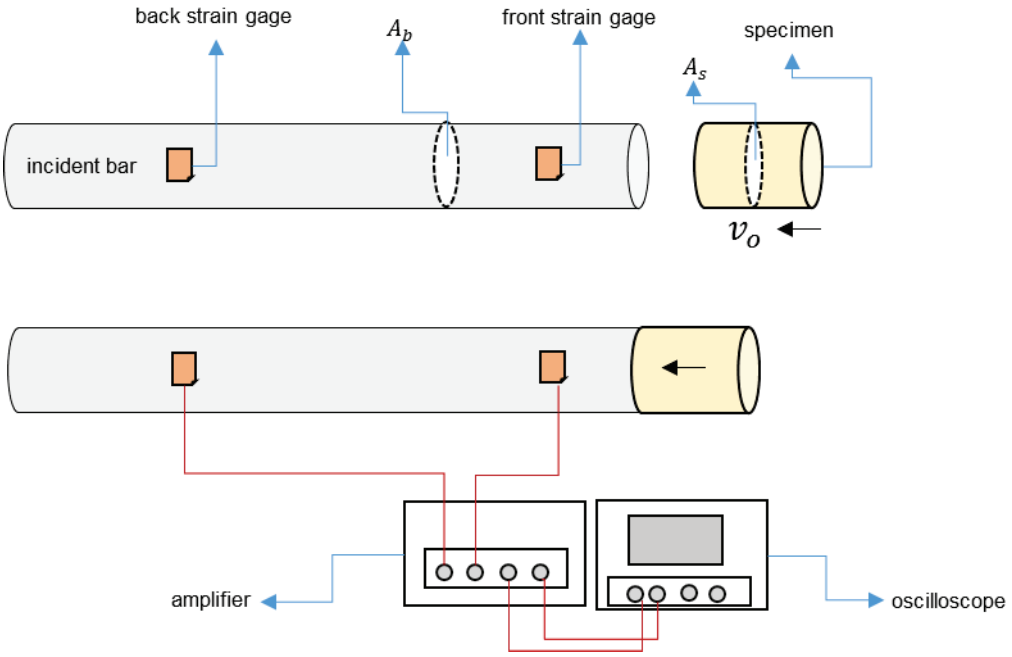


Figure 3.6. Schematic of Taylor-like impact test

# CHAPTER 4

# MODELLING

## 4.1. Methodology

The numerical model of quasi-static and dynamic testing of the layered corrugated core structure was composed of solid structure modeling, meshing, pre-processing, and solution and verification of numerical results. Three dimensional tests models were developed in Solidworks CAD Software. The unit fin of the corrugated layer was created in CAD software and meshed with predefined finite elements. Then, the generated unit cell was transformed into the Hypermesh software. The meshed unit cell was duplicated to form a long chain of the cells in the long axis (x-axis). After that, the structure was duplicated in the transverse direction (y-axis) and moved in the direction of x-axis simultaneously to create zig-zag form. The full geometrical numerical models of the tests were developed in non-linear explicit FE code of LS-Dyna. These models were then meshed and then exported to LS-PrePost software to define material properties, boundary conditions, contacts, test conditions, termination time and mass scaling for quasi-static loading. The solution was implemented in LS-Dyna Solver.

## 4.2. Numerical Models of Multi-layer Corrugated Sandwiches

As stated earlier, the handling of the fin layers during brazing and then later in cutting with electro discharge machine unavoidably induced imperfections on the fin walls. Since the layers accommodated varying intensities of the imperfections, in the quasi-static compression testing of the corrugated samples, the crushing was observed to start in the weakest core layer and then proceeded non-sequentially. In order to simulate, the effect of fin wall imperfection on the crushing behavior and also on the crushing stress, a bending type imperfection 3.2 mm in length and 1.6 mm in radius determined from the micrographs of a machined sample (Figure 4.1(b)) was inserted into the fin layers. Four numerical models of the corrugated core samples were then

investigated. These are (1) perfect model I, (2) perfect model II, (3) one-layer imperfect model and (4) two layer imperfect model (Figure 4.2). In the perfect model I, all layers were constructed using the perfect unit cell fin (Figures 4.1(a) and 4.2(a)). In perfect model II, all fin layers were constructed using the bent unit cell as shown in Figures 4.1(b) and 4.2(b)). In one layer imperfect model, only layer 10 (from top to bottom there are 15 layers) was constructed using the bent unit cells (black arrow in Figure 4.2(c)) and in two layer imperfect model, layer 2 and layer 10 were constructed using the bent unit cell (black arrows in Figure 4.2(d)). The perfect I, perfect II, one layer imperfect and two layer imperfect models consisted of 34942, 41921, 35116 and 33570 shell elements, respectively.

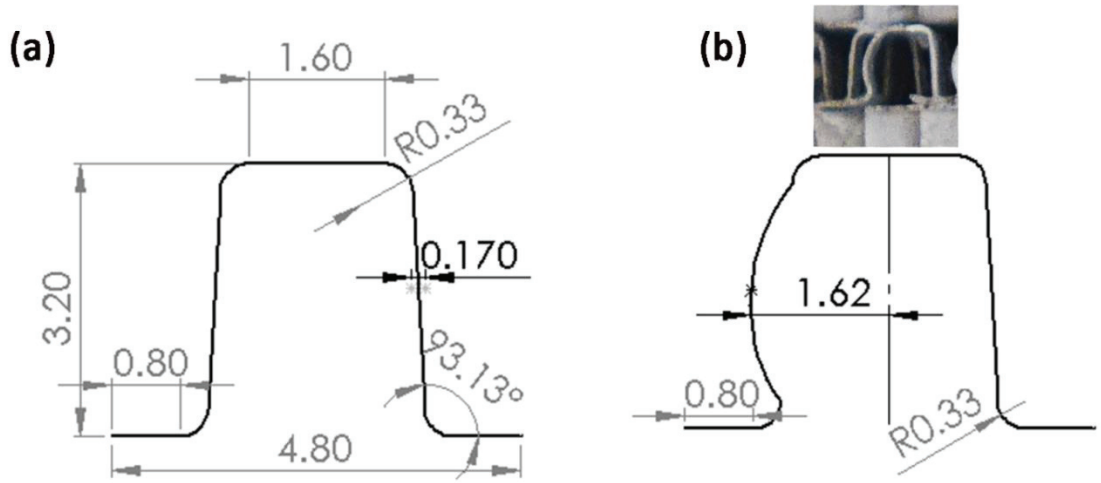


Figure 4.1. Perfect and imperfect unit fin geometry

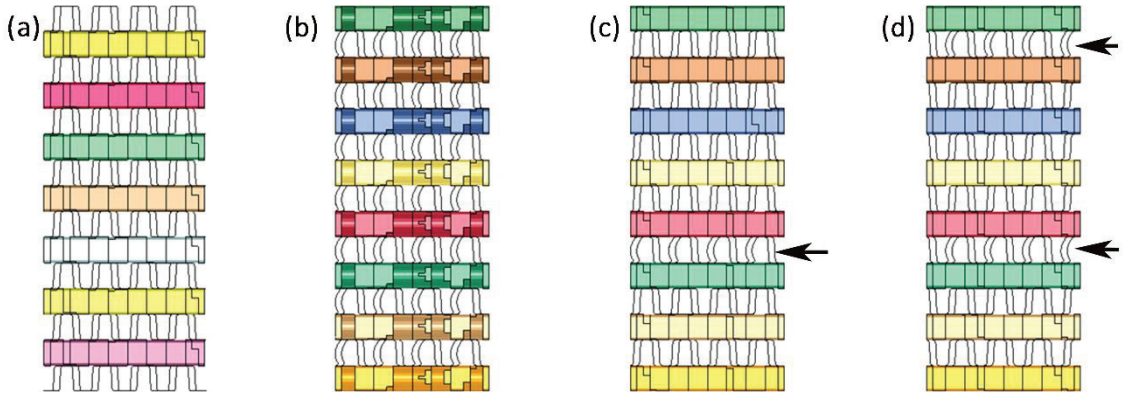


Figure 4.2. (a) perfect model I, (b) perfect model II, (c) one layer imperfect model and (d) two layer imperfect model

The trapezoidal corrugated fin layers were meshed using Belytschko-Tsay shell elements (0.25x0.25 mm) with five integration points and 1050 Al face sheets were

modeled using the constant stress solid elements. The increased number of integration points in shell elements generally led to prolonged CPU calculation times. On the other side, in order to increase the accuracy of the models, the number of integration points should be higher than two when the buckling is the dominant deformation mode [78]. In addition, the FE meshes of the corrugated fin layers and face sheets had to coincide with each other in order to be able to define contacts. These naturally limit the use of arbitrary-defined mesh distribution and elements size.

The 1050 Al aluminum alloy was modeled with MAT_RIGID and MAT_SIMPLIFIED_JOHNSON_COOK (Material type 98) material models, respectively. The equivalent stress ($\sigma_y$) in the Johnson and Cook (JC) flow stress model [79] is given as

$$\sigma_y = \left[A + B\varepsilon_p^n\right]\left[1 + C\ ln\dot{\varepsilon}_p^*\right]\left[1 - T_H^m\right] \tag{5.1}$$

where $\varepsilon_p$ is the equivalent plastic strain, $\dot{\varepsilon}_p^*$ is the strain rate ratio given as $\frac{\dot{\varepsilon}_p}{\dot{\varepsilon}_o}$, where $\dot{\varepsilon}_p$ is the equivalent plastic strain rate, $\dot{\varepsilon}_o$ is the reference equivalent plastic strain rate, and $T_H$ is the normalized temperature expressed as $T = \frac{T - T_r}{T_m - T_r}$; where $T$, $T_r$ and $T_m$ are the temperature, room temperature and melting temperature, respectively. Material type 98 does not take into account temperature effect and further aluminum alloys have no or negligible strain rate dependent flow stress; therefore, only first bracket of Equation 5.1 is taken into account. The material model parameters of 1050 H14 Al were determined previously as A=102 MPa, B=98 MPa and n=0.18 [80].

Figures 4.3(a) and (b) show the front and 3D view of the numerical model of quasi-static compression test set-up, respectively. The model consisted of the top and bottom compression test steel platen and sample. Each compression test platen was modeled using 38400 constant stress solid elements (Figure 4.3(b)). The compression steel platens were modeled with MAT20_RIGID material model (E=210 GPa and $v = 0.3$). In the model, the rotations and the movement of the compression platens were fully constrained, except the axial motion of the top platen in the z-direction. The axial velocity (z-direction) of the top platen was kept constant, the same as the experiments and defined by PRESCRIBED_MOTION_RIGID card. The contact between compression test platens and specimen was defined by AUTOMATIC_SURFACE_TO SURFACE contact. Since the total CPU time for the quasi-static test solutions were

relatively long [81], the mass scaling was applied in the quasi static simulations by defining a positive time step value in CONTROL_TIMESTEP card. The mass was added or removed from elements so that the time step of the elements was the same. In order to determine the mass scaling factor, the simulation was initially run without mass scaling and the determined time step without mass scaling was multiplied by 10, 100 and 1000. It was found numerically that the kinetic energy change was substantially lower than the internal energy change when the mass scaling factor was 1000. For quasi-static models, the contacts between core layers were ERODING_SINGLE_SURFACE contact algorithm.

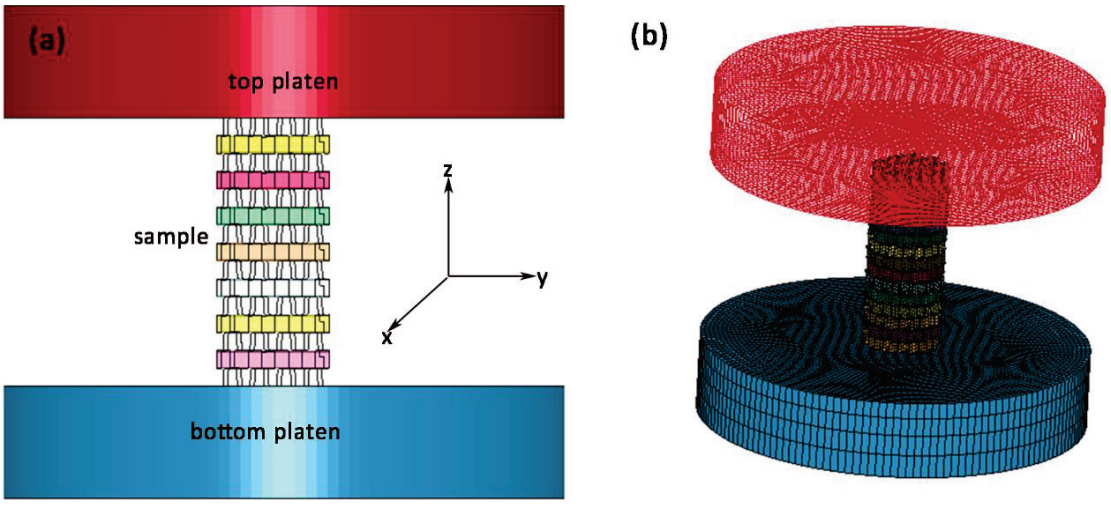


Figure 4.3. The numerical model of quasi-static compression test set-up

The full numerical model of the SHPB test and the specimen bar interfaces are shown in Figures 4.4(a) and (b), respectively. The lengths of incident and transmitter bars were 3110 mm and 2050 mm, respectively. The Inconel 718 striker, incident and transmitter bars were modeled using 15 mm size elements. The incident and transmitter bar consisted of 28980 and 19180 constant stress solid elements, respectively. The number of constant stress elements of the striker bar varied with the length of the striker bar. The impact velocities in the SHPB models were 6 and 10 m $s^{-1}$ as with the experiments.

The full model direct impact test model and the specimen bar interfaces are shown in Figures 4.5(a) and (b), respectively. The Inconel incident bar was modeled using 15 mm size elements, while the striker bar was modeled using 5 mm size elements. The Inconel 250 mm-long striker bar model consisted of 12000 constant stress solid elements, while the aluminum striker bars of 100 mm-long consisted of

4800 and aluminum and wood striker bar of 200 mm-long consisted of 10080 constant stress solid elements. The impact velocities in direct impact test models were 9, 22, 40, 60 and 90 m $s^{-1}$ as with the experiments.

The full Taylor impact test model and the specimen bar interfaces are shown in Figures 4.6(a) and (b), respectively. The impact velocity was defined to the mass by VELOCITY_GENERATION card in LS-Dyna. The impact velocities in the numerical models varied between 135 to 200 m $s^{-1}$. The contact between the bar and specimen was defined by AUTOMATIC_SURFACE_TO SURFACE contact. The contact between the layers of the corrugated sample and face sheets was defined by AUTOMATIC_SINGLE_SURFACE contact algorithm.

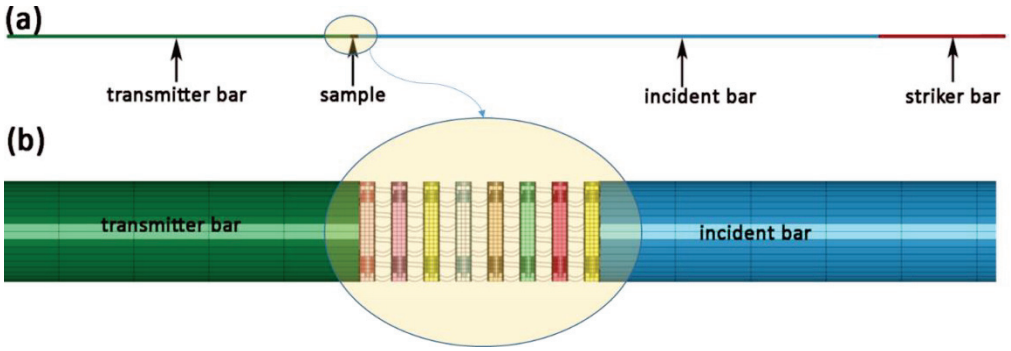


Figure 4.4. (a) SHPB test model and (b) specimen bar interfaces

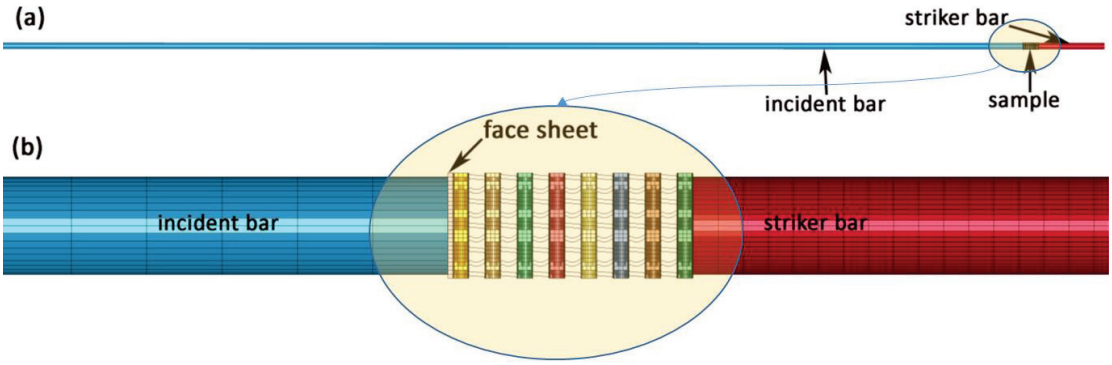


Figure 4.5. (a) direct impact test model and (b) specimen bar interfaces

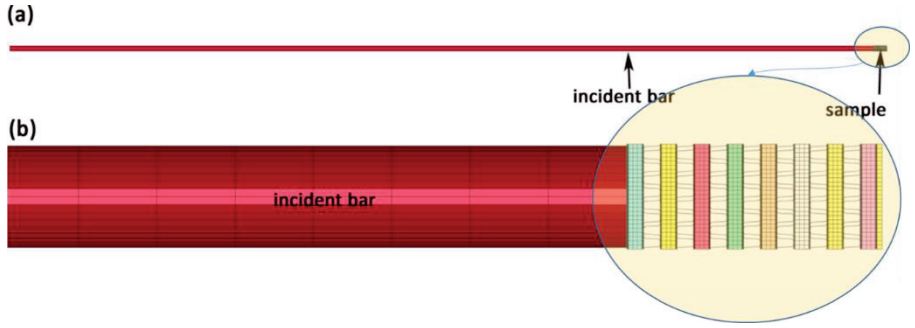


Figure 4.6. (a) Taylor impact test model and (b) specimen bar interfaces

The Inconel 718 incident, transmitter and striker bars were modeled using MAT01_ELASTIC material model with E=207 GPa, $\nu$=0.33 and $\rho$=7850 kg m$^{-3}$. The aluminum and wood striker bars were modeled using MAT01_ELASTIC material model; E=71.7 GPa, $\nu$= 0.33, $\rho$=2810 kg m$^{-3}$ for aluminum and E=2.2 GPa, $\nu$=0.33, $\rho$=725 kg m$^{-3}$ for wood [7]. The static and dynamic friction coefficients were set sequentially to 0.3 and 0.2 in all contact definitions, except SHPB impact testing. As the surfaces of the bars were lubricated with grease in the SHPB test, the static and dynamic friction coefficients were taken 0.2 and 0.1, respectively. The stresses on the transmitter and incident bar were calculated in the models at the same location with the strain gages in the experimental set-up.

# CHAPTER 5

# RESULTS

## 5.1. Quasi-Static Tests and Models

The quasi-static stress-strain curves of the tested corrugated samples at $4.8x10^{-3}$ m $s^{-1}$ corresponding to the strain rate of $10^{-1}$ $s^{-1}$ are shown in Figure 5.1. As similar with cellular metal structures such as aluminum foams and aluminum honeycombs, the tested 1050 Al multi-layer corrugated structure shows three distinct deformation regions under compression. These are (i) elastic, (ii) plateau and (iii) densification region. At very low strains, the sample deforms elastically till about an initial peak or crushing stress in the elastic region. In the post-initial peak stress region, the stress oscillates between the peak and valley stresses, resulting from the collapse of layers individually or collectively until about a densification strain. In the densification region, the stress values increase sharply as all-collapsed layers are compressed together. The initial peak stress at $4.8x10^{-3}$ m $s^{-1}$ varies between 1.2 and 1.30 MPa with an average of 1.25 MPa (Figure 5.1). The means stress, $\sigma_{crm} = \frac{\int \sigma d\varepsilon}{\varepsilon}$, is determined at 0.4 strain and varies between 0.96 and 1 MPa with an average of 0.98 MPa. The densification strain at quasi-static velocity is determined by the intercept method [40]. A tangent line is drawn to the densification part of the stress-strain curve and the intercept of this line with the mean crushing stress is taken as the densification strain. The densification strain by this method is found 0.67 as seen in Figure 5.1. The experimental densification strain is lower than the theoretically calculated densification strain based on an S-shape folding of fin walls. The complete compression of a S-shape folding of a fin layer having a height of 3.2 mm results in a final thickness of 0.7 mm, which will induce a final layer strain of 0.78 (3.2-0.7/3.2). Note that in this calculation it is assumed that all layers are folded through S-shape and fully compacted.

Figures 5.2(a-d) show the stress-strain and mean stress-strain curves and the densification strain of the perfect model I, perfect model II, one layer imperfect model and two layer imperfect model, respectively. All models result in initial peak stresses higher than the tests; while, the perfect model exhibits the highest initial peak stress

(2.26 MPa) which is 1.8 times that of the test. The lowest initial peak stress is found in the two layer imperfect model as seen in Figure 5.2(d). The insertion of an imperfect layer reduces the initial peak stress, but the perfect model II which is made up all bent layers shows both reduced initial peak stress and mean stress (Figure 5.2(b)). As seen in Figures 5.2(a-d), all models show the same densification strain, 0.76, which is higher than that of the tests but near the theoretically calculated densification strain. Above results show that the perfect model II and imperfect models well approach the experimental initial peak stress, while the perfect model I shows well agreements with experimental mean stress.

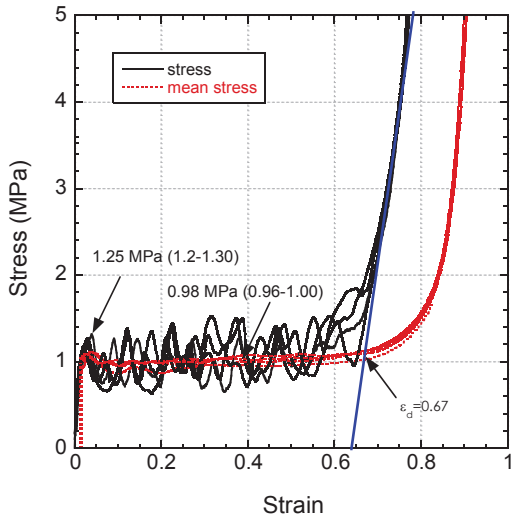


Figure 5.1. Quasi-static stress-strain and mean stress-strain curves and densification strain of 19.40 mm diameter sample at $4.8 \times 10^{-3}$ m $s^{-1}$

The experimental and numerical pictures of the samples deformed until about 0, 0.2, 0.4, 0.6 and 0.8 strains are shown in Figures 5.3(a-d), respectively. The collapse in the test starts from one of the mid-section layers (shown by arrows in Figure 5.3(a)).The collapse then proceeds discretely by the crush of layers near the bottom and top sections (Figure 5.3(a)). As the layers continuously crush, the specimen starts to bend as early as 0.2 strain as seen in Figure 5.3(a). In the perfect model I and perfect model II, following the elastic loading, the plastic collapse starts from the bottom and top section layers and continues progressively to the mid-section layers (Figures 5.3(b) and (c)). In the perfect model II (Figure 5.3(c)), the layers are inclined to the loading axis at 0.2 strain, resulting in specimen bending. In the one layer imperfect model, the initial collapse starts at the 10th layer (imperfect layer), then continues with the crush of upper layers.

The deformation proceeds progressively but not sequentially to the mid-section layers. It is noted that the mid-section layers deform at the final stage of the deformation near the densification strain. Although layers are sheared in this model, no global bending of the specimen is observed. In the two layer imperfect model, the collapse starts again from the imperfect 10th and 2nd layers (Figure 5.3(d)). The further collapse occurs at the mid and top section layers. The bottom section layers deform again at the later stages of the deformation. The bending of the specimen is seen at a strain of 0.4. The corrugated layers are also inclined to the loading axis caused by the bending of the specimen. The initial crushing stress, mean stress, densification strain and the layer crushing sequence of the tests and models are listed together in Table 5.1.

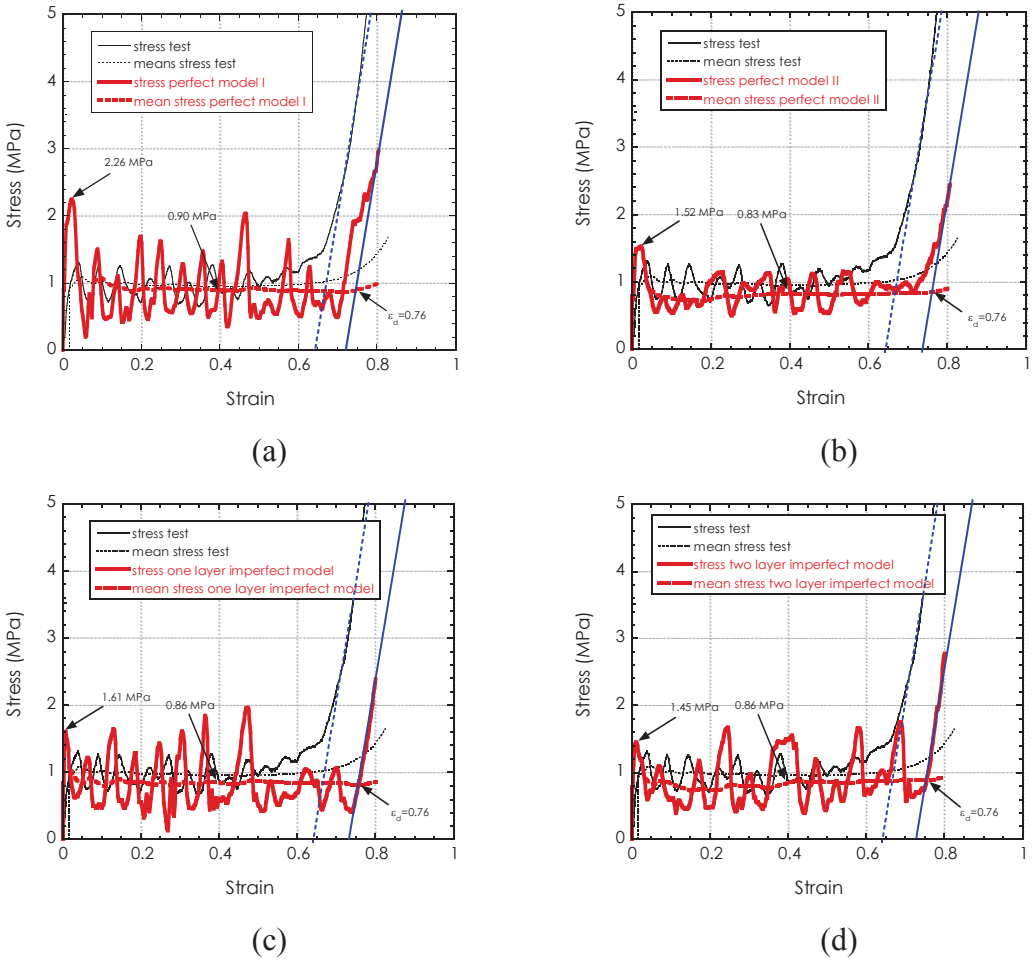


Figure 5.2. The comparison of test and model stress-strain, mean stress-strain curves and densification strains: (a) perfect model I, (b) perfect model II, (c) one layer imperfect model and (d) two layer imperfect model

a

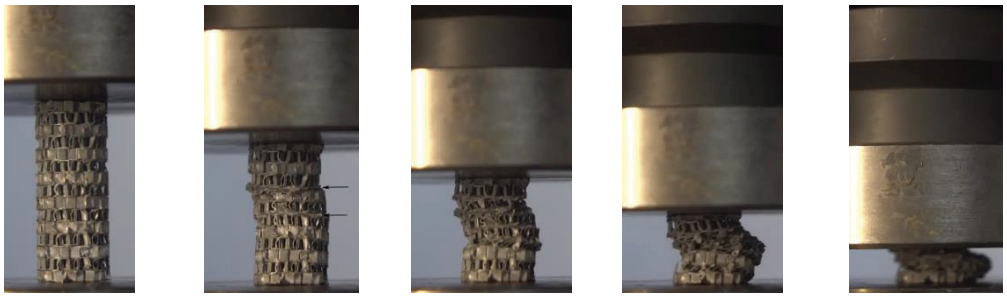

b

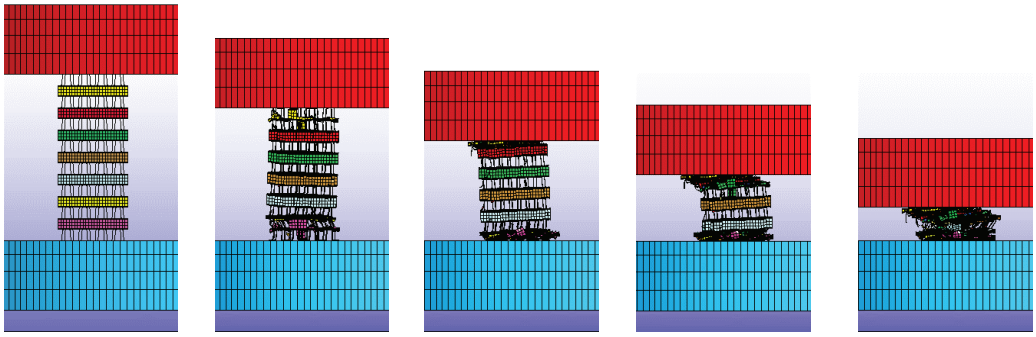

c

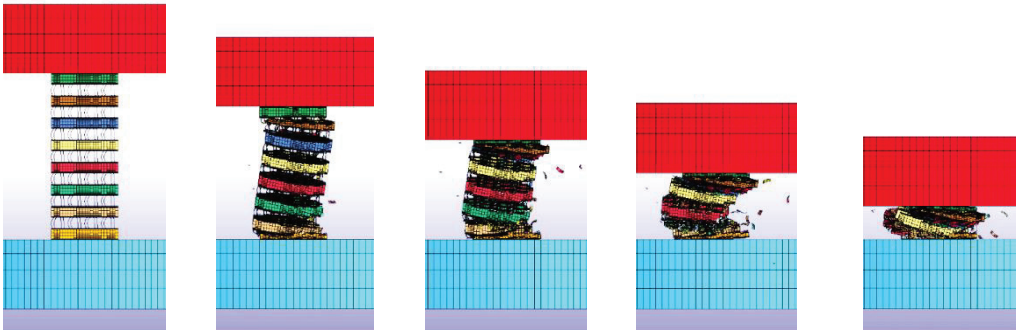

d

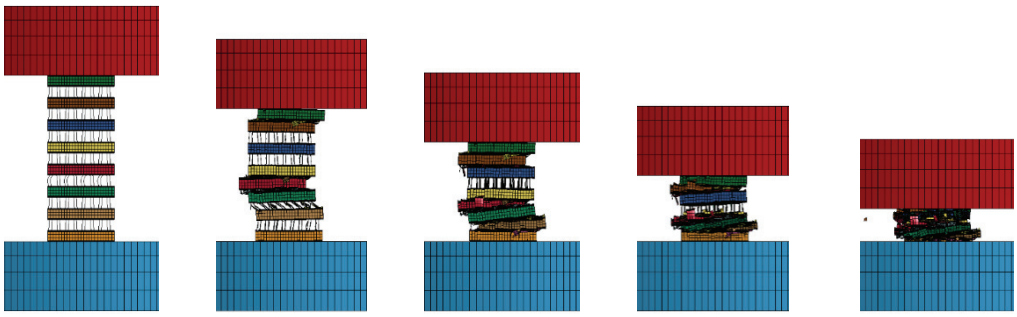

**(cont. on next page)**

e

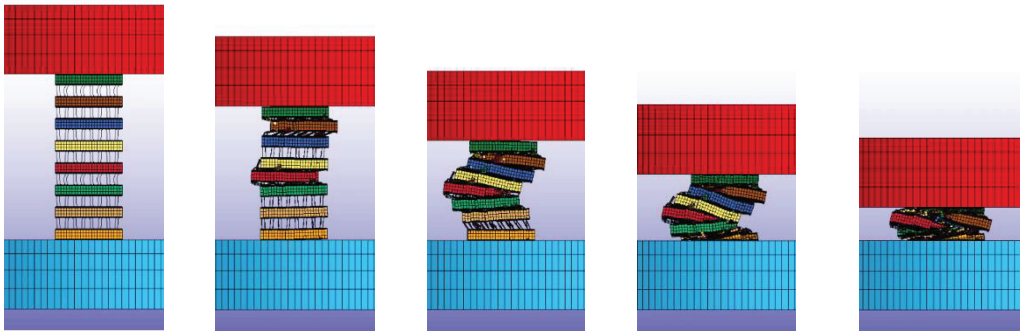

0 0.2 0.4 0.6 0.8

Figure 5.3. Deformed pictures of 19.40 mm corrugated sample at various strains at $4.8x10^{-3}$ $s^{-1}$ (a) test, (b) perfect model I, (c) perfect model II and (c) 10th layer and (e) 2nd and 10th layer imperfect models (cont.)

Table 5.1. The experimental and numerical initial crushing stress, mean stress, densification strain and the layer crushing sequence of the corrugated core at $4.8x10^{-3}$ m $s^{-1}$

| **Property** | $\sigma_{cr}$ (MPa) | $\sigma_{crm}$ (MPa) at 0.4 strain | $\varepsilon_d$ | Layer crushing sequence |
|---|---|---|---|---|
| **Test** | 1.25 | 0.98 | 0.67 | 9, 5,6 5, 11, 7,11,3-9 |
| **Perfect model I** | 2.26 | 0.90 | 0.76 | 13,2,11,14,1,3,15,3,5,6 |
| **Perfect model II** | 1.52 | 0.83 | 0.76 | 14,3,2,15,4 |
| **One layer imperfect model** | 1.61 | 0.86 | 0.76 | 10,2,8,12,14,4,6,9 |
| **Two-layer imperfect model** | 1.45 | 0.88 | 0.76 | 10,8,2,4,12,6,14 |

## 5.2. Split Hopkinson Pressure Bar Tests and Models

Split Hopkinson Pressure Bar tests were performed at two different velocities using 75 and 50 cm long Inconel striker bars. The velocity of the striker bar is 6 m $s^{-1}$ for 75 cm and 10 m $s^{-1}$ for 50 cm long striker bar. The final attained strain and hence displacement of the specimen in a SHPB test is limited by the incident and transmitter bar lengths. The final attained strain in a single loading of the investigated corrugated core is very small, ~0.03. To induce larger strains in a single shut, the bar lengths should be very long. Anyway, the tests are able to show the initial crushing stresses.

Figures 5.4(a) and (b) show the representative experimental and model (two layer imperfect model) incident and transmitted stresses at 6 and 10 m $s^{-1}$ as function of time, respectively. The oscillations in the transmitted stress in the same figures are due to the noise of the data acquisition system measuring relatively small strains. Nevertheless, the stress variations are detectable during the course of deformation and the experimental stresses are also comparable with the model stresses. The model and experimental incident wave stresses are also very much similar despite the small differences between them, both reaching a maximum stress of 113 MPa at 6 m $s^{-1}$ and 197 MPa at 10 m $s^{-1}$. The intricate stress profiles seen in Figures 5.4(a) and (b) are because of the stress wave reflections from the bar's free ends, as well as the stress transmissions and reflections at/from the specimen-bar interfaces. The length of the incident bar is 3110 mm and the transmitter bar is 2050 mm. The strain gage location is 1000 mm away from the incident bar-transmitter interface. Taking the wave velocity of the bar material 4930 m $s^{-1}$ gives a time duration of 427 μs for the wave to reach the strain gage location. The stress of incident bar is seen starting nearly at 400 μs in Figures 5.4(a) and (b).

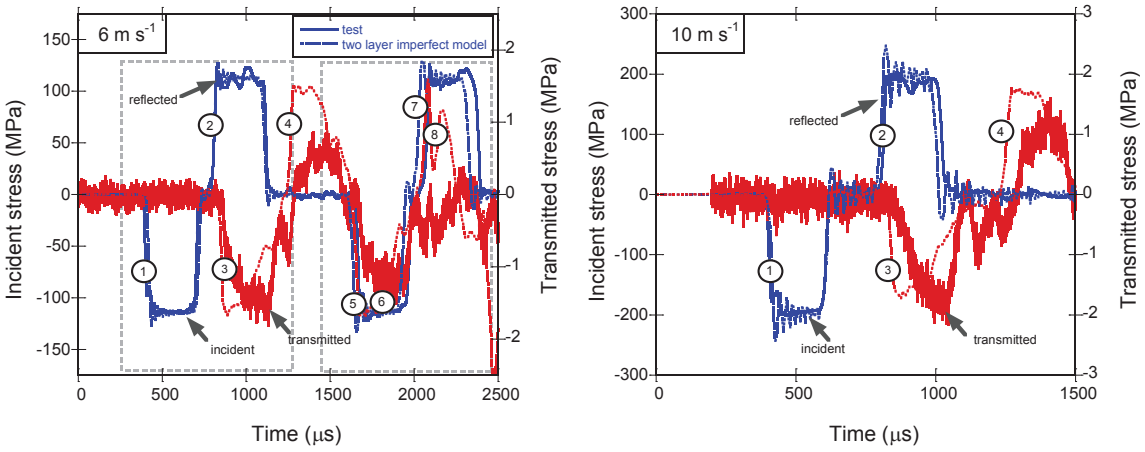


(a) (b)

Figure 5.4. The representative experimental and model (two layer impact model) SHPB incident and transmitted stresses as function of time at (a) 6 and (b) 10 m $s^{-1}$

In order to see wave propagation in the test duration, t-x diagram is drawn and shown in Figure 5.9. The locations of the strain gages are marked with the lines in the same graph. The full lines in the same graph are compressive, while dotted lines are the tensile stress waves. The numbered waves in Figure 5.5 correspond to the numbered waves in Figures 5.4(a) and (b). The first wave in Figure 5.5 is the incoming incident

compressive wave, which is reflected as tensile wave to the incident bar, number 2, and transmitted as compressive wave to the transmitter bar, number 3. The transmitted compressive wave returns back as tensile wave to the incident-transmitter bar interface, number 4. Since the tensile wave is a separating wave, it returns back from the specimen bar interface as a compressive wave, number 6 in Figure 5.9. Approximately at the same time, the tensile wave (number 2) on the incident bar returns back as compression wave to the incident bar, number 5, in the same figure. Since the specimen is not completely separated from the incident bar, this returned wave reloads the specimen transmitting a compressive wave (number 8) to transmitter bar and reflecting a tensile wave to the incident bar (number 7). This sequence of loading continues during a testing at least 30 times determined from the high speed camera records. Every ~1200 μs the sample is compressed repeatedly with a duration of 325 μs following an elastic relaxation after each repeating loading (the difference between the starting times of first and second incident waves gives 1200 μs). In Figure 5.4(a), each dotted rectangle shows the region of the specimen loading within recorded time domain of the deformation. The specimen is therefore two times loaded in Figure 5.4(a) and only one time is loaded in Figure 5.4(b). As the strain gages measure both incoming and going waves, the separation of these waves on the specimen is rather difficult; therefore, only the first loading will be used to determine stress-strain and stress-time profile of the tested specimens. There is also a time shift between the test and model waves as seen in Figures 5.4(a) and (b). The model stress values are extracted from an element at a distance from the incident-specimen/specimen-transmitter bar interfaces, nearly the same as the experiments. Since the size of the element used to collect the stress data in the model and strain gage in the tests is different, a small time shift unavoidably occurs between them. Furthermore, the specimen geometry and surface flatness in the model are perfect, while these are not perfect in the test specimen.

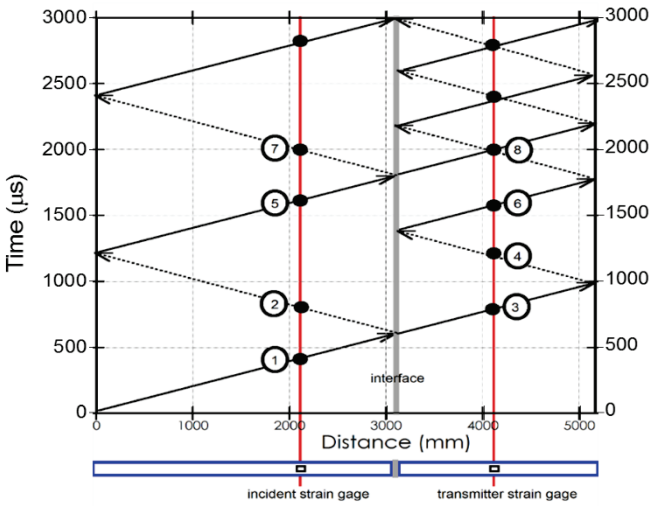


Figure 5.5. t-x diagram of the SHPB dynamic test

The stress-strain and strain rate-strain curves of the tests at 6 and 10 m $s^{-1}$ are shown sequentially in Figures 5.6(a) and (b) together with the quasi-static stress-strain curve. The stress, strain and strain rate in these curves, both in the tests and models, were calculated using the SHPB data reduction equations given in Chapter 3. The final strains attained in the first loading of the tests are relatively small, corresponding nearly to the initial peak stress strain values, ~0.03. But the SHPB stresses at both velocities are greater than that of quasi-static. The average initial peak stress (3 tests) is 1.49 MPa at 6 m $s^{-1}$ and 1.65 for 10 m $s^{-1}$. The strain rate at both velocities is also nearly constant and 115 and 185 $s^{-1}$ at 6 and 10 m $s^{-1}$ respectively. Figures 5.6(c) and (d) show the numerical stress-strain and strain rate-strain curves at 6 and 10 m $s^{-1}$, respectively. The numerical stress-strain and strain rate-strain curves in Figures 5.6(c) and (d) were determined again using the SHPB data reduction equations. In the same figures, the experimental SHPB and quasi-static stress-strain curves are also shown for comparison. The used numerical models show almost the same strain rate-strain profiles at both velocities, while numerical strain rates are slightly higher than that of the test at 10 m $s^{-1}$ (Figure 5.6(d)). The numerical final attained strains are also slightly higher at both velocities. The maximum stress for each model is also shown in Figures 5.6(c) and (d). The maximum stresses are sequentially 2.35, 1.67, 1.80 and 1.66 MPa at 6 m $s^{-1}$ and 2.52, 1.88, 1.72 and 1.72 MPa at 10 m $s^{-1}$ for perfect model I, perfect model II, one layer imperfect model and two layer impact model, respectively. It is noted that although the perfect models show increasing and flat stress-strain behavior, the imperfect models show decreasing stress values after the initial peak stress showing the

early strain localization in these models. The perfect model II and imperfect models also show comparable peak stress values with the tests, 1.49 and 1.65 MPa at 6 and 10 m $s^{-1}$, respectively. The initial peak stress values are also seen to increase with increasing velocity from 6 to 10 m $s^{-1}$. The experimental and numerical deformation pictures of the corrugated sample at the end of first and second loadings are shown in Figures 5.7(a) and (b) for 6 and 10 m $s^{-1}$, respectively. In 6 m $s^{-1}$ test, the strain localization in the tests just starts in layer 10 in the first loading and the localization in this layer continues in the second loading (Figure 5.7(a)). In the fourth loading, the strain localization is also seen in layer 7. The layer collapse in the SHPB tests is therefore not sequential as in the case of quasi-static test.

In the first and second loading of the perfect models, sequentially layer 14 and 2 for perfect model I and layer 13 and 3 for perfect model II (the layers near the incident and transmitter bar interfaces) rotate by shearing (Figure 5.7(a)). The shear induced rotations are more clearly seen in the second loading. In the imperfect models at 6 m $s^{-1}$, the imperfect layer 10 collapses in the first loading, while layer 2 starts to collapse in the two layer imperfect model in the second loading. The layer collapse starts in layer 12 in the first loading and continuous in the second loading at 10 m $s^{-1}$ (Figure 5.7(b)). The collapse of layer 10 also starts in the second loading and well develops in the fourth loading. As similar with the test at 6 m $s^{-1}$, the layer collapse is not sequential at this velocity. In the perfect models, the layer collapse proceeds with the rotation and shearing of the layers. In the perfect model I, collapse occurs in layer 12 and 3 and in the perfect model II in layer 14 and 2. Again, layer 10 and layer 2 collapse in the first and second loading of the imperfect models (Figure 5.7(b)). The models show clearly discrete stain localizations in the layers as similar with the tests.

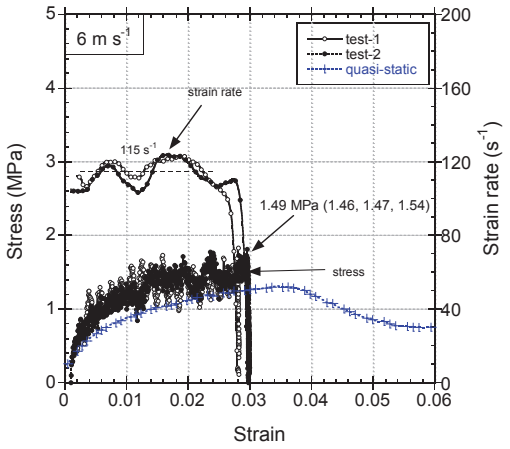


(a)

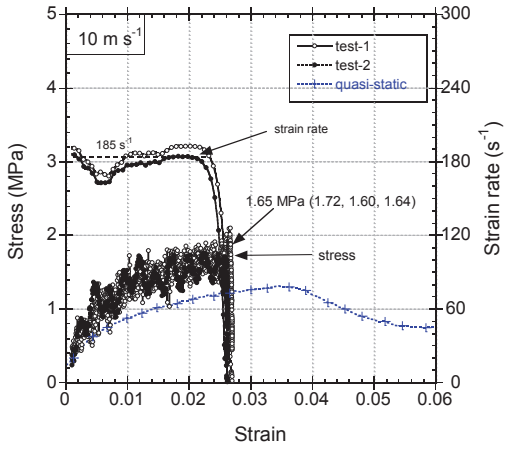


(b) **(cont. on next page)**

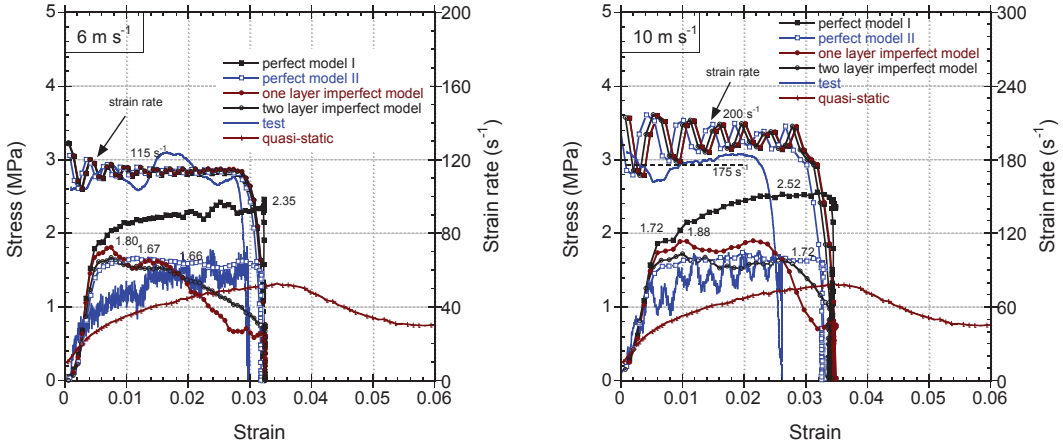


(c) (d)

Figure 5.6. The experimental stress-strain and strain rate-strain curves of the SHPB tests at (a) 6 and (b) 10 m $s^{-1}$ and the stress-strain and strain rate–strain curves of the SHPB models calculated using the SHPB data reduction equations (c) 6 and (d) 10 m $s^{-1}$ (cont.)

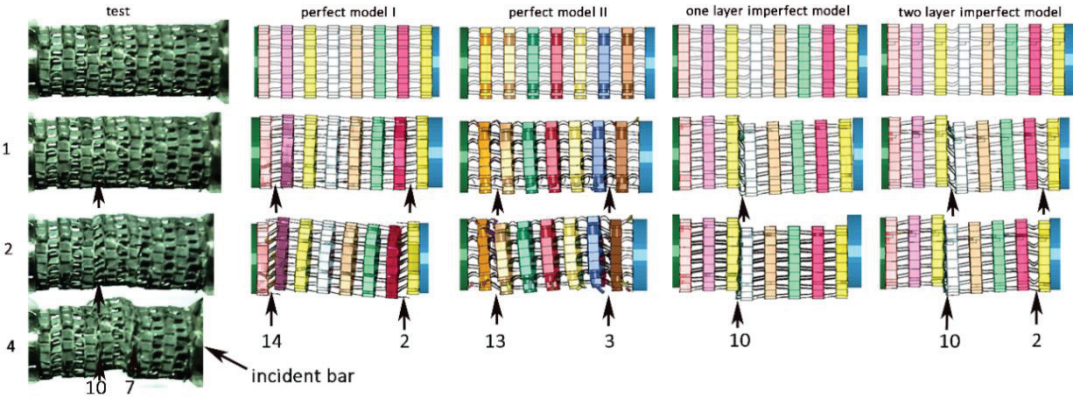


(a)

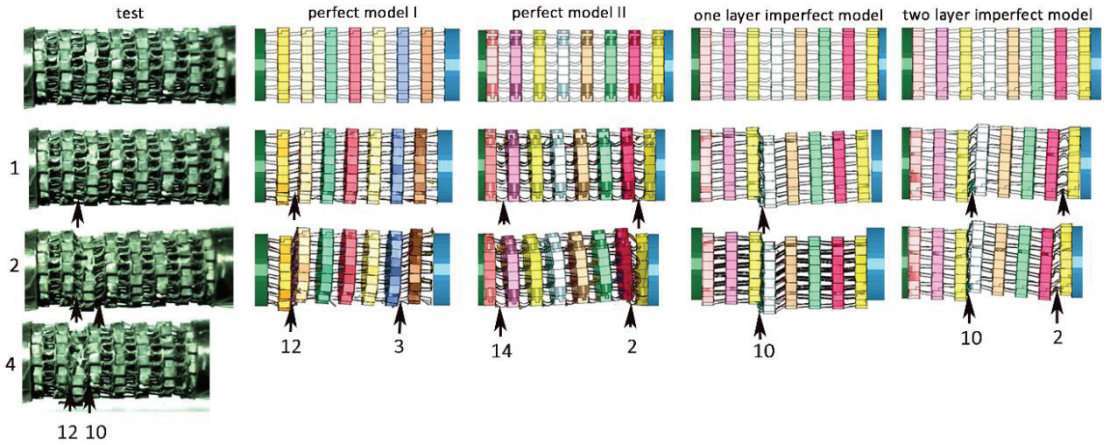


(b)

Figure 5.7. Test and numerical deformation pictures of the corrugated sample at the end of first, second and third loading at (a) 6 and (b) 10 m $s^{-1}$

Figures 5.8(a) and (b) show sequentially the perfect model I incident and transmitter bar stress profiles measured from the specimen interfaces and the ratio of incident bar stress to the transmitter bars stress as function of time at 6 and 10 m $s^{-1}$. The time difference between the starting points of the incident bar interface and transmitter bar interface stress, 40 μs, shows simply the transit time of the sample. The ratio of incident bar stress to the transmitter bar stress is initially high then it reaches one at 780 and 670 μs in 6 and 10 m $s^{-1}$ test, respectively. The ratio near one shows essentially the stress equilibrium; the incident and transmitted stresses become nearly equal to each other. The similar stress equilibrium was also found in the perfect model II and in the imperfect models. The stress-strain curves of models determined from the specimen-bar interfaces at 6 and 10 m $s^{-1}$ are shown in Figures 5.8(c) and (d), respectively. The stresses at the contacts were averaged and the strains were determined by the incident and transmitter bar displacements. This allowed to determine the stress and strain in the second and third loadings in the SHPB. The experimental stress-strain curves are also shown in the same figures. As is seen in Figures 5.8(c) and (d), the initial peak stress is reached in the first loading in all models.

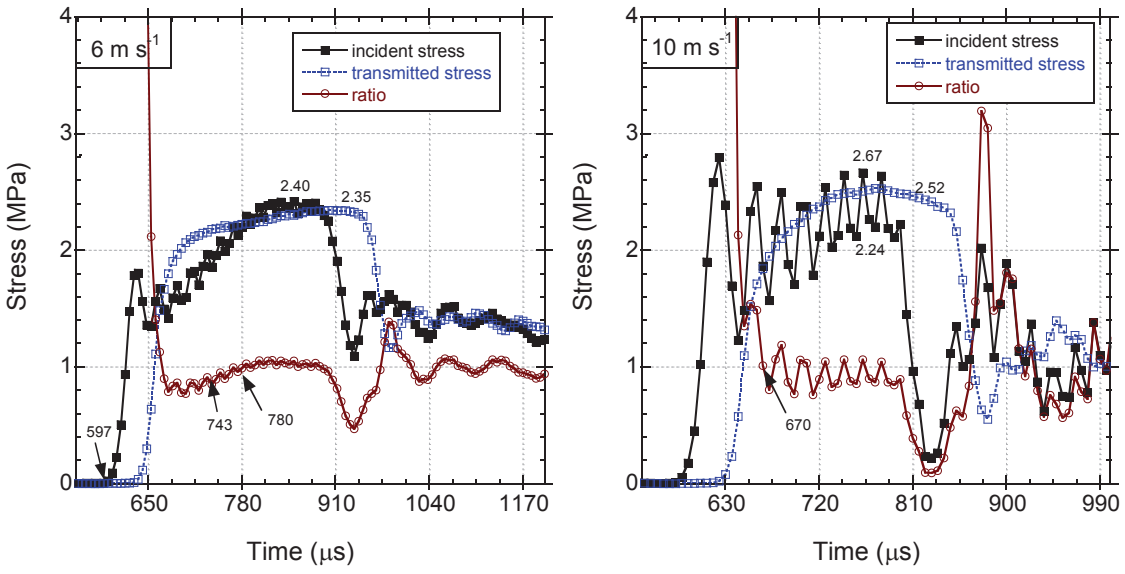


(a) (b)

**(cont. on next page)**

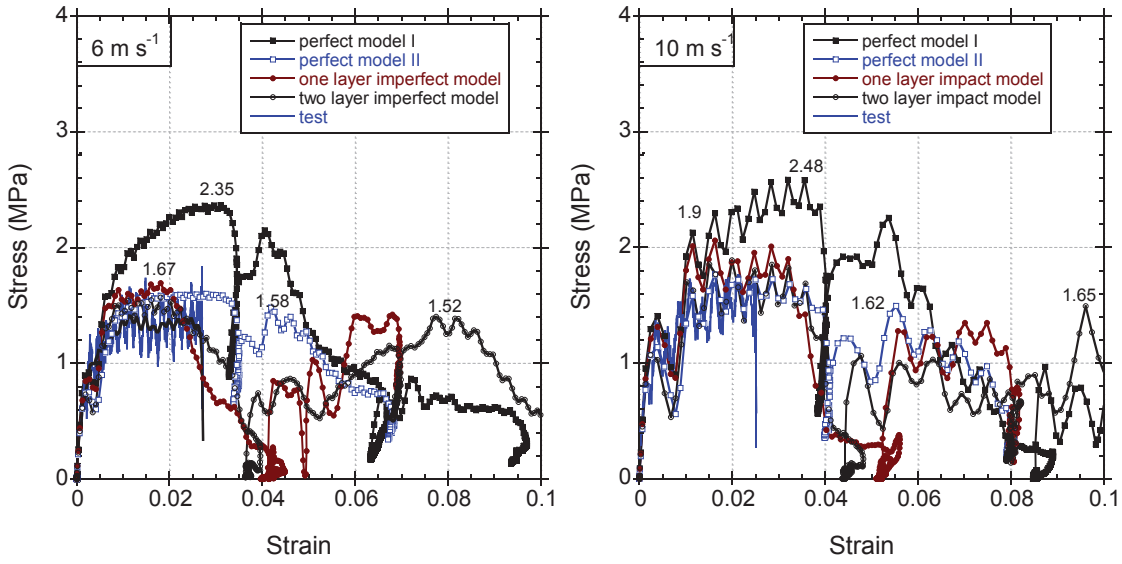


(c) (d)

Figure 5.8. The bar specimen interface incident and transmitted stresses and the stress ratio as function of time at (a) 6 and (b) 10 m $s^{-1}$ and the stress-strain curves of models determined from the specimen-bar interfaces at (c) 6 and (d) 10 m $s^{-1}$ (cont.)

## 5.3. Direct Impact Tests and Models

Direct impact tests were performed at 9, 22, 40, 60 and 90 m $s^{-1}$ using Inconel, aluminum and wood striker bars. Figure 5.9(a) shows the front and back gage stress-time curves of a single test at 9 m $s^{-1}$ using Inconel striker bar. Since the front gage is 300 mm and the back strain gage is 1810 mm away from the sample-incident bar interface, the front stress is shifted 60.8 μs (c= 4930 m $s^{-1}$) and the back stress is shifted 367 μs on the time axis to start the front and back strain gage stresses at the same time (0 μs). The distances between the end of the incident bar and strain gage locations are 1000 and 2810 mm for the back and front gage, respectively. The back gage stress, by a simple calculation using the wave speed of Inconel bar, 4930 m $s^{-1}$, starts to decrease and become tensile at 405.6 μs and the front gage stress starts to decrease at 1140 μs as the compressive stress wave is reflected from the free end of the incident bar. Because of the relatively low impedance of the corrugated sample, the reflected tensile wave returns back largely as the compressive wave to the incident bar at 1261 μs and the stress becomes again compressive. These calculated times based on Inconel bar wave velocity and distances between strain gage and bar ends perfectly match with the experimentally determined times as marked in Figure 5.9(a). Figure 5.9(b) shows the

front gage stress-time curves of three tests conducted at 9 m $s^{-1}$. The stress-time profiles of three tests are very much similar and show the stress reductions due to the reflected wave from the incident bar end at 1140 μs as shown in the same figure. An average initial peak stress is determined to be 1.7 MPa (Figure 5.9(b)). The average initial peak stress determined in the direct impact test at 9 m $s^{-1}$ is also very similar with the SHPB bar test at 10 m $s^{-1}$, 1.65 MPa. Figure 5.9(c) shows the deformation pictures of the corrugated sample at the time intervals of 300 μs (the time at which striker bar hits the sample is taken zero). The layer crushing although starts from the impacted end as marked by an arrow at 300 μs, the crushing is not sequential and it switches to the layers near the impact and distal ends as marked with arrows at 900 and 1200 μs. At the later stages of the deformation the sample bends because of the crushing of near and far layers, as similar with the quasi-statically and dynamically (SHPB) tested samples.

Figures 5.10(a), (b) and (c) show sequentially front gage stress-time graphs of three tests at 22, 40 and 60 m $s^{-1}$. On the same graphs, the average initial peak stresses are also shown. The average initial peak stresses are 1.83, 1.95 and 2.23 for 22, 40 and 60 m $s^{-1}$ tests, respectively. The initial peak stress at 90 m $s^{-1}$ is 2.17 MPa and shown in Figure 5.10(c). As is seen in Figures 5.10(a), (b) and (c), the tests are repeatable at all velocities; each test gives almost the same stress-time profile expect small variations between the stress values. The sharply increased stress part of the curves corresponds to the complete crushing of layers and subsequent compaction of the crushed layers. As the velocity increases the compaction becomes faster, giving rise to early rise of the stress values. Since the reflected wave from the end of the incident bar reaches the front strain gage at 1140 μs, the measured stress values, except 22 m $s^{-1}$, are not affected by the reflected waves. However, the effect of reflected wave is only effective at the later stages of the deformation near the compaction stage or rising part of the stress-time curve at 22 m $s^{-1}$. Figure 5.10(d) shows the representative stress-time profiles at quasi-static, 6, 22, 40, 60 and 90 m $s^{-1}$. The time scale for the quasi-static test is shown in Figure 5.10(d) is taken as millisecond instead of microsecond to make comparison with the dynamic tests. The initial peak stress increases from 1.25 MPa at quasi-static to 2.23 MPa at 60 m $s^{-1}$, while the initial peak stress almost remains constant at 90 m $s^{-1}$.

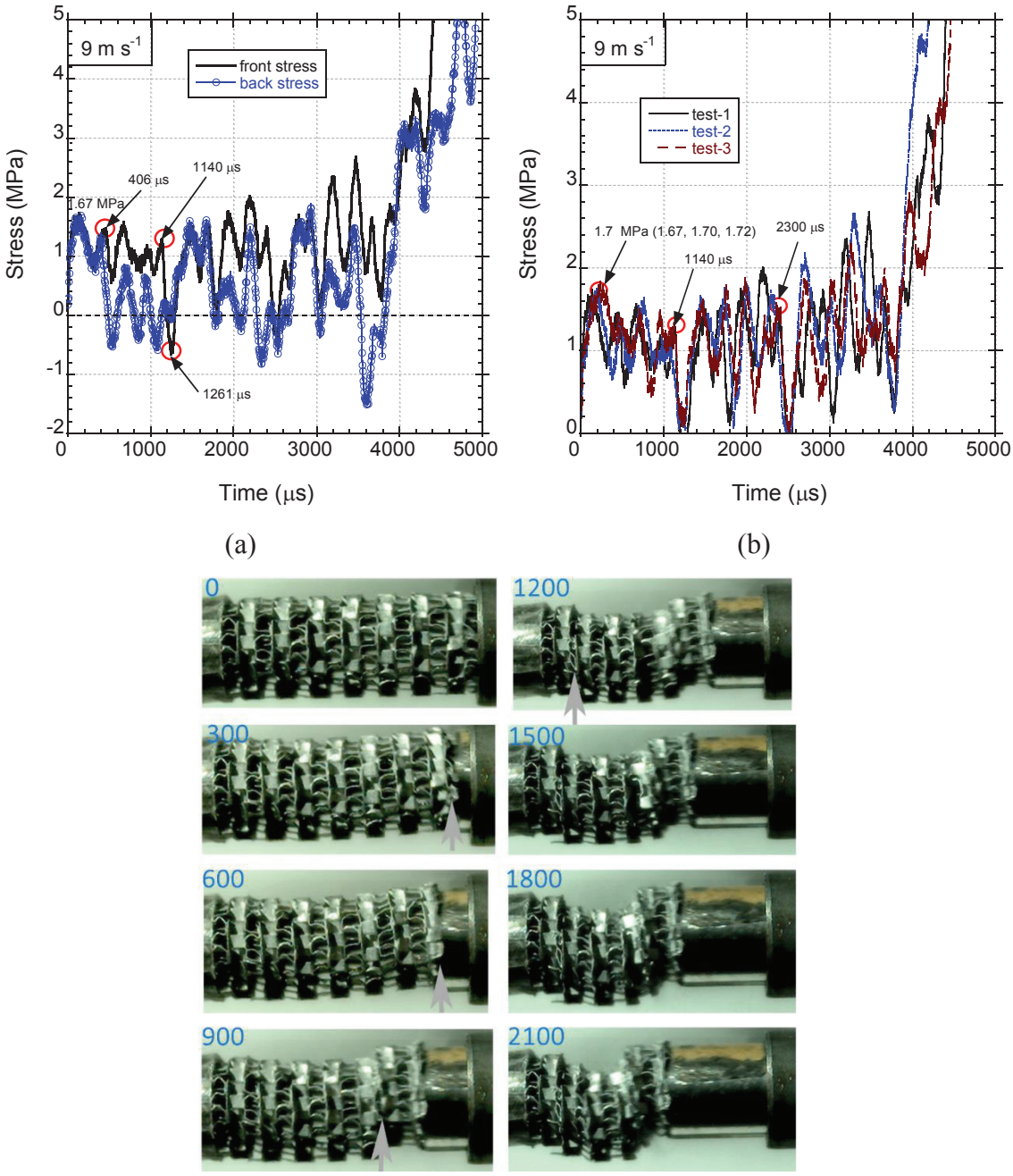


Figure 5.9. (a) front and back gage stress-time curves of single test, (b) front gage stress-strain curves of three tests and (c) the deformed pictures of the corrugated sample tested at 9 m $s^{-1}$ in the direct impact test (the numbers in the picture are in the time

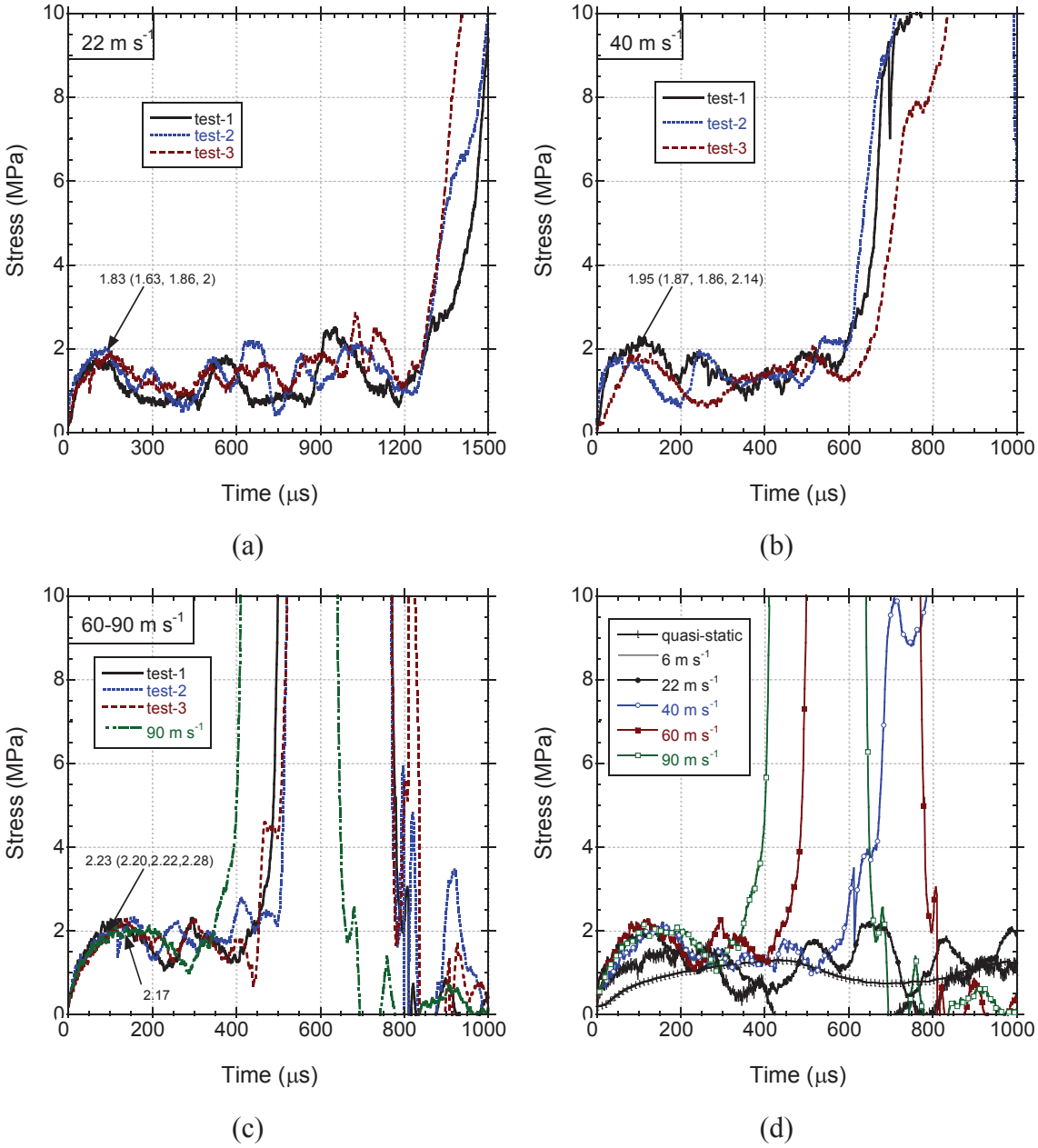


Figure 5.10. Stress-time histories of the direct impact tests at (a) 22, (b) 40 and (c) 60 m $s^{-1}$ and (d) stress-time histories from quasi-static to 80 m $s^{-1}$

Figures 5.11(a) and (b) show the experimental and the perfect model II and the two layer imperfect model front and back strain gage stresses at 22 m $s^{-1}$, respectively. Although, the back strain gage stresses of the experiment and perfect model II are very much similar, the perfect model II front gage stress deviates from the experiment after 600 μs and the numerical stress becomes tensile (Figure 5.11(a)). On the other side, both front and back strain gage stresses of the experiment and the two layer imperfect model show very similar trends at the same impact velocity shown in Figure 5.11(b).

The perfect model II and the two layer imperfect model numerical striker bar-sample and incident bar-sample contact stresses with the experimental front strain gage stress are shown sequentially in Figures 5.11(c) and (d). The time difference between the striker bar- and incident bar-sample contact stresses seen in Figures 5.11(c) and (d) corresponds to the wave transit time, 48 μs, for both models. Both models also show similar contact stresses, but the number of peak stress increase in the two layer impact model. The contact stresses between the striker bar-sample and the incident bar-sample are also very much similar, showing almost no effect of inertia. The experimental and perfect model II and two layer imperfect model deformed pictures of the corrugated sample at 22 m $s^{-1}$ direct impact test are shown in Figure 5.12. Experimentally, the layer crushing starts from the impact end, then layer crushing switches into mid-sections and rear ends. The layer crushing is progressive, but not sequential. This indicates that the deformation behavior is very much similar to that of the quasi-static deformation. The layer crushing in the perfect model II starts from the impact end, while the layers are crushed progressively. The layer crushing in the two layer impact model starts from the imperfect layers and proceeds with non-sequential manner. The numbers in Figure 5.12 show the time in microsecond. The time at which the striker bar hits the corrugated sample is taken as zero. Therefore; there may be same delay between the experimental and numerical times as the numerical starting time was determined exactly while the experimental starting time was determined from the picture frames ($\pm$ 100 $\mu s$).

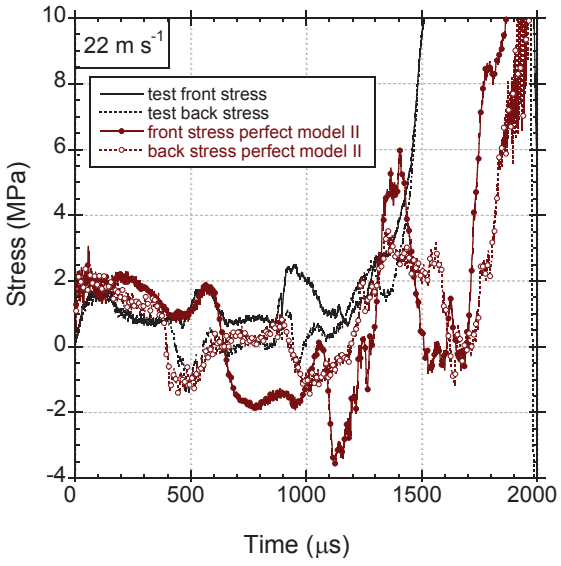


(a)

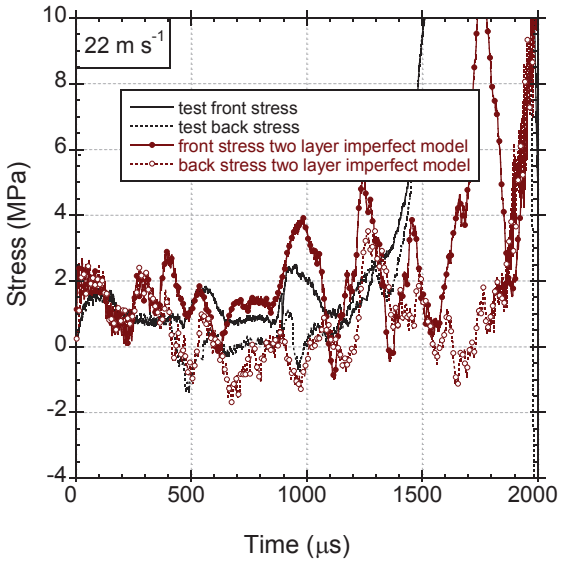


(b) **(cont. on next page)**

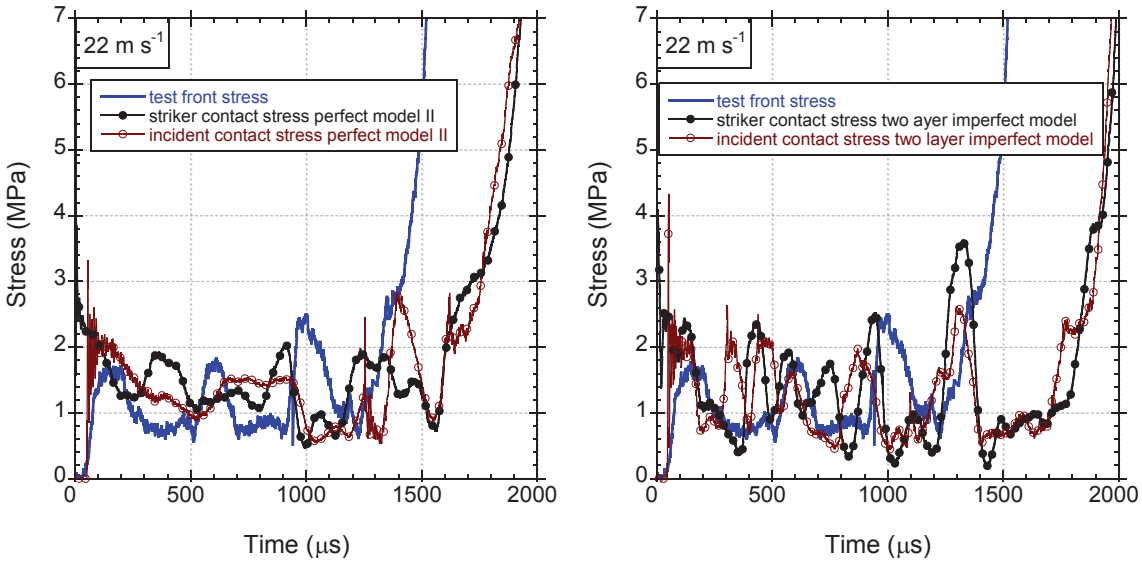


(c) (d)

Figure 5.11. The experimental and numerical front and back strain gage stresses (a) perfect model II and (b) two layer imperfect model, and the experimental front gage stress and striker and incident bar contact stresses (c) perfect model II and (d) two layer imperfect model (cont.)

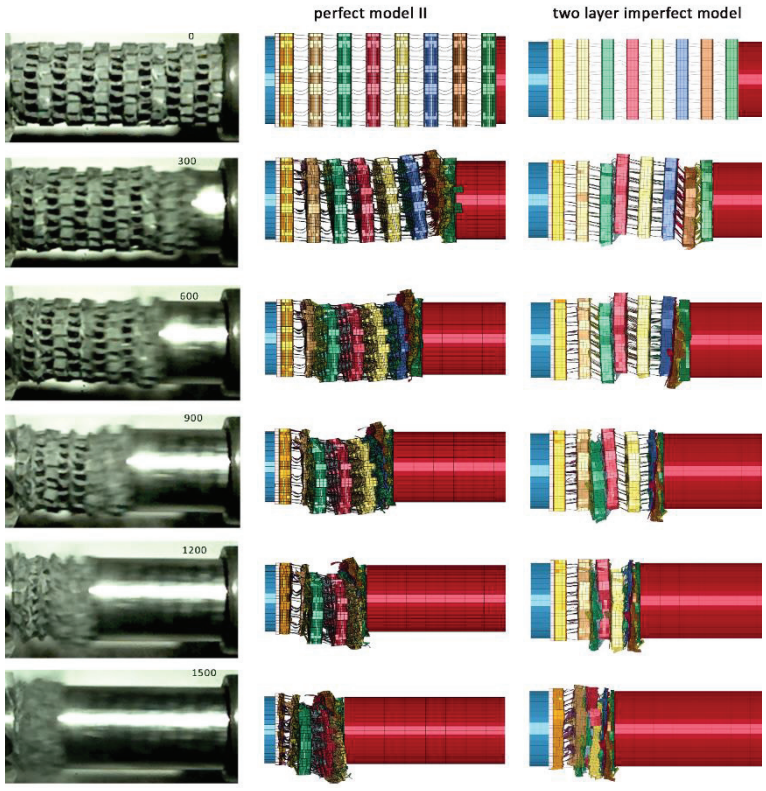


Figure 5.12. Experimental and perfect model II and two layer imperfect model deformed pictures of the corrugated sample at 22 m $s^{-1}$ direct impact test

Figures 5.13(a) and (b) show the experimental perfect model II and two layer imperfect model front and back strain gage stresses at 40 m $s^{-1}$, respectively. Although the perfect model II shows similar stress-time profile with the test, the front gage stress values become tensile after 600 μs (Figure 5.13(a)). The front and back strain gage stresses of two layer imperfect model are also very similar to those of the test (Figure 5.13(b)). The perfect model II striker bar-sample contact stress is slightly higher than that of the incident bar-sample at the beginning of the deformation. The incident bar contact stress shows no stress oscillation as opposed to striker bar contact stress (Figure 5.13(c)). The striker bar contact stress of two layer imperfect model is higher and shows larger magnitude of stress peaks than the incident bar contact stress as depicted in Figure 5.13(d). Although initially the layer crushing starts from the impacted end in the test, later the layer crushing switches to rear end and mid-sections, as similar with 22 m $s^{-1}$ test. Again, the layer crushing in perfect model II starts from the impacted end in a sequential manner, while the layer crushing in two layer impact model starts from the impacted end and imperfect layers and proceeds with non-sequential manner.

Figures 5.15(a-d) show the experimental, the perfect model I, perfect model II, one layer imperfect model and two layer imperfect model numerical front and back strain gage stresses at 60 m $s^{-1}$, respectively. It is noted in the same figures that the front and back strain gage experimental and numerical stresses are almost the same for all models, showing no effect of wave dispersion on the bars. The perfect model I and the one layer imperfect model predict initial peak stresses higher than that of the experiment (Figures 5.15(a) and (c)), while the perfect model II and the two layer imperfect model approach the experimental initial peak stress. Figures 5.16(a-d) show the perfect model I, perfect model II, one layer imperfect model and two layer imperfect model numerical striker bar-sample and incident bar-sample contact stresses together with the experimental front strain gage stress, respectively. The striker bar contact stresses are higher than the incident bar contact stresses in all models, while both contact stresses approach to each other near the end of the deformation. The higher striker contact stress is however more pronounced in the perfect model II as seen in Figure 5.16(b). The experimental layer crushing as shown in Figure 5.17 starts from the impact end and proceeds almost sequentially until about 300 μs; then it switches to non-sequential or diffusive mode. Numerically, the layer crushing also starts from the impact end as seen in Figure 5.17, while the deformation becomes non-sequential after 300 μs in the perfect model I and after 100 μs in the one and two layer imperfect

models. The layer crushing is however sequential during the course of deformation in the perfect model II.

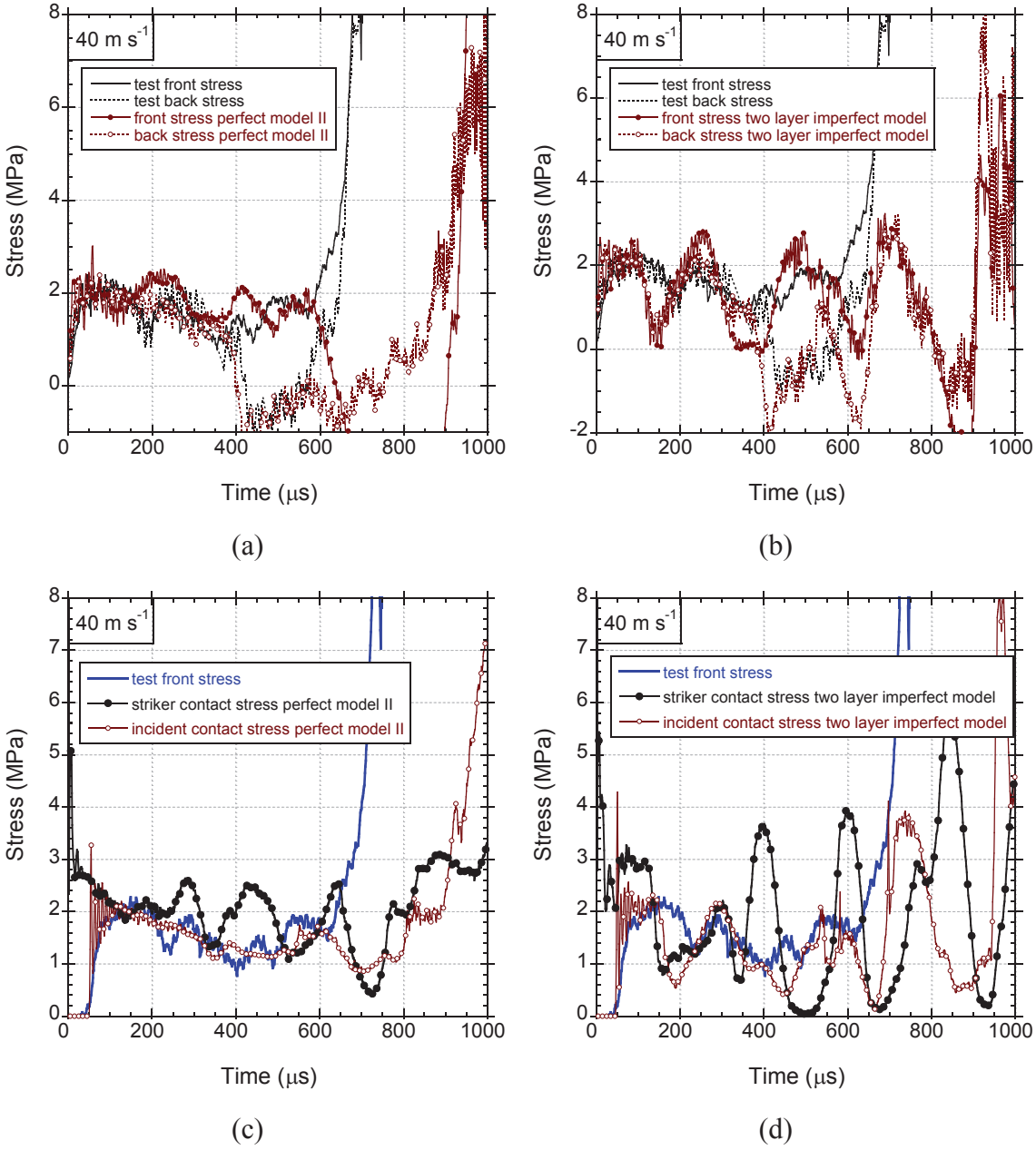


Figure 5.13. The experimental and numerical front and back strain gage stresses (a) perfect model II and (b) two layer imperfect model, and the experimental front gage stress and striker and incident bar contact stresses (c) perfect model II and (d) two layer imperfect model

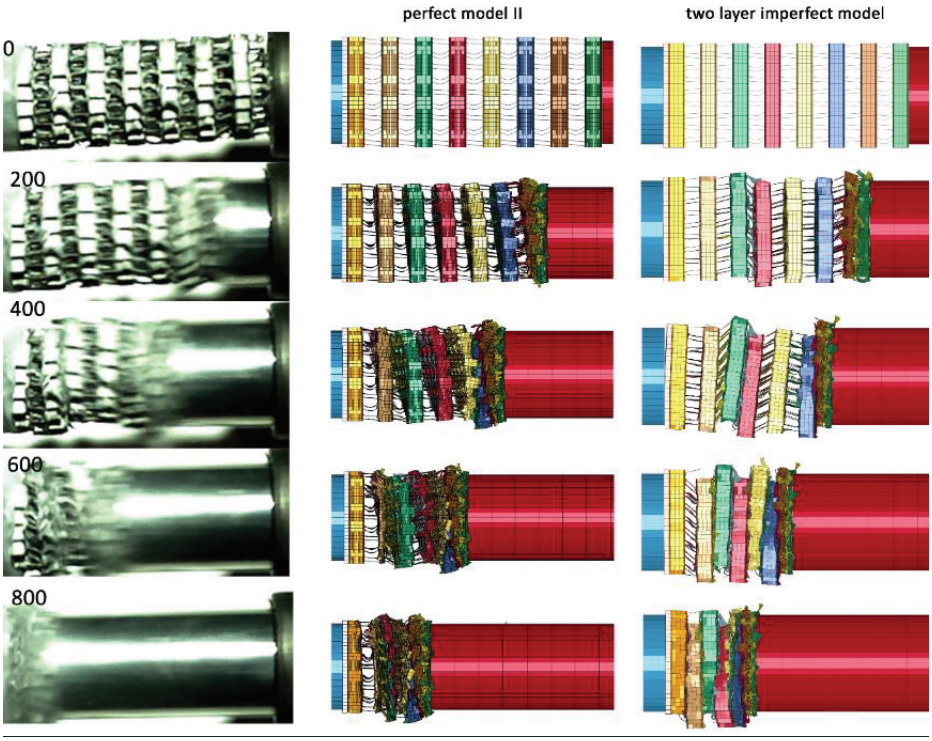


Figure 5.14. Experimental and perfect model II and two layer imperfect model deformed pictures of the corrugated sample at 40 m $s^{-1}$ direct impact test

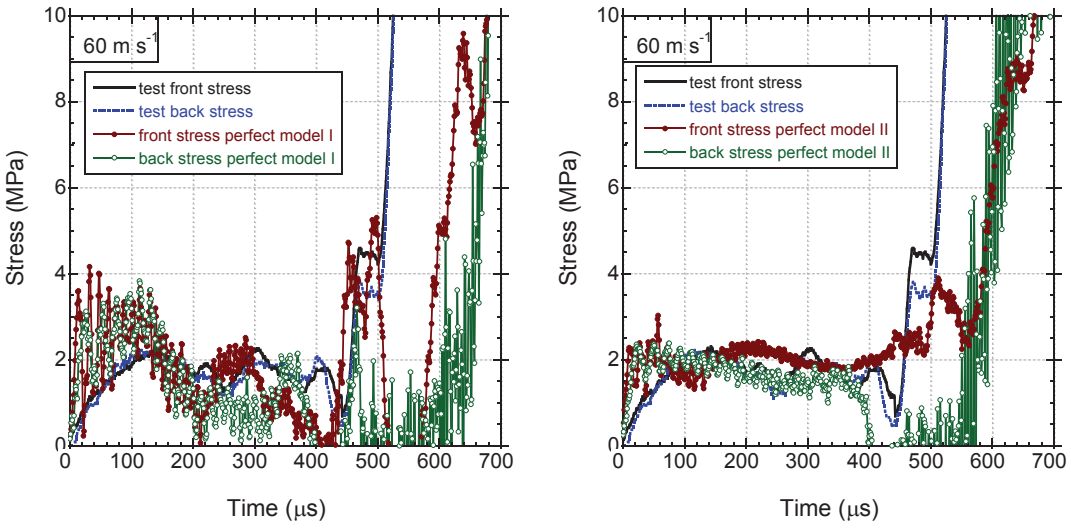


(a) (b) **(cont. on next page)**

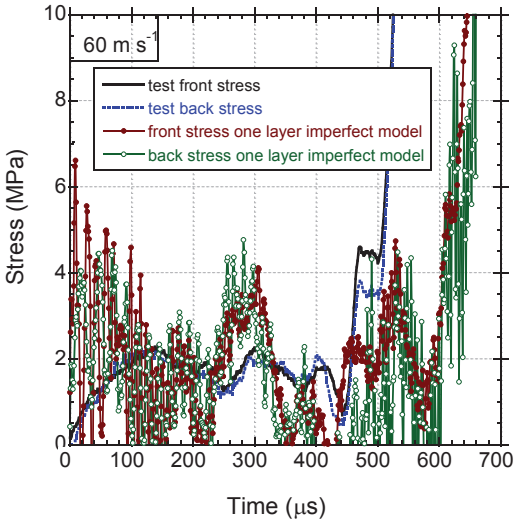


(c)

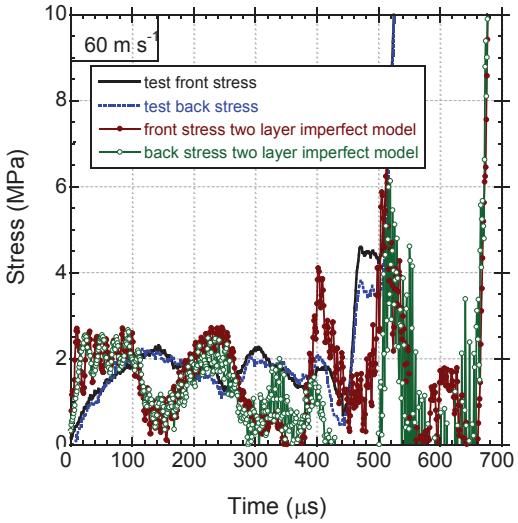


(d)

Figure 5.15. The experimentally and numerically measured front and back strain gage stresses and the numerical front and back strain gage stresses (a) perfect model I, (b) perfect model II, (c) one layer imperfect model and (d) two layer imperfect model (cont.)

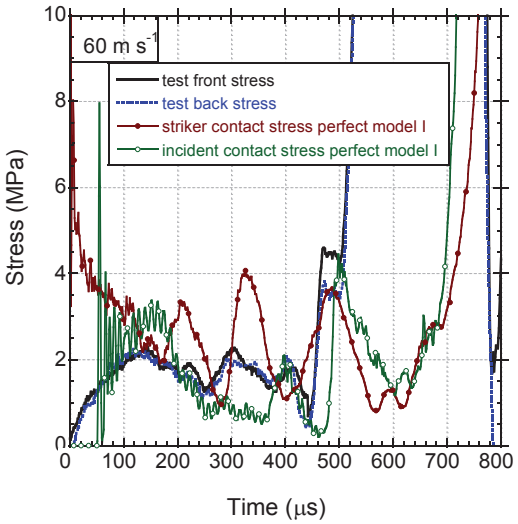


(a)

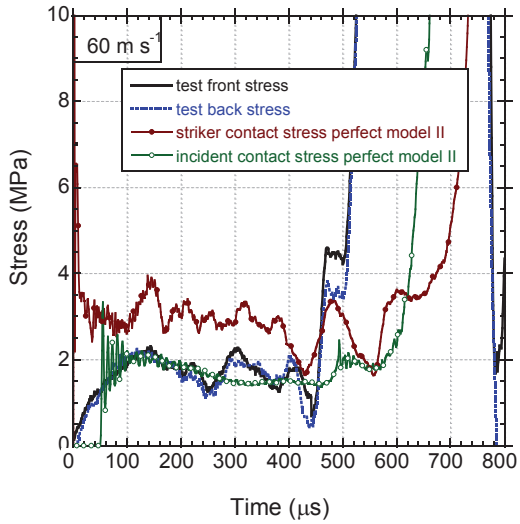


(b) **(cont. on next page)**

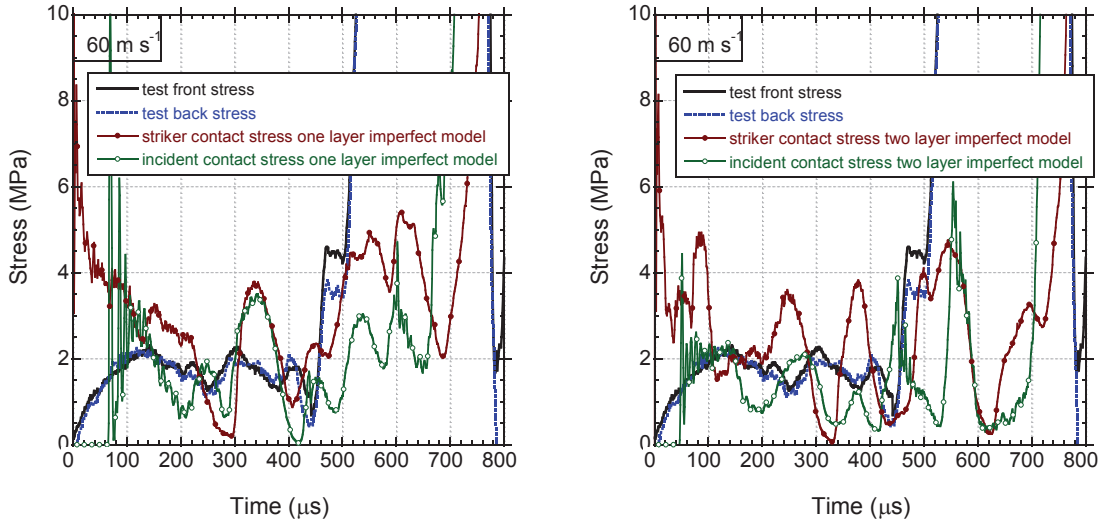


(c) (d)

Figure 5.16. The numerical stress-time profiles at the contacts between striker bar-sample and sample-incident bar; (a) perfect model I, (b) perfect model II, (c) one layer imperfect model and (d) two layer imperfect model. (cont.)

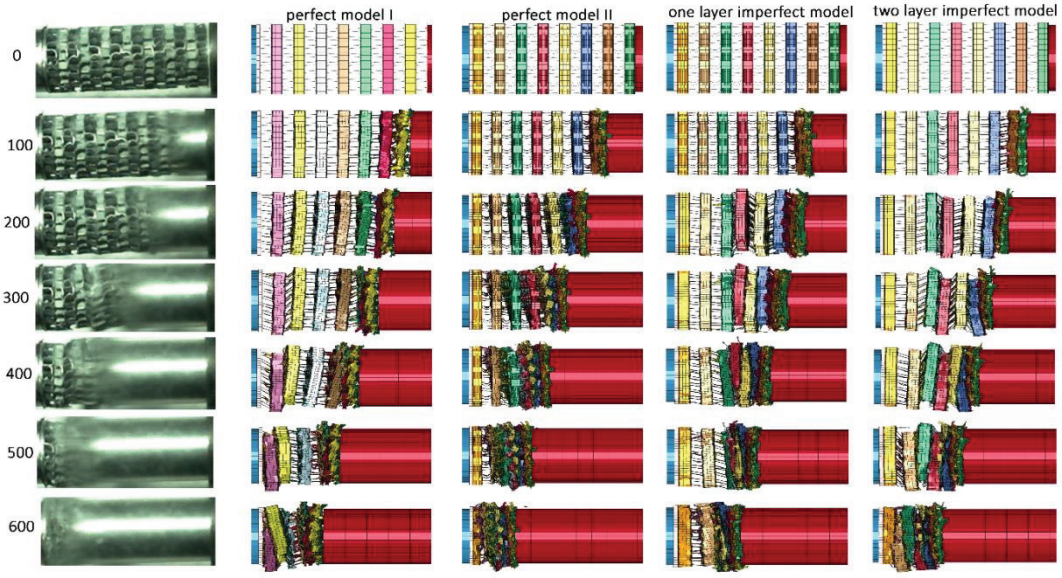


Figure 5.17. The experimental and numerical deformed pictures of the sample tested at 60 m $s^{-1}$

Figures 5.18(a) and (b) show the experimental, perfect model II and two layer imperfect model front and back strain gage stresses at 90 m $s^{-1}$, respectively. Both models predict the experimental crushing stress well. The stress oscillations seen in Figure 5.18(b) in the two layer impact model result from the crushing the imperfect layers; otherwise, the crushing stress will be almost constant as similar with the perfect model II. The striker bar- sample contact stress in both models are higher than that of

the incident bar-sample contact stress (Figures 5.18(c) and (d)). Again, larger stress drops seen in Figure 5.18(d) is resulted from the collapse of imperfect layers. The experimental deformation of the corrugated sample at 90 m $s^{-1}$ starts from the impact end and proceeds sequentially, showing shock formation as seen in Figure 5.19. The imperfect model deformation sequence shown in the same figure is very much similar with the experiment; layer crushing starts from the impact end and proceeds sequentially to the rear end of the specimen. While, the layer crushing in the two layer impact model starts from the impact end and it proceeds non-sequentially but in a diffusive mode as seen in Figure 5.19

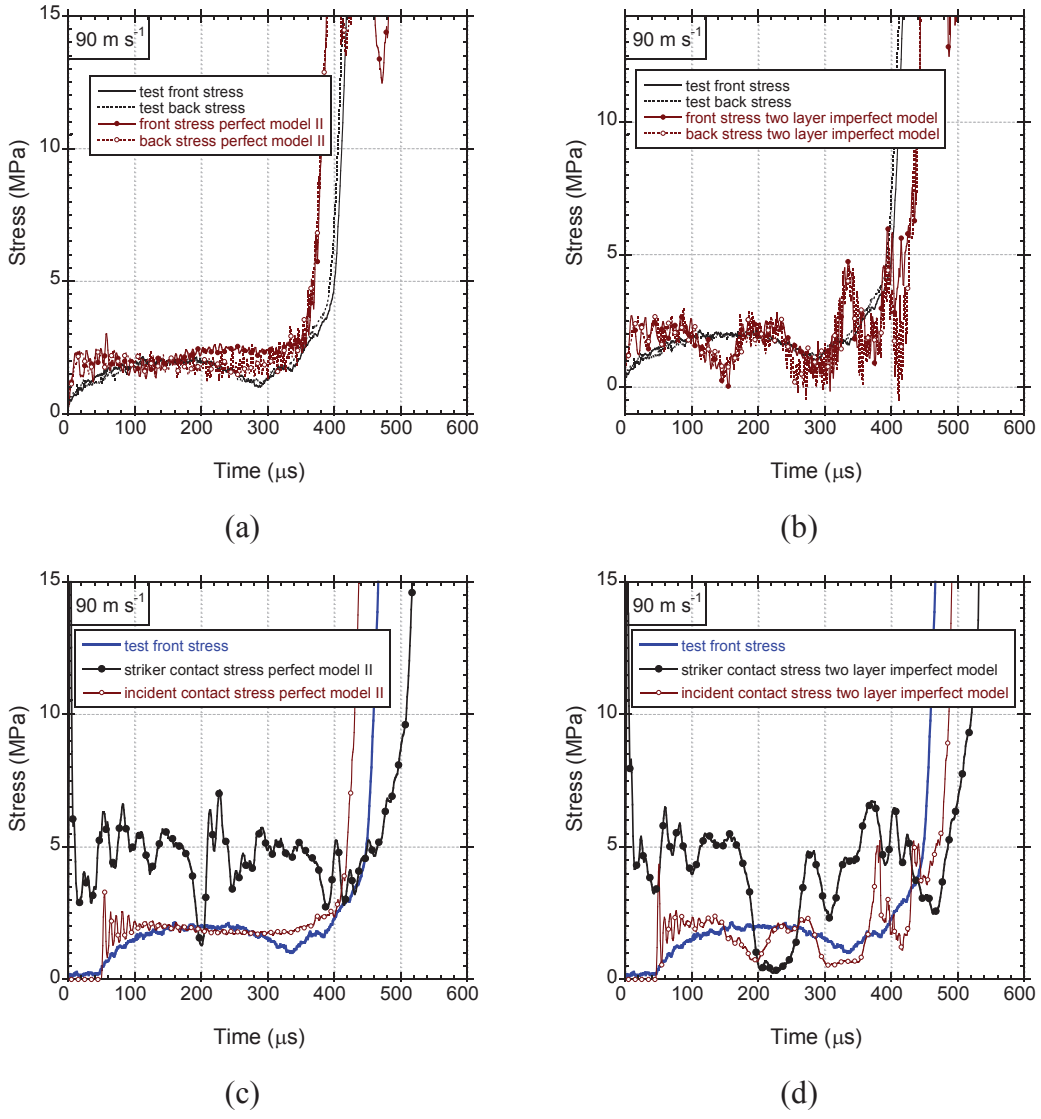


Figure 5.18. The experimental and numerical front and back strain gage stresses (a) perfect model II and (b) two layer imperfect model, and the experimental front gage stress and striker and incident bar contact stresses (c) perfect model II and (d) two layer imperfect model at 90 m $s^{-1}$ direct impact test

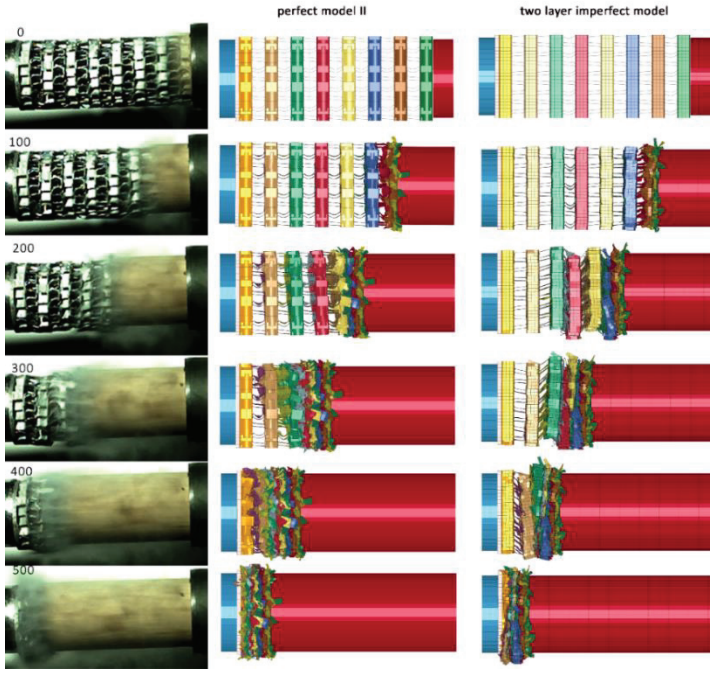


Figure 5.19. Experimental and perfect model II and two layer imperfect model deformed pictures of the corrugated sample at 90 m $s^{-1}$ direct impact test.

## 5.4. Taylor Impact Tests and Models

The Taylor-like impact tests were performed at 135, 150 and 200 m $s^{-1}$. The stress was calculated using the SHPB equations in Chapter 3. The strain in the incident bar was measured from both front and back strain gages. In the simulations, the stress was determined from the element whose location was the same with the strain gages in the incident bar. The corrugated samples were impacted with a 1 mm thick Al backing face sheet at the rear end (distal end).

Figure 5.20(a) shows the back gage stress-time profile of two samples tested at 135 m $s^{-1}$. The tests show very similar stress-time profiles as seen in the same figure, drawing the repeatability of the tests. Figure 5.20(b) shows the stress-time profiles measured by the front and back gages. The stress-time profiles measured by front and back gages are also very similar at this velocity. Similarly, the tests performed at 150 m $s^{-1}$ also show repeatable test results (Figure 5.20(c)) and similar front and back gage stresses (Figure 5.20(e)), while the front gage stress exhibits larger stress oscillations than the back gage stress (Figure 5.20(f)). The increased stress oscillations in the front gage stress are attributed to the release of the shear waves near the impact end, showing

3D stress wave propagation. Therefore, the stress-time profiles of the tests are compared with the numerical simulations using the back gage stress measurements.

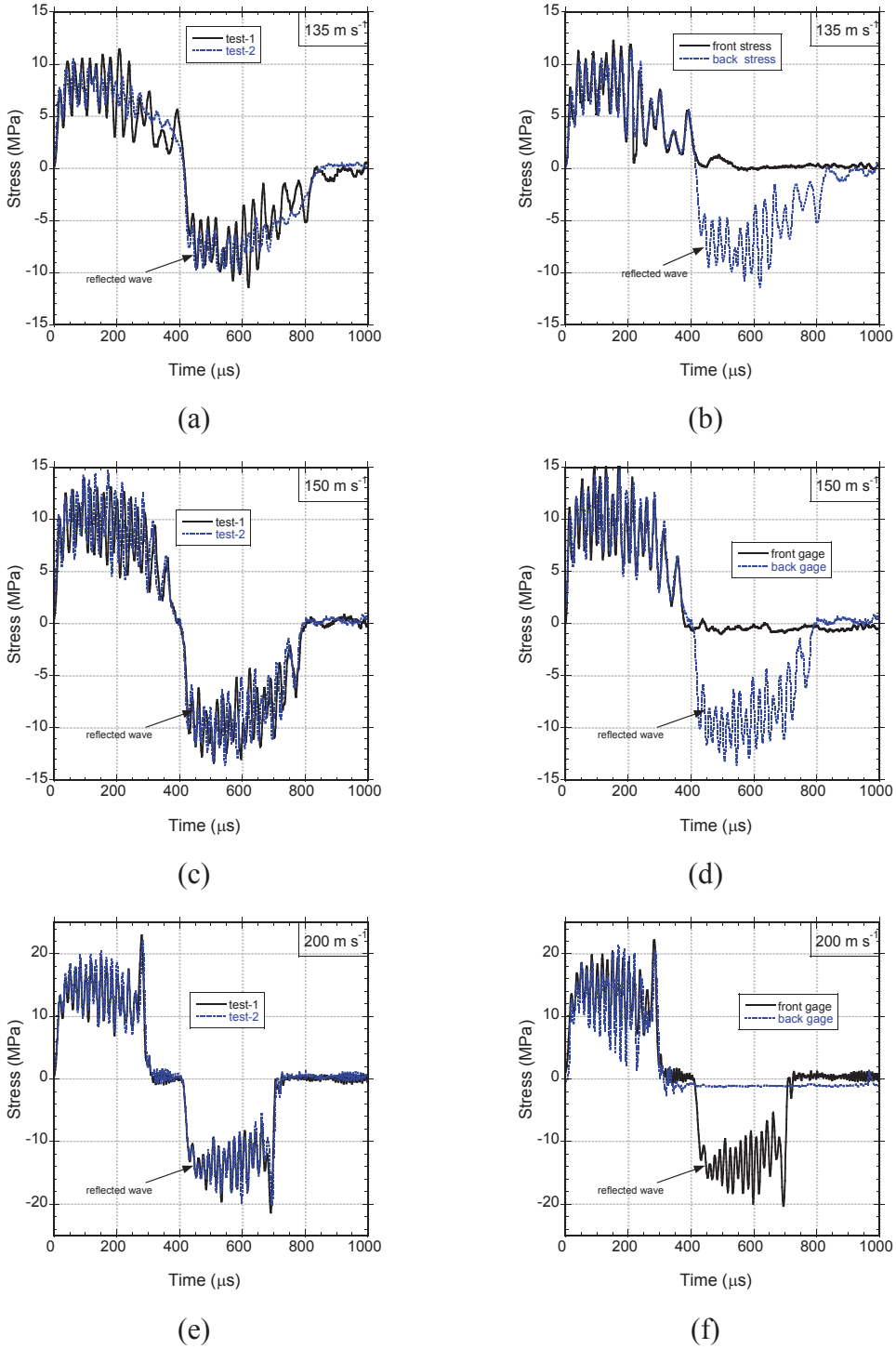


Figure 5.20. The stress-time profiles at 135 m $s^{-1}$ (a) two tests from back gages and (b) single test from front and back gages; 150 m $s^{-1}$ (c) two tests from back gages and (d) single test from front and back gages; and 200 m $s^{-1}$ (e) two tests from back gages and (f) single test from front and back gages

Figures 5.21(a) and (b) show the stress-time profiles at 3 different velocities measured from the back and front gages, respectively. As noted in the same figures, as the velocity increases the stress values increases. The stress waves reflected from the free end of the incident bar are also presented in the same figures. Figure 5.22 shows the deformation high speed camera pictures of the corrugated sample at a time interval of 50 μs at 150 m $s^{-1}$. The crushing of the sample in this figure starts from the impacted end and proceeds in a planar manner to the distal end of the sample, showing a shock wave formation. Similar shock wave progression at the impact end was recorded, for the tests performed at 135 and 200 m $s^{-1}$

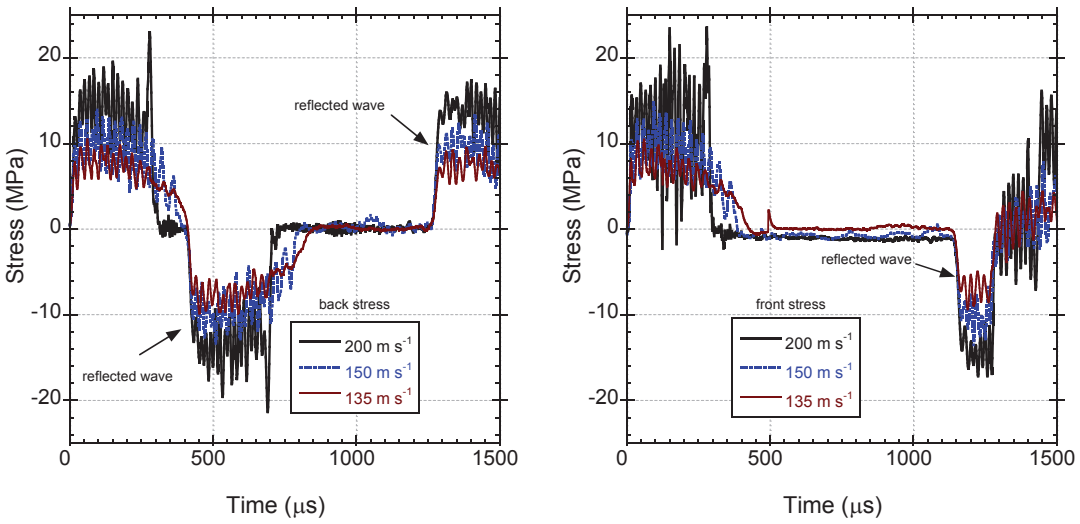


(a) (b)

Figure 5.21. The stress-time profiles of corrugated samples measured from (a) back and (b) front gages at different velocities

Figures 5.23 (a-d) show the stress-time profiles of the perfect model I, perfect model II, one layer imperfect model and two layer imperfect model at 135 m $s^{-1}$ together with the experimental stress-strain curve. In the same figures, the experimental and numerical sample's final deformed pictures are also shown for comparison. All models show higher initial crushing stress than the experiment (Figures 5.23(a-d)). The crushing stress of the models also approach to each other at this velocity, while perfect model II best approximates the duration of the experimental deformation. The deformation sequences of four numerical models at 135 m $s^{-1}$ are shown separately in Figures 5.24(a-d) for perfect model I, perfect model II, one layer imperfect model and two layer imperfect model, respectively. As is seen, the perfect model I results in one

and half undeformed layer (Figure 5.24(a)). The one layer imperfect model almost results in complete compaction of all layers (Figure 5.24(c)) and also large stress variations in the mid sections of stress-time profile. The two layer imperfect model results in one undeformed layer, the last layer (Figure 5.24(d)). The perfect model I also results in only one undeformed layer, the last layer, same as the experiment.

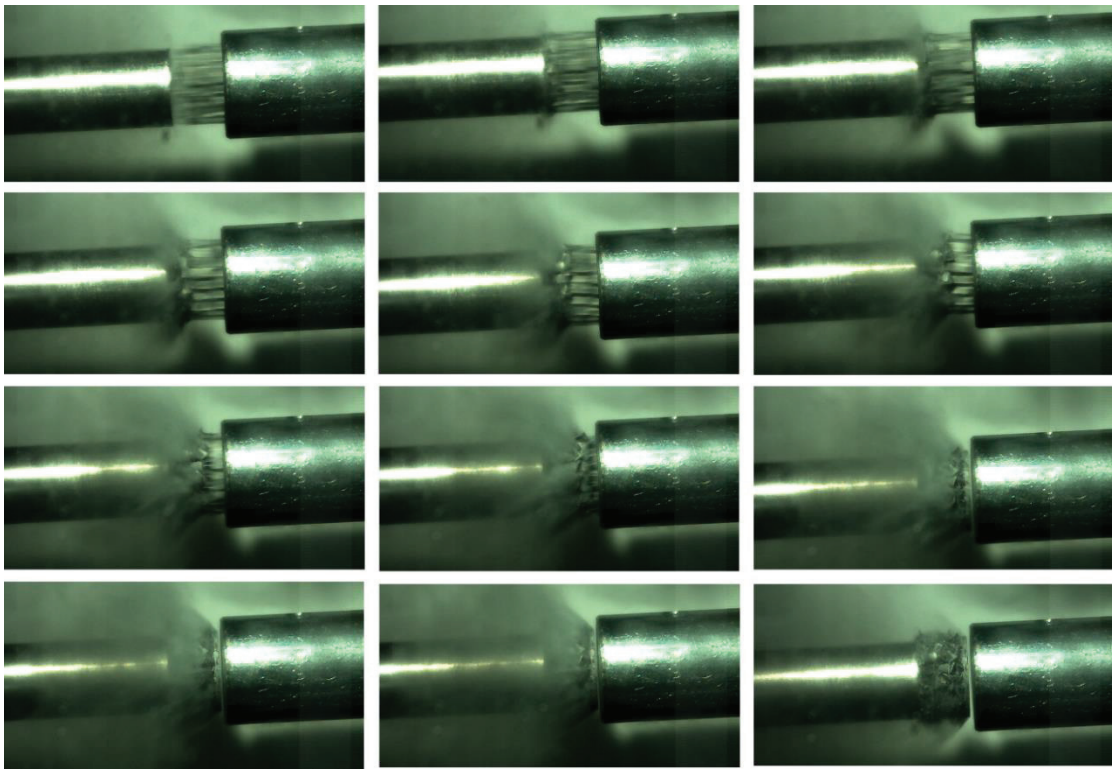

Figure 5.22. The deformation pictures of the corrugated sample tested at 150 m $s^{-1}$ showing shock deformation (time interval is 50 μs)

Figures 5.25(a) and (b) show the perfect model I and perfect model II stress-time profiles of 150 m $s^{-1}$, respectively. In the same figures, the experimental and numerical final deformed pictures are also shown for comparison. Experimentally, all layers are almost completely crushed at 150 m $s^{-1}$. The perfect model I results in one undeformed layer, while the perfect model two show almost complete layer crushing at the end of the deformation. Although at 200 m $s^{-1}$ both models result in complete layer crushing, the perfect model I cannot predict the final densified region in the stress-time profile shown in Figure 5.25(c), while the perfect model II predicts the increase in the stress values near the end of the deformation as seen in Figure 5.25(d). The experimental and numerical final thicknesses of the tests are listed in Table 5.2. It is seen in this table, the experimental final thicknesses of the test samples are nearly approached by the perfect model II.

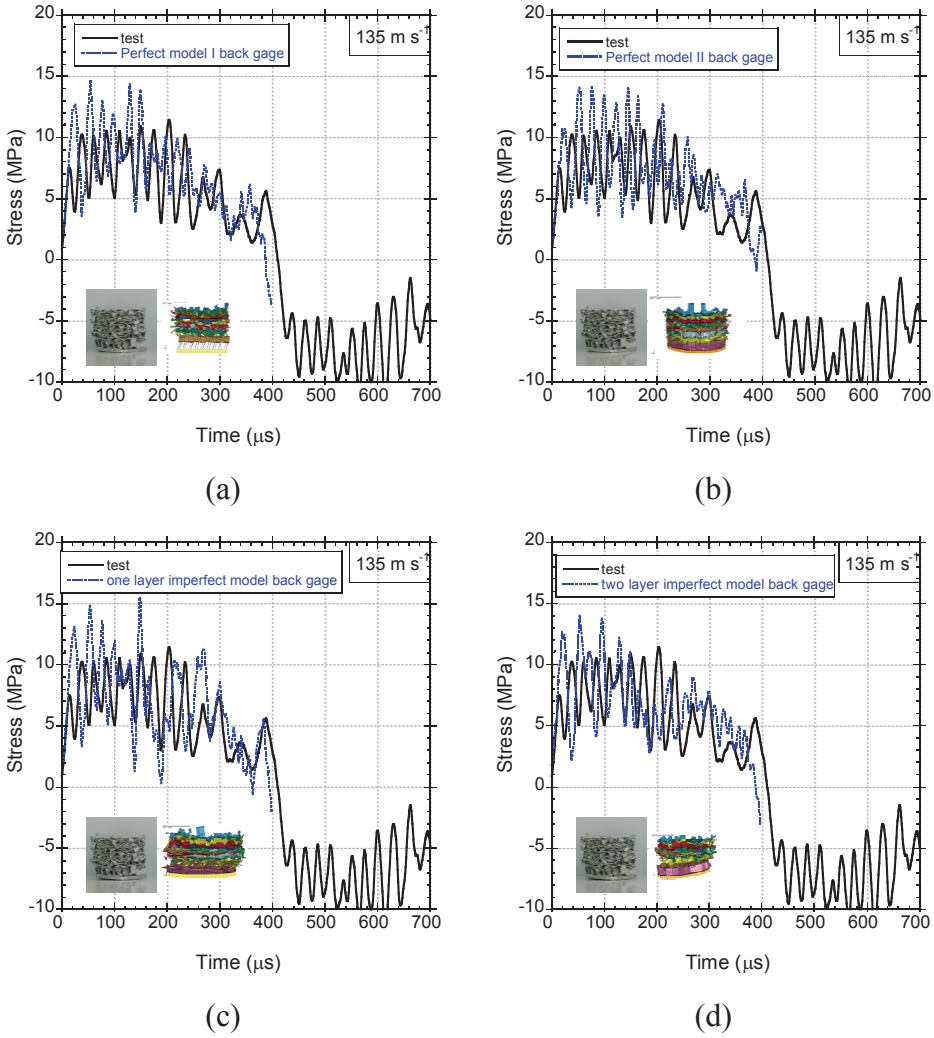


Figure 5.23. The stress vs time profiles corrugated samples tested at 135 m $s^{-1}$ (a) perfect model I and (b) perfect model II, (c) one layer imperfect model and (d) two layer imperfect model

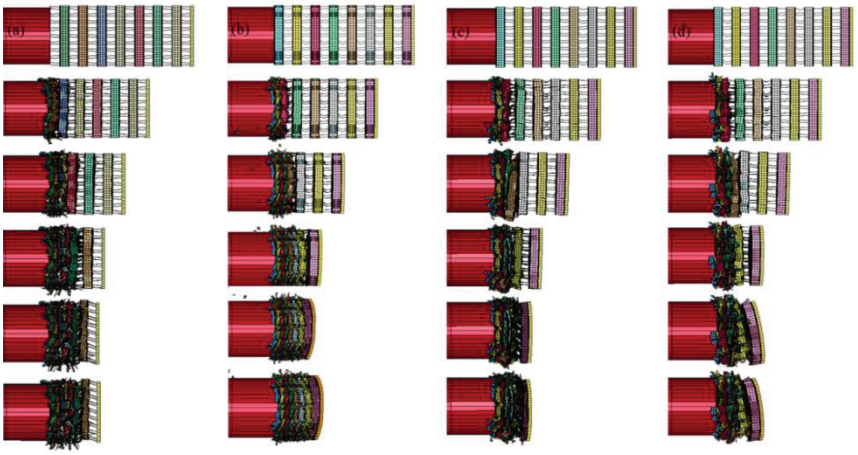

Figure 5.24. The deformed pictures of the corrugated sample at 135 m $s^{-1}$ (a) Perfect model I and (b) Perfect model II (c) one layer imperfect model and (d) two layer imperfect model (time interval is 100 μs)

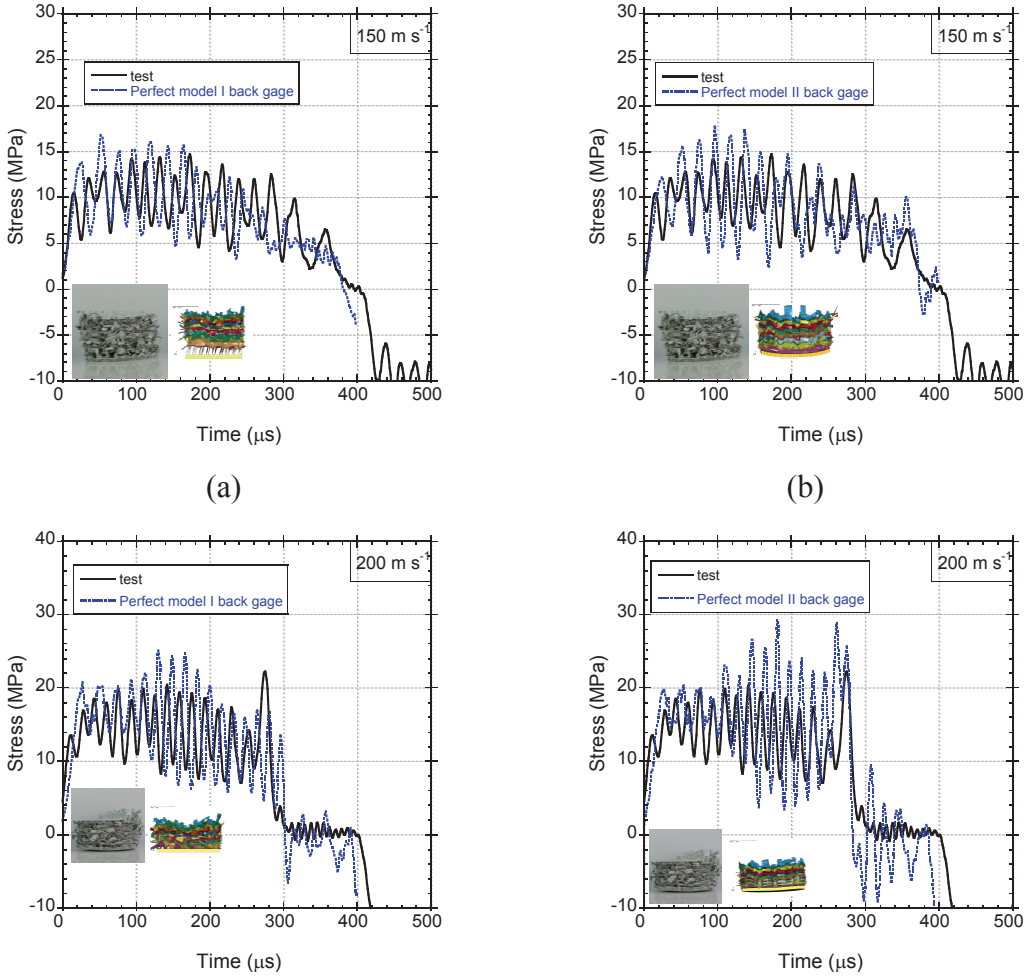


Figure 5.25. The stress vs time profiles corrugated samples tested at 135 m $s^{-1}$ (a) perfect model I and (b) perfect model II and at 200 m $s^{-1}$ (c) perfect model I and (d) perfect model II

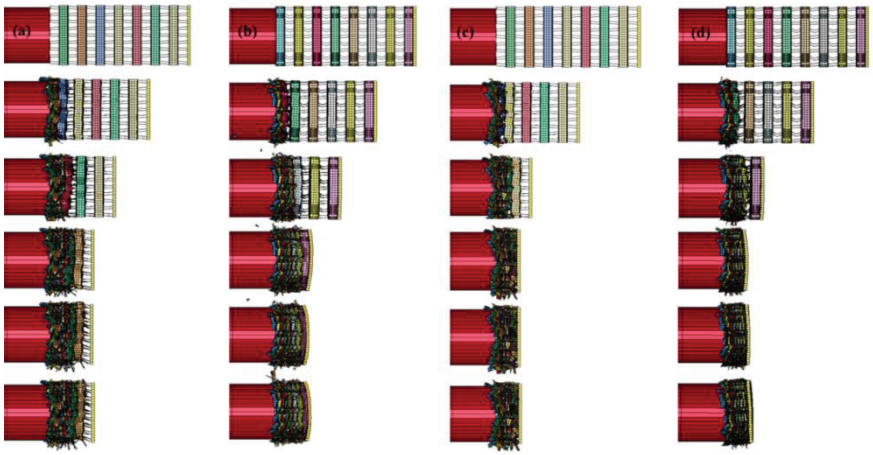


Figure 5.26. The deformed pictures of the corrugated sample at 150 m $s^{-1}$ (a) Perfect model I and (b) Perfect model II and at 200 m $s^{-1}$ (c) Perfect model I and (d) Perfect model II (time interval is 100 μs)

Table 5.2. The experimental and numerical final thickness of the tested corrugated sample at different velocities

| Velocity | 135 m $s^{-1}$ | 150 m $s^{-1}$ | 200 m $s^{-1}$ |
|---|---|---|---|
| Experimental thickness (mm) | 14.78 | 11.16 | 8.97 |
| Perfect model I thickness (mm) | 16.20 | 14.9 | 9.0 |
| Perfect model II thickness (mm) | 13.7 | 11.5 | 8.8 |

# CHAPTER 6

# DISCUSSION

## 6.1. The Effect of Velocity on Crushing Behavior

All quasi-static models exhibit higher initial peak stresses and densification strains, but lower valley and mean stresses than tests (Figures 5.2(a-d)). The highest initial peak and mean stress are found in the perfect model I as it has geometrically the strongest structure. The insertion of imperfect layer(s) tends to decrease both initial peak and mean stress at the quasi-static velocity. Similar results of the reduced initial peak and post stress values with the insertion of imperfections were reported previously in testing metallic pyramidal truss and Nomex honeycomb core at quasi-static velocities [5, 32].

The quasi-static layer strains and nominal strain and stress histories of the two layer imperfect model and perfect model II, representing perfect and imperfect models, are shown sequentially in Figures 5.2(a) and (b). The specimen's top layer at which the cross-head compresses the specimen is numbered layer 1 and the bottom layer 15. The differences in the layer deformation behavior between the imperfect and perfect models are clearly seen in these graphs and the deformation sequence pictures shown in Figure 5.3. The localized deformation in imperfect model starts earlier from one of the imperfect layers: in two layer imperfect model the crushing starts from layer 10 and/or layer 9 as seen in Figure 6.1(a) and Figure 5.3(e). So-called two-stage layer crushing is also seen Figure 6.1(a). Initially layers are compressed until about 0.4 strain, then these crushed layers are further compressed until about the densification strain gradually. The layers crushing later stages of the deformation are directly compressed to near or above the densification strain. The concurrent crushing of two or more layers, which was also observed in the experiments, is clearly seen in Figure 6.1(a). Initially all layers deform elastically and plastically in the perfect model II (see arrow in Figure 6.1(b)) until the strain localization occurs, likely due to the misalignments of the layers near the top and bottom of the specimen (Figure 5.3(c)). The initial crushing layers in perfect model II are localized at and near the specimen's ends, layer 14, 3, 2 and 15. The layers crush

individually and more or less sequentially/gradually starting both from the top and bottom layers until about or slightly below the densification strain. The two-stage layer compression is also seen in the perfect models but only for few layers, while it is a dominant deformation mode in the imperfect models. As shown by arrows in Figures 6.1(a) and (b), both imperfect and perfect models show increased stress values after 0.76 strain, while the individual layer's strains show great variability between each other at this nominal strain value. Since the layer crushing in quasi-static experiments starts from the mid-sections as seen in (Figure 5.3(a)), the quasi-static crushing response of test specimens are best represented by the imperfect models.

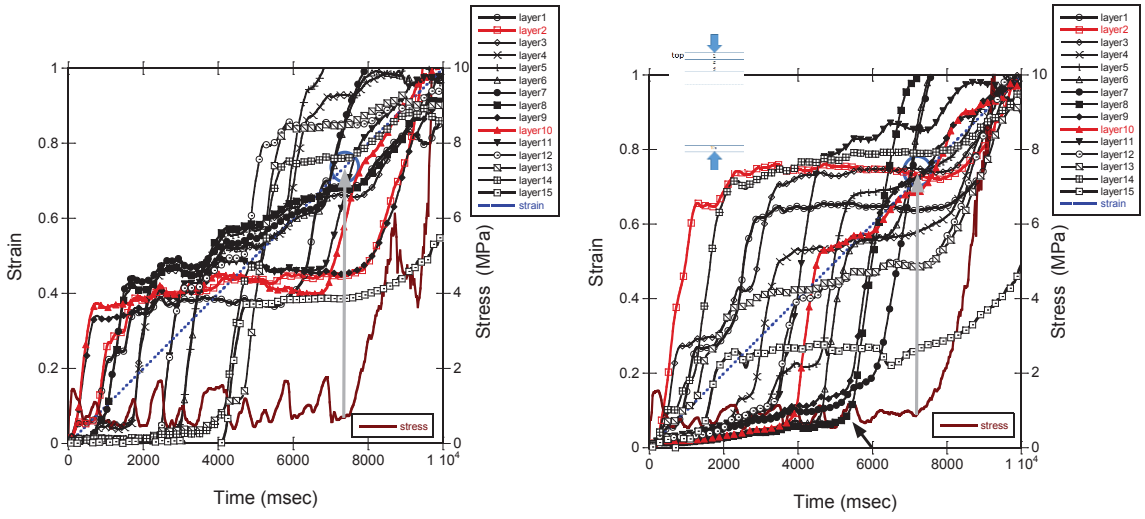


(a) (b)

Figure 6.1. Layer strain-time, strain-time and stress-time graphs of (a) two layer imperfect model and (b) perfect model II

In order to determine whether the quasi-static compression properties of the tested structure are size dependent, the test specimens in 40 mm diameter having the same height with 19.40 mm diameter specimens were compression tested quasi-statically at 0.0048 m $s^{-1}$. The representative quasi-static velocity stress-strain curves of 40 mm and 19.40 mm diameter specimens are shown together in Figure 6.2(a). Increasing specimen diameter as seen in the same graphs increases both the initial peak (from 1.25 MPa to 1.5 MPa) and the post-peak stress values without significantly affecting the valley stress values. At both diameters, the specimens show increasing post-peak and valley stresses as the strain increases, shown by the dotted lines in Figure 6.2(a). This is likely due to the bending of the specimen during the course of deformation, resulted from the constraint of the compression test platens to the lateral

motion of specimen's ends. In order to assess the effect of friction, 40 mm diameter samples were tested with a thick layer of lubricant (grease) deposited on the both bottom and top compression test platen's surfaces. The surfaces of the platens were completely lubricated in way that the test specimen ends freely moved in lateral direction as the individual layers were compressed progressively. This provided a near-axial loading of the specimen without inducing lateral constraint to the specimen. With the use of excessive lubricant, the layers were observed to crush in a progressive mode (individual layers were crushed progressively but not necessarily sequentially). Figure 5.2(b) shows the stress-strain curves of a 40 mm diameter specimen tested using excessive lubricant together with that 19.40 mm diameter specimen. In the stress-strain curve of the specimen tested with excessive lubrication, each stress peak following the initial stress peak corresponds to the completion of the crushing of individual layers. As seen in the same figure, total 13 layers crush in the test before the densification and the last two layers collapse in the densification region when all-crushed layers are compressed together. This observation was further confirmed by the camera records. Without end-constraint, the peak and valley stresses become almost equal to each other during the course of the deformation till densification as shown by the dotted lines in Figure 6.2(b). The average initial peak stress without end-constraint is 1.35 MPa and the mean stress is 0.96 MPa. The mean stress is found to be similar to that of 19.40 mm diameter sample, 0.96 MPa, as tabulated in Table 5.1. As the compression of the last two layers occurs in the densification region, a densification strain is calculated before the densification until about the completion of 9 layers as shown by an arrow in Figure 6.2(b). The nominal strain at the completion of 9-layer crushing is 0.43, resulting a displacement of 20.7 mm and per layer displacement of 2.3 mm. The division of layer displacement with the height of the layer, 3.2 mm, gives an average densification strain of 0.72. This value of densification strain is lower than the numerical densification strain, 0.76, while it is higher than the experimentally determined densification strain, 0.67. The differences in the crushing stress and densification strain between the test and numerical models at quasi-static velocity are simply attributed to the presence of imperfections in the test specimen. Note that the filler material used in the brazing process is excluded in the model. The filler naturally increases the thickness of the fin sheet at the bottom and top shown by arrows in Figure 6.3(a). This may end up with an increased plateau stress and a reduced densification strain in the test specimen. The test specimens of tested corrugated structure actually contained 7wt% filler material and the

effect of filler material on the crushing will be investigated in another study. The machining as stated earlier induces damages/imperfections on the specimen's outer surfaces as depicted in Figure 6.3(b). While, as opposed to this, the imperfections are included as a specific layer or layers in the models. Also, note that the effect of machining induced surface imperfections on the stress is expected to be less in larger size specimens than in small size specimens due to lower surface area to volume ratio in larger size specimens. The higher initial peak and post-peak stress values in 40 mm diameter specimen are attributed to the reduced surface area to volume ratio.

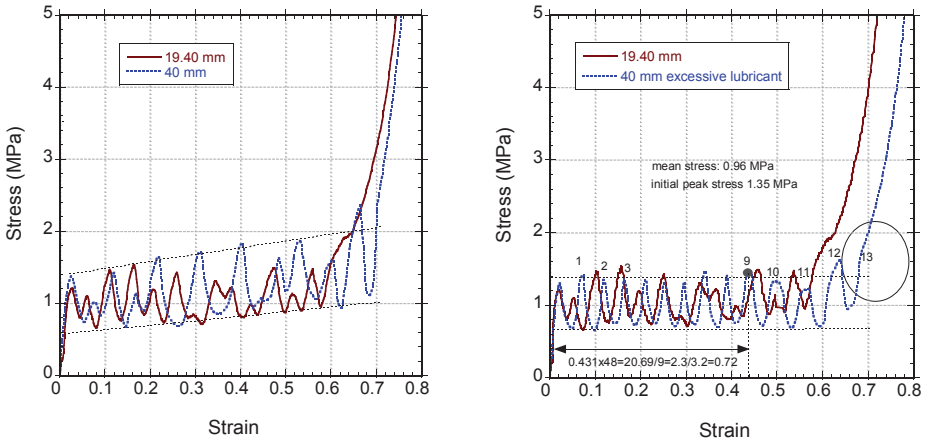


(a) (b)

Figure 6.2. Layer strain-time, strain-time and stress-time graphs of (a) perfect model II and (b) two layer imperfect model

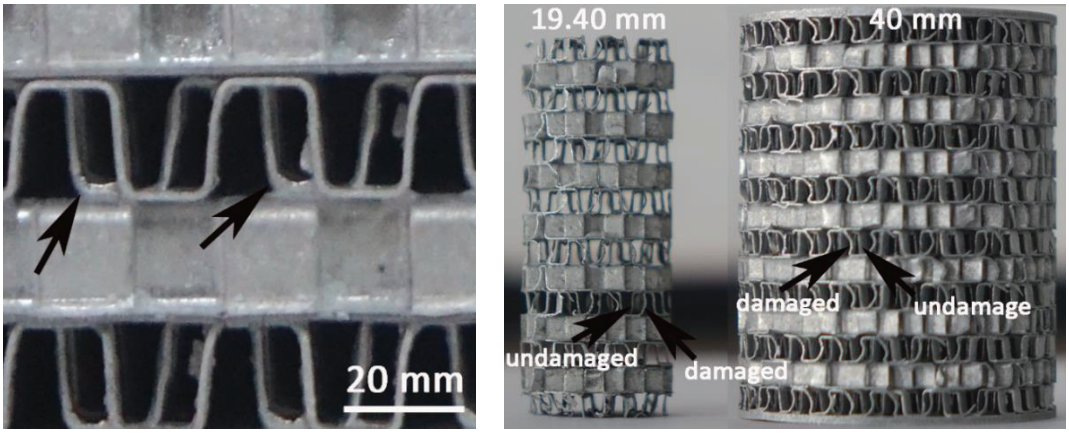


(a) (b)

Figure 6.3. (a) the side view picture of corrugate plate shown increased thickness at the brazing sections and (b) the pictures of 19.40 and 40 mm test specimens showing machining induced imperfection on the surface

## 6.2. Dynamic tests and models

The experimental and numerical deformation sequences of the SHPB, direct impact and Taylor impact tested specimens at different velocities were given in detail in Chapter 5. Based on these records of the deformation sequences, the tested corrugated structure is considered to exhibit three distinct, sequential deformation modes, both experimentally and numerically, at increasing velocities, as will be elaborated below.

At relatively low velocities, between 0.0048 m $s^{-1}$ and 22 m $s^{-1}$, the crush bands (localized deformation) form randomly. At this velocity range, the layer crushing starts most likely from the weakest fin layer and progresses non-sequentially to the uncrushed layers/parts. Above deformation mode is seen at quasi-static velocity tests (Figure 5.3), in the SHPB tests at 6 and 10 m $s^{-1}$ (Figure 5.7) and in the direct impact tests at 9 m $s^{-1}$ (Figure 5.9). The numerically calculated stresses at the impact and distal ends are almost the same and in equilibrium (Figure 5.8). This deformation mode is therefore referred as to "quasi-static homogenous mode" [57]. Similar homogenous deformation modes were previously identified in regular and irregular honeycomb structures as X-shape shear bands [2], in Voronoi honeycombs [3], and in corrugated layered Al structure [11]. In the homogenous deformation mode as the layer crushing localizes in the mid-sections of the cylindrical test sample, the specimen bends during a test (Figure 5.3(a)). The bending causes a non-axial loading of the specimen. Although specimen bending does not significantly affects the initial peak stress, it increases the peak stresses as the strain increases as explained before in this chapter. Similar specimen bending is also observed in the models. The deformation mode between 22 and 60 m $s^{-1}$ is considered as the "transition mode" as the layer crushing is more concentrated at the impact end than at the distal end (Figures 5.12, 5.14 and 5.17). The strain distribution in the crush band is wider or diffusive rather than confined in a narrow region. The strain in the crushed layers does not reach the densification strain [57]. At high velocities, at and above 90 m $s^{-1}$, a shock mode occurs. In this mode, the sample crushes sequentially layer by layer starting from the impact end (Figures 5.19 and 5.22). The crushed layer strain in this mode reaches the densification strain.

Alternative to the above analysis based on the camera records, the deformation modes are also investigated numerically by determining the layer strain histories of direct and Taylor impact test models. Figures 6.4(a-d) show the layer strain, nominal strain, velocity and stress-time profiles of the two layer imperfect model at 22, 40, 60

and 90 m $s^{-1}$, respectively. Although at the quasi-static velocity, the crushing starts from layer 10 and/or layer 9 (Figure 6.1(b)), the imperfect layer 2 near the impact end crushes simultaneously with layer 1, while the imperfect layer 10 crushes afterwards seen in Figure 6.4(a) at 22 m $s^{-1}$. This shows the effect of inertia starting as early as 22 m $s^{-1}$ without significantly altering the deformation mode. However, as the velocity increases to 40 and 60 m $s^{-1}$, the impact end layer 1 crushes before the imperfect layer 2 as seen in Figures 6.4(b) and (c). As compared with quasi-static layer strain profiles also seen in Figure 6.1(a), at these velocities, more and more layers collapse until the densification strain sharply rather than collapsing gradually until the densification strain. A near sequential layer crushing is found at 90 m $s^{-1}$ as seen in Figure 6.4(d), except the imperfect layer 10 and layers near it crushes non-sequentially. As opposite, the layer crushing in the perfect model II becomes almost sequential at 60 m $s^{-1}$, Figure 6.5(c), and completely sequential at 90 m $s^{-1}$, Figure 6.5(d). This is well accord with the experimental observation; the sequential crushing starts nearly at 90 m $s^{-1}$ (Figure 5.19). A layer densification strain is determined by measuring peak strain values of the first three crushed layers. As shown in Figures 6.5(c) and (d), the densification strains for the perfect model II are 0.67 and 0.72 at 60 and 90 m $s^{-1}$ respectively.

At 135 and 150 m $s^{-1}$ velocity, the layer crushing becomes sequential in the two layer imperfect model, except layer 10 and layer 9 crush together until strains higher than the densification strains (Figures 6.6(a-b)). But, the layer crushing becomes perfectly sequential at 200 m $s^{-1}$ in the two layer imperfect model (Figures 6.6(c)) and at all velocities in the perfect model II (Figures 6.7(a-c)). As seen in Figures 6.6(a-c) and Figures 6.7(a-c), the final deformed shapes of both models are similar except in two layer impact model the sides of deformed sample is not planar at 135 and 150 m $s^{-1}$. Both models however end up with the same densification strains (as written in the figures and determined from crushed first 3 layers since the velocity decreases with time). The numerical densification strains are 0.81 at 135 m $s^{-1}$ (Figures 6.6(a) and 6.7(a)), 0.84 at 150 m $s^{-1}$ (Figures 6.6(b) and 6.7(b)) and 0.88 at 200 m $s^{-1}$ shown in Figure 6.6(c) and Figure 6.7(c). The numerical densification strain increases with increasing impact velocity from 0.72 at 90 m $s^{-1}$ to 0.88 at 200 m $s^{-1}$. It is noted in the same graphs, the layer peak strains decrease as the time increases. This is due to the reduced velocity of the crushing corrugated sample with time. Although, imperfect and perfect models exhibit the same densification strain, the perfect model II results in higher final deformation strains than the two layer imperfect model.

Sequentially, the final strains are 0.73, 0.76 and 0.85 for the two layer impact model and 0.75, 0.79 and 0.88 for the perfect model II at 135, 150 and 200 m $s^{-1}$, respectively. Since the perfect model II is a geometrically soft model caused by the bent walls, it naturally deforms until about larger strains.

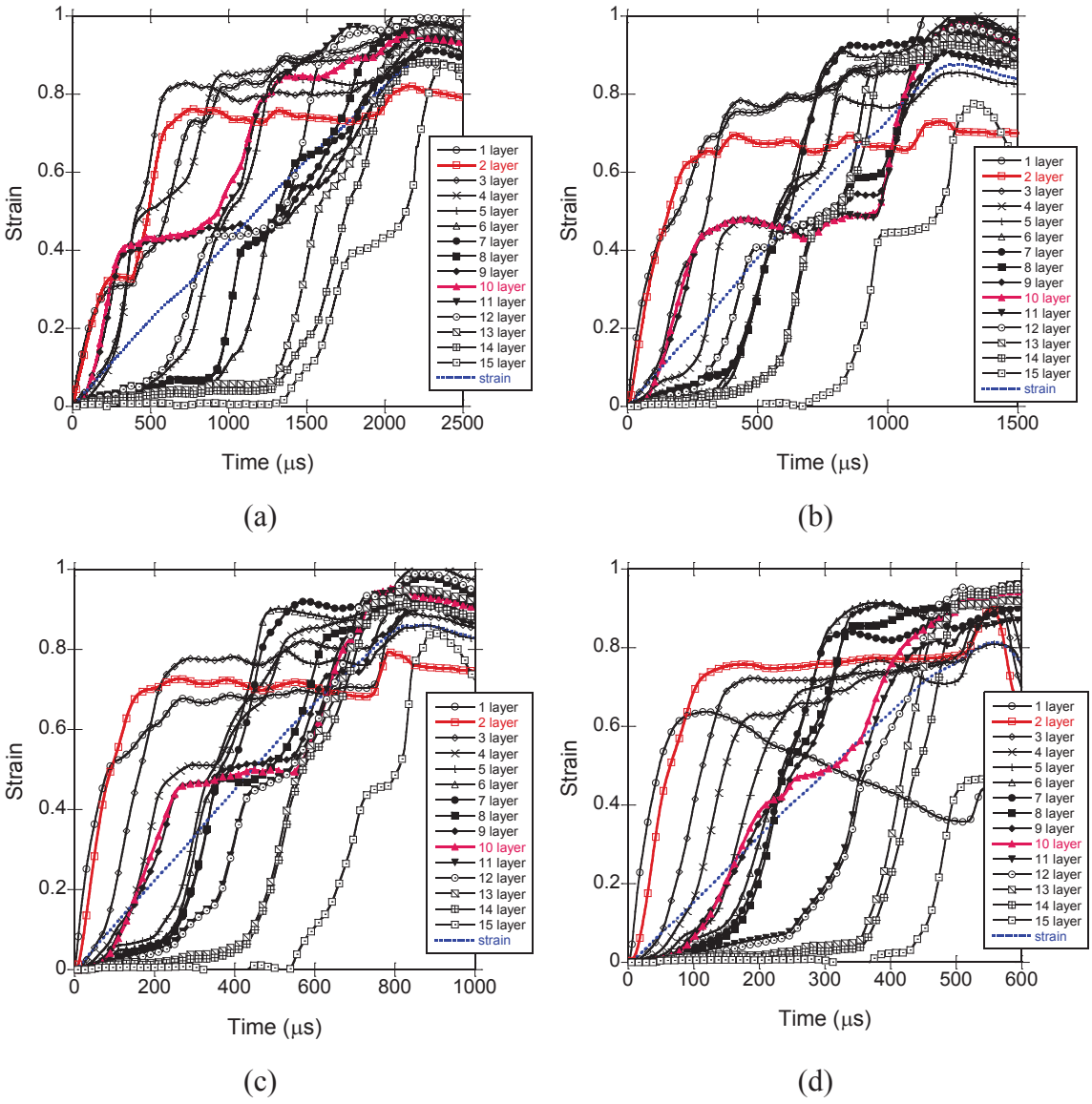


Figure 6.4. Layer strain-time, strain-time and stress-time graphs of two layer imperfect model at (a) 22, (b) 40, (c) 60 and (d) 90 m $s^{-1}$

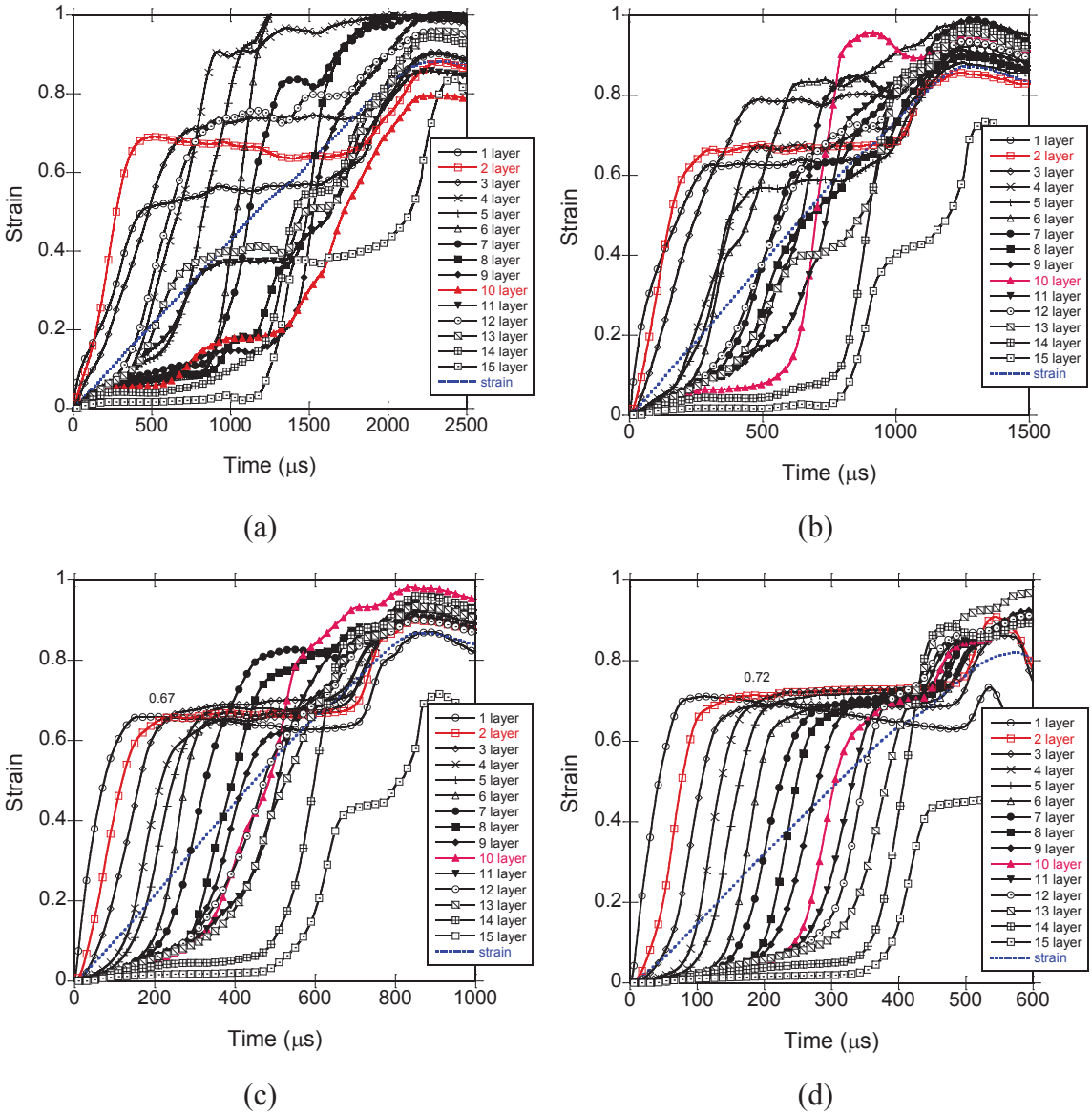


Figure 6.5. Layer strain-time, strain-time and stress-time graphs of perfect model II at (a) 22, (b) 40, (c) 60 and (d) 90 m $s^{-1}$

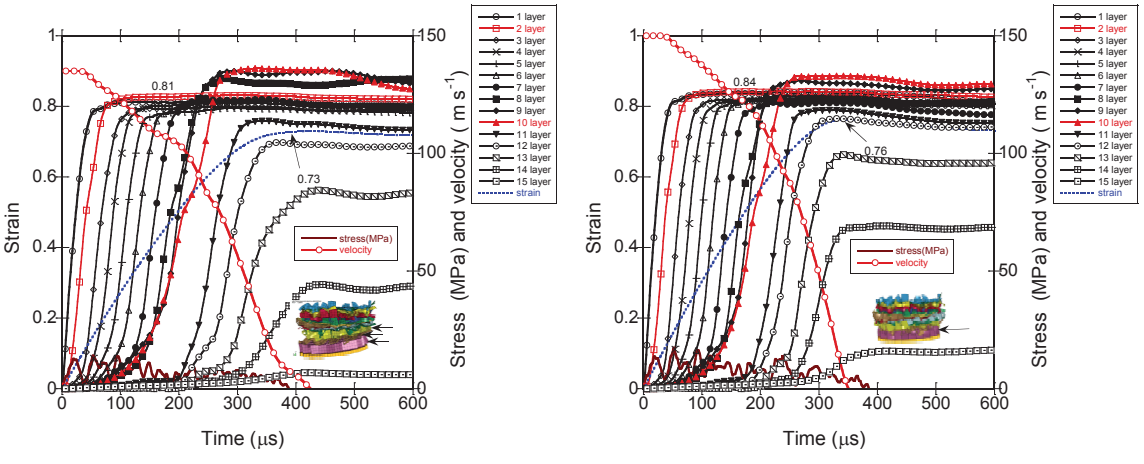

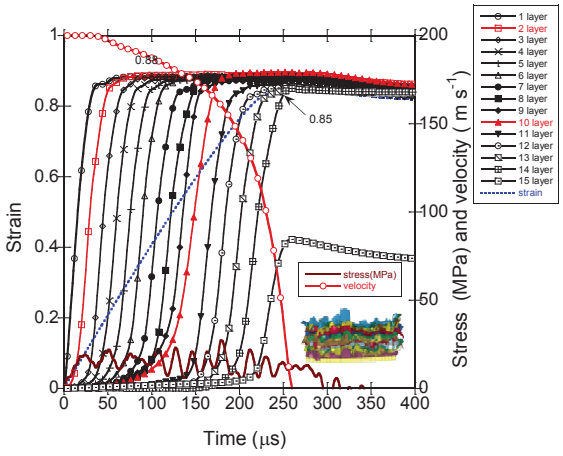


(c)

Figure 6.6. Layer strain-time, strain-time and stress-time graphs of two layer imperfect model at (a) 135, (b) 150 and (c) 200 m $s^{-1}$ (cont.)

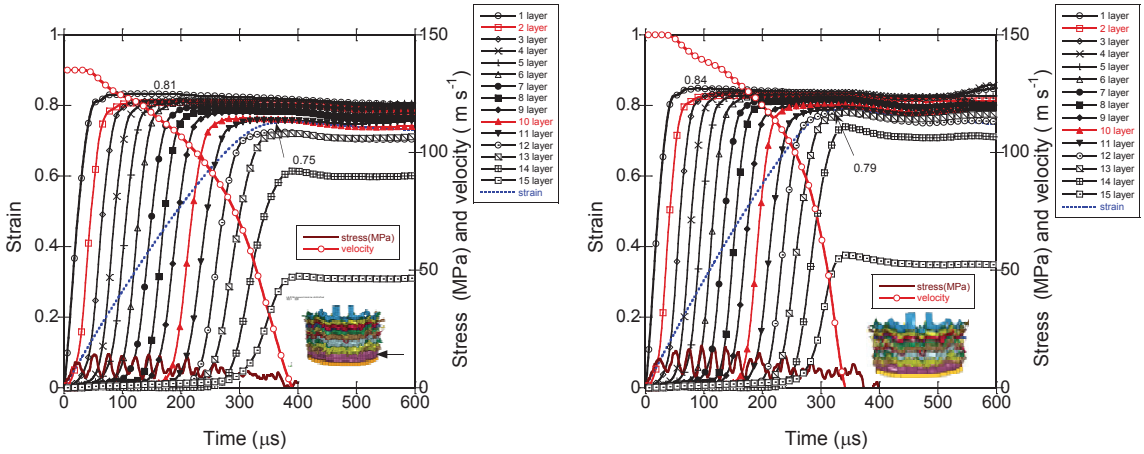


(a) (b)

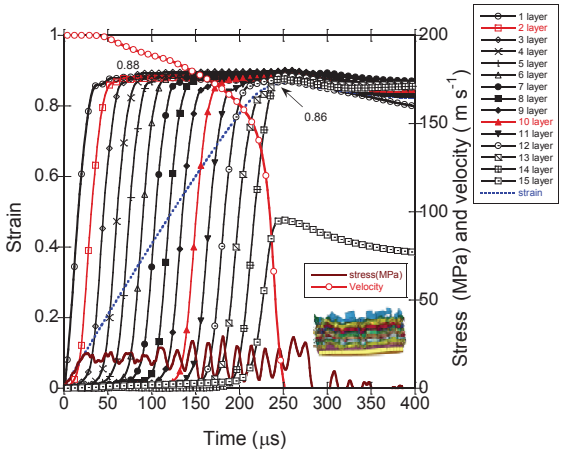


(c)

Figure 6.7. Layer strain-time, strain-time and stress-time graphs of perfect model II at (a) 135, (b) 150 and (c) 200 m $s^{-1}$

## 6.3. Critical Velocity for Shock

The following equation was proposed to calculate the critical velocity for the shock formation by considering all the internal energy was due to the loss of the kinetic energy [12]

$$v_{cr} = \sqrt{\frac{2\sigma_p \varepsilon_d}{\rho_o}} \tag{6.1}$$

Taking $\sigma_p$ as the mean stress, 0.96 MPa, $\rho_o$ =326 kg m$^{-3}$ and $\varepsilon_d = 0.72$, the critical velocity is calculated ~65 m s$^{-1}$. When $\sigma_p$ is taken as 0.84 MPa for the perfect model II, the critical velocity approaches 60 m s$^{-1}$. These velocities are well accord with the experimentally and numerically determined critical velocities for shock formation. Experimentally, it is seen a complete sequential crushing at 90 m s$^{-1}$ and the perfect model II results in near sequential and complete sequential crushing at 60 and 90 m s$^{-1}$, respectively.

## 6.4. The Effect of Imperfect Layer on the Shock Stresses

The effect of the insertion of imperfect layer at the quasi-static velocity is seen in Figures 5.2(a, c and d) and in Table 5.1. The imperfect layers change the location of initial crushing layer. As tabulated in Table 5.1, the initial layer crushing starts from layer 9 in the perfect model I, while it switches to imperfect layer 10 in the one and two layer imperfect model. The imperfect layers; however, do not affect the densification strain. Since the crushing initiates from the imperfect layer, the initial peak stress decreases in the imperfect models. The mean crushing stress also declines with the insertion of the imperfect layer since the imperfect layers also alters the stress distribution on the neighboring layers. It is noted in Table 5.1 that the perfect model II and the two layer imperfect model result in similar initial crushing stress (1.52 and 1.48 MPa) and mean stress (0.83 and 0.84 MPa). The perfect model II can also be considered as the full imperfect model. This implies that the stress of the imperfect model approaches to the perfect model II (full imperfect layer model) after inserting two imperfect layers. The similar effect is also seen in the SHPB test models. For example at 6 m s$^{-1}$, the perfect model I gives an initial peak stress of 2.35 MPa, the one layer

imperfect model 1.80 MPa and the two layer imperfect model 1.66 MPa. Again, the perfect model II and two layer imperfect model result in similar crushing stress, 1.66 and 1.67 MPa.

In the transition regime between 22 and 60 m $s^{-1}$, the effect of imperfect layer is shown in Figure 5.17. In this figure, the layer crushing sequences of four models are shown at various deformation times. For the perfect model I and the imperfect models; although, the deformation initially localizes near the impact end till 200 μs and although the layer crushing is still localized near the impact end in the perfect model I at 300 μs, the layer crushing in the imperfect models at 300 μs switches to homogeneous mode near the initially crushed impact end layers. Figures 6.8(a-d) show the striker bar-specimen and specimen-incident bar contact stress for the perfect model I, perfect model II, one layer imperfect model and two layer imperfect model, respectively. In the same graphs, the ratio of specimen-incident contact stress to the striker bar-specimen contact stress is also shown. When this ratio equals to 1, the deformation is considered to be homogenous. When, it is greater than 1, then the incident bar contact stress is greater than the striker bar contact stress and when it is less than 1, then vice versa. It is noted in Figures 6.8(a-d), as the ratio is less than 1 throughout the deformation before densification, the perfect model II clearly displays an inertia effect, while in the other models, the ratio fluctuates around 1. The deformation is therefore at this velocity somewhat in the transition stage for the perfect model I and imperfect models, while it switches to a shock mode in the perfect model II. When the velocity increases to 90 m $s^{-1}$ , all models show inertia effect and the stress ratio is less than 1 (Figure 5.18).

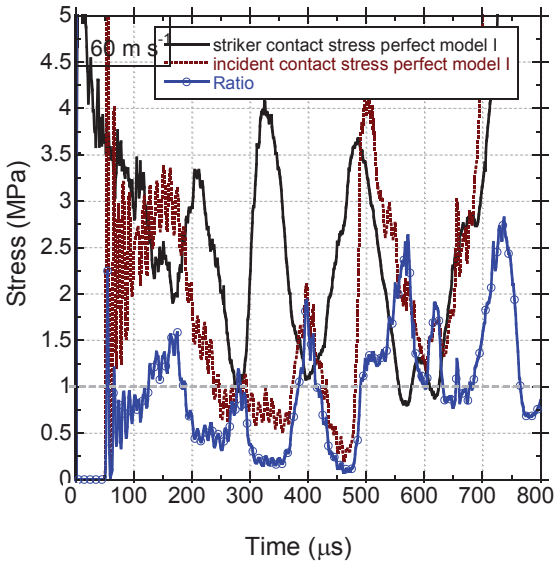


(a)

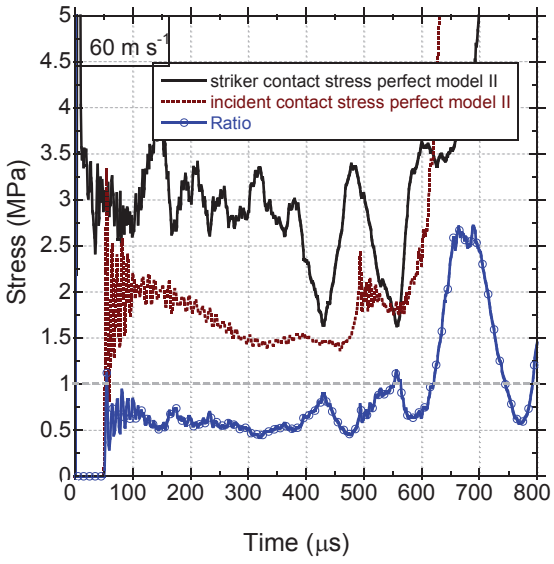


(b) **(cont. on next page)**

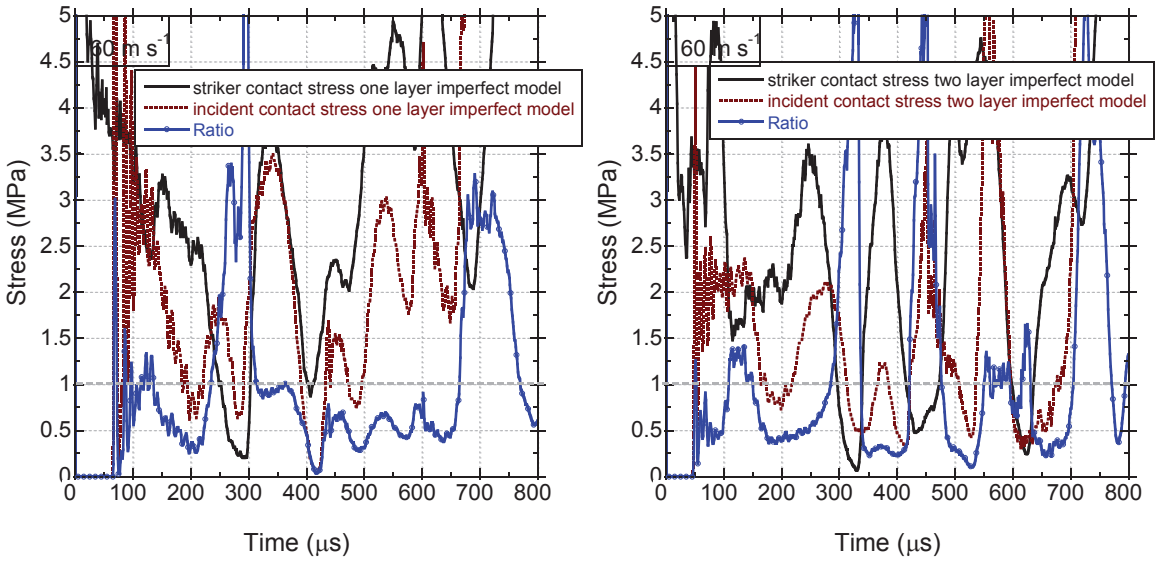


(c) (d)

Figure 6.8. Striker-sample and sample-incident bar contact stresses –time and incident bar striker bar constant stress ratio at 60 m $s^{-1}$ for (a) perfect model I, (b) perfect model II, (c) one layer imperfect model and (d) two layer imperfect model (cont.)

In the shock mode velocity range, the effect of imperfect layer on the shock stress is shown in Figure 6.9(a). The insertion of imperfect layer does not affect the initial peak stress until about the imperfect layer starts to crush. Note that the imperfect layer crushing is marked by the circles in Figure 6.9(a) for the one and two layer imperfect models. The circle A corresponds to layer 2 crushing and the circle B to the layer 10 crushing. As is seen in the same figure, in the event of the imperfect layer crushing, the stress in the imperfect models decreases as compared to the perfect model I. The effect of insertion fully imperfect layers, the perfect model II, is also shown in Figures 6.9(b), (c) and (d) at 135, 150 and 200 m $s^{-1}$, respectively. The perfect model I shows higher initial peak stress and valley stress than the perfect model II at 135 and 150 m $s^{-1}$, but the effect disappears when the velocity increases and both models show the similar initial peak stresses at 200 m $s^{-1}$ (Figure 6.9(d)). It is also noted that the perfect model II shows a densification region of the sharp stress rise near the end of the deformation. This is the indication of the crushing of all layers sequentially and finally these crushed layers are compressed together in the densification region. As stated in Chapter 2, when the backing mass equals to 0, the critical velocity for the densification is infinity. Since the test samples in the present study were fired with a thin face sheet layer at the back (1 mm) to the incident bar, the critical velocity for the densification

was calculated using Equation 2.17, with the following material parameters: $\sigma_p$=0.96 and 2 MPa and $\varepsilon_d$=0.88 and 0.77. The critical velocity is found between 100 m $s^{-1}$ and 165 m $s^{-1}$. The absence of a densification region at the end of the deformation at 135 and 150 m $s^{-1}$ is simply due to the reduction of the velocity of the impacted specimen as it consumes its kinetic energy. While at 200 m $s^{-1}$, the velocity of the specimen is sufficient for all layers completely crushed and for the densification.

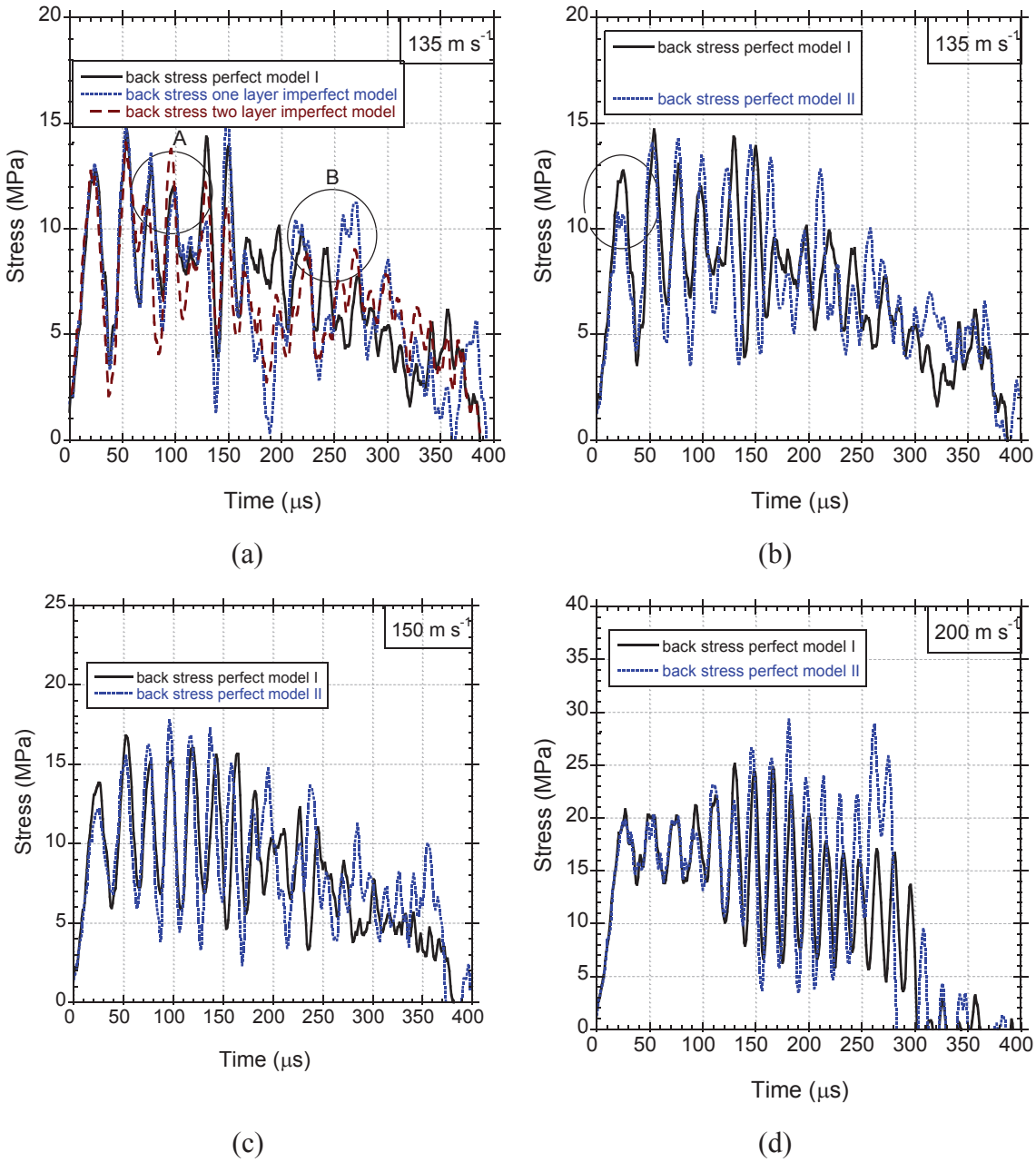


Figure 6.9. Stress-time curves (a) Perfect model I and imperfect models and (b) Perfect model I and II at 135 m $s^{-1}$ and stress time curves of perfect model I and II at (c) 150 m $s^{-1}$ and (d) 200 m $s^{-1}$

## 6.5. The Effect of Velocity on the Crushing Stress and R-P-P-L Model Prediction

Figure 6.10(a) shows the experimental distal end stress-strain curves of quasi-static and direct impact tests until 90 m $s^{-1}$. As seen in the same figure, the initial peak stress increases as the velocity increases. This is a clear indication of the micro-inertia effect and the tested corrugated structure shows a Type II behavior [65, 71]. The variations of experimental and perfect model distal end peak stress with velocity and the perfect model's densification strain with velocity are shown in Figure 6.10(b). For the model and experiments, the distal end stress increases until about 60 m $s^{-1}$ from 1.35 MPa at quasi-static velocity to 2 MPa at 60 m $s^{-1}$ , then it saturates at 2.15 MPa experimentally and ~2 MPa numerically. Figures 6.10(c) and (d) show the perfect model II contact stresses of striker-specimen and specimen-incident bar interface at 60 and 90 m $s^{-1}$, respectively. At both velocities, the specimen-bar contact stress is about 2 MPa and as time passes it decreases to a plateau stress of 1.5 MPa and 1.8 MPa for 60 and 90 m $s^{-1}$, respectively. The densification strain in Figure 6.10(b) is fitted with a power-law relation

$$\varepsilon_d = 0.25 * {v_o}^{0.24} \tag{6.2}$$

In Figures 6.10(c) and (d), the r-p-p-l predicted stress-time profiles using Equation 2.16 and quasi-static plateau stress (0.96 MPa) and densification strain (0.72) are also shown for 60 and 90 m $s^{-1}$, respectively. Using the quasi-static plateau stress, the r-p-p-l model predicts lower crushing stress at both velocities than the perfect model II as depicted in Figures 6.10(c) and (d). On the other side, the use of dynamic plateau stress of 1.65 and 1.8 MPa at 60 and 90 m $s^{-1}$ results in r-p-p-l model stresses which are very similar with those of the perfect model II. The r-p-p-l model based on the dynamic plateau stress also gives very similar velocity-time profiles with the model as seen in Figure 6.10(d).

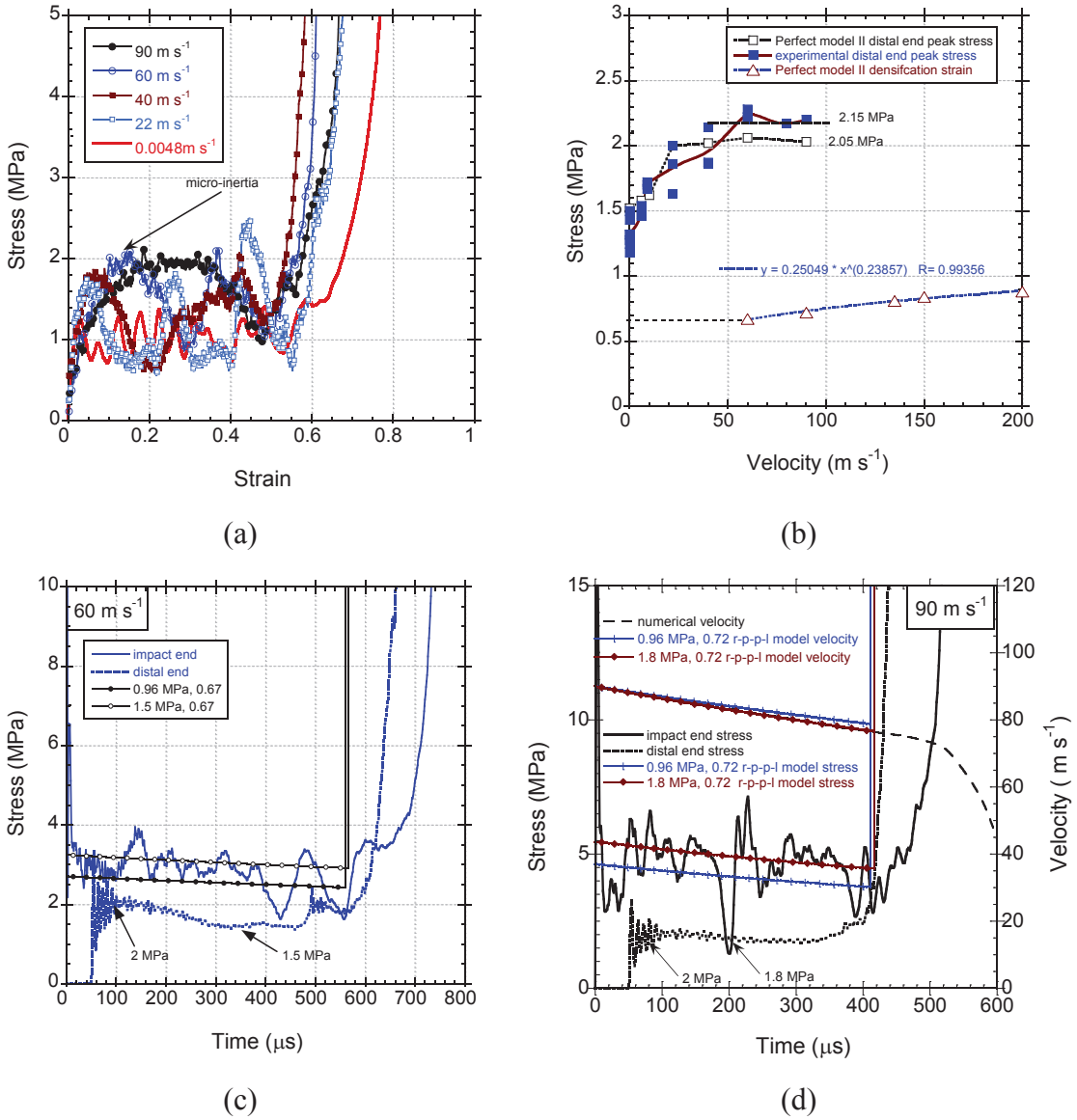


Figure 6.10. The experimental front gage stress-time histories of direct impact test, (b) the variation of perfect model II and experimental distal end peak stress with time and perfect model densification strain with time and (c) the r-p-p-l model fitting with quasi-static and varying parameters at 60 m $s^{-1}$

The dynamic plateau stresses, ${\sigma_p}^d$, at 135, 150 and 200 m $s^{-1}$ is determined ~2 MPa from above analysis. Inserting Equation 6.2 and dynamic crushing stress into Equation 2.10 gives the variation of r-p-p-l model stress with time in the Taylor impact tests as

$$\sigma^* = {\sigma_p}^d + \frac{\rho_o}{0.25 * {v_o}^{0.24}}\left[v_o^2 + \frac{2 * {\sigma_p}^d * 0.25{v_o}^{0.24}}{\rho_o} ln\left(1 - \frac{\rho_o * A_o * u}{M * 0.25 * {v_o}^{0.24}}\right)\right] \quad (6.3)$$

Figures 6.11(a), (b) and (c) show the r-p-p-l model stress–strain and velocity-strain profile prediction for 135, 150 and 200 m $s^{-1}$, respectively. In the same figures,

the r-p-p-l model stress–strain and velocity-strain prediction using quasi-static plateau stress and densification strain and quasi-static plateau stress and numerically determined densification strain at that specific velocity are also shown. The resultant curves are also compared with the perfect model II stress-time and velocity-time graphs in the same graphs. As seen in Figures 6.11(a) and (b), the use of quasi-static plateau stress and densification strain and the quasi-static plateau stress and numerical densification strain in the r-p-p-l model results in higher velocities than the perfect model at 135 and 150 m $s^{-1}$ and a full densification case (velocity is higher than zero). While, in the r-p-p-l model based Equation 6.3, the modified model, the velocity attains to zero at the end of the deformation at both 135 and 150 m $s^{-1}$, agreeing with the perfect model II and the experiments (Figures 5.23(b) and 5.25(b)). When the velocity increases to 200 m $s^{-1}$, all r-p-p-l model predictions result in full densification (velocity does not attain to zero). However, the modified r-p-p-l model shows a velocity-strain profile that perfectly matches with the perfect model II until about large strains. Furthermore, the r-p-p-l modified r-p-p-l model gives a stress-time profile which nearly predicts the reduction of the stress near end of the deformation as seen in Figures 6.11(a-c). Both, the perfect model and the r-p-p-l model exhibit the increase in crushing stress with the velocity and also increased densification strain as seen in Figure 6.11(d).

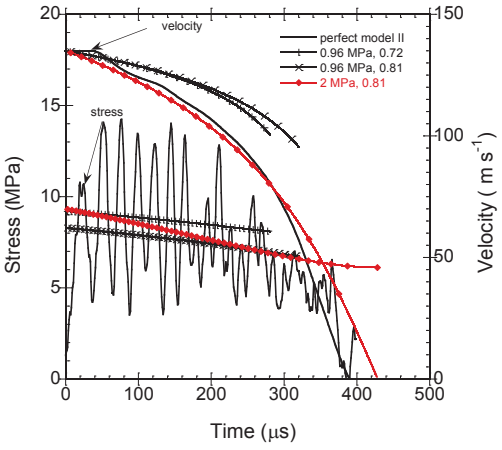


(a)

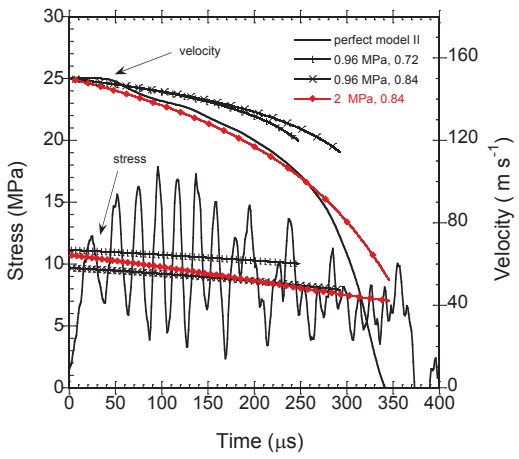


(b) **(cont. on next page)**

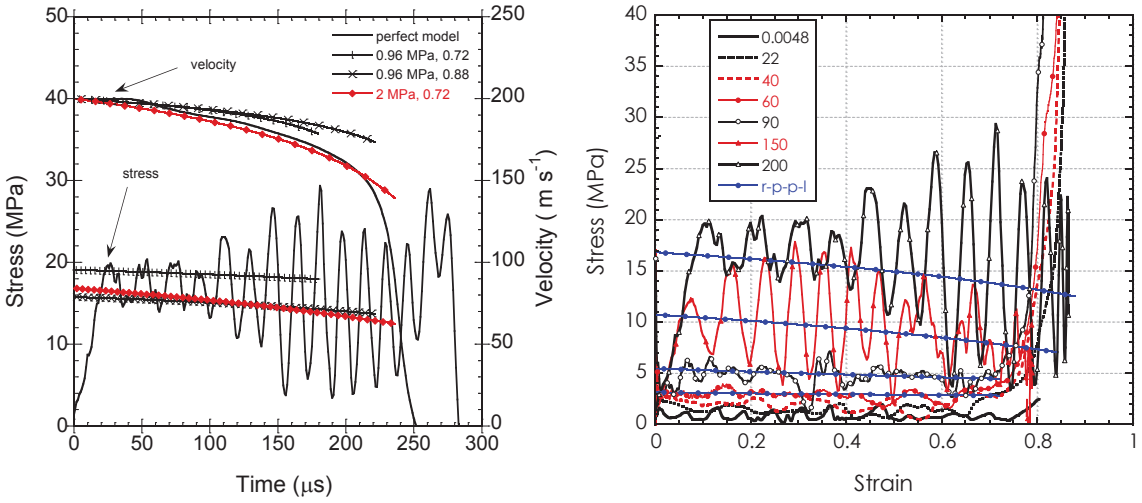


(c) (d)

Figure 6.11. (a) The perfect model II distal end stress-strain curves of direct impact tests until 90 m $s^{-1}$ and r-p-p-l prediction of stress-time profiles at (b) 90 and (c) 60 m $s^{-1}$ and (c) comparison r-p-p-l velocity-time profile with simulation velocity-time profile with simulation velocity-time profiles. (cont.)

In order to compare the peak pressures predicted by the r-p-p-l model, experiments and the perfect and imperfect models, the mean crushing stresses (plateau stress) of the experiments and models were determined. Since the impacted end layer is a free layer, the first initial peak stress is excluded in the determination of initial peak stress and plateau stress. Figure 6.12(a) shows the experimental stress-time graph at 150 m $s^{-1}$ together with the plateau stress, initial peak stress and valley stress. As seen in the same figure the second peak is taken as the initial peak stress and the following stress-drop as the initial valley stress. The plateau stress is determined at the flat part of the mean stress corresponding to the collapse of three layers after the first layer. The variation of the experimental impact end initial peak and valley and plateau stress and distal end stress with the impact velocity are seen in Figure 6.12(b). In the same figure, the classical r-p-p-l (quasi-static plateau stress and densification strain) and modified (dynamic plateau stress and densification strain) model predictions of the impact stress are shown. Although, both classical and modified model stress predictions are higher than experimental plateau stress, both model predict very much similar crushing stress at relatively low velocities, while the classical model predicts a crushing stress very much higher than the experimental and modified model crushing stress at 200 m $s^{-1}$. The modified model crushing stress however shows perfect agreement with the perfect model II and two layer imperfect model crushing stress as depicted in Figure 6.12(c).

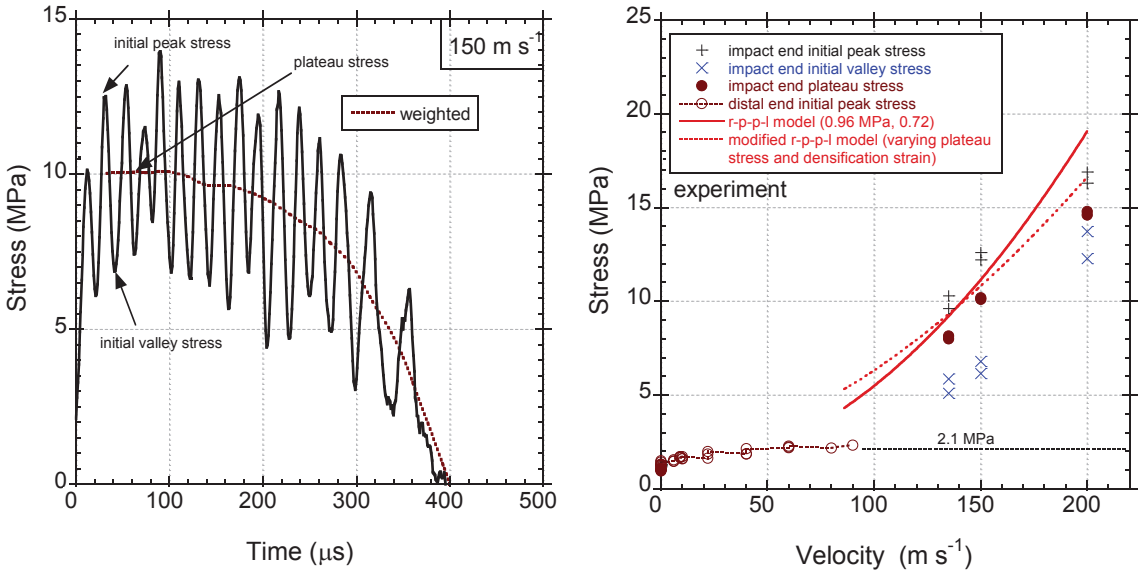


(a) (b)

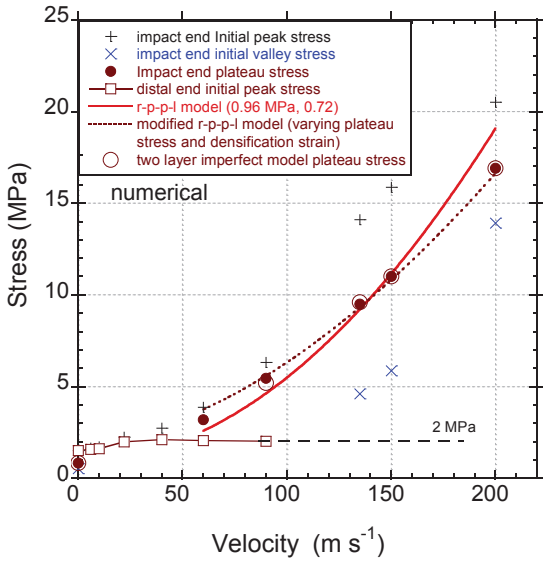


(c)

Figure 6.12. (a) the experimental stress-time graph at 150 m $s^{-1}$ (b) the classical r-p-p-l and modified model predictions of the impact stress for experimental results and (c) the classical r-p-p-l and modified model predictions of the impact stress for numerical results

# CHAPTER 7

# CONCLUSIONS

The compression impact deformation of a layered 1050 H14 aluminum corrugated sandwich structure were determined both experimentally and under low, intermediate and high velocities to investigate the validity of the perfect and imperfect models as function velocity and layer crushing profiles of the samples. The investigated sandwich corrugate core structure was made of multilayer corrugated layers (fins). The quasi-static compression test was performed at ~$5x10^{-3}$ $s^{-1}$, the Split Hopkinson Pressure Bar (SHPB) tests between 6 and 10 m $s^{-1}$, direct impact tests between 9 and 90 m $s^{-1}$ and Taylor-like impact tests at 135, 150 and 200 m $s^{-1}$. Three-dimensional finite element model of the tested specimens were developed using the LS-DYNA. The stress-time histories of the tests were verified by the simulations in the explicit finite element code of LS-DYNA. The perfect geometry model was coded as the perfect model I, fully bent fin wall model coded as the perfect model II, the model with the one layer bent fin coded as one layer imperfect model and the model with two layers of ben fin layers coded as the two layer imperfect model.

The localized deformation in quasi-static imperfect models started earlier from one of the imperfect layers and the layers initially compressed until about 0.4 strain were then compressed until about the densification strain gradually. The concurrent crushing of two or more layers observed in the experiments was also detected in the imperfect models. The localized deformation in the quasi-static perfect models; however, started at and near the specimen ends layers with the misalignments of the layers near the top and bottom of the specimen. Since the layer crushing in quasi-static experiments started from the mid-section layers of the weakest, the quasi-static crushing response of the tested structure was best approached by the imperfect models.

At increasing velocities from quasi-static velocity to 200 m $s^{-1}$, the tested corrugated structure showed three deformation modes. Between 0.0048 and 22 m $s^{-1}$ the deformation was quasi-static homogenous mode featured by the crushing bands formed randomly starting from the weakest fin layer and proceeded non-sequentially to uncrushed layers. The deformation mode between 22 and 60 m $s^{-1}$ was a transition mode

in which the layer crushing was concentrated at the impact end and the strain in the crushed layer was wider and did not reach the densification strain. Above 90 m $s^{-1}$, the deformation mode was a shock mode and the sample crushed sequentially layer by layer starting from the impact end and the crushed layer strain reached the densification strain. These observations were made based on the high speed camera records and model layer strain profiles.

The critical velocity for the shock formation calculated based on all the internal energy due to the loss of the kinetic energy, ~65 m $s^{-1}$, was well accord with the experimentally and numerically determined critical velocity for the shock formation. Experimentally a complete sequential crushing occurred at 90 m $s^{-1}$ and perfect model II resulted in near sequential and complete sequential crushing at 60 and 90 m $s^{-1}$, respectively.

The imperfect models one and two layer imperfect models, predicted the stress-time profile and layer deformation of the homogeneous and transition modes, while the imperfect and perfect models both approximated the stress-time profile and layer deformation of the shock mode. At high velocities, the layer crushing started from the impact end regardless the perfect of imperfect model used. Therefore, perfect and imperfect models resulted in similar initial stresses when the imperfect layer was located not at the front.

Layer strain profiles showed that as the velocity increased, the crushed layer densification strain increased. The numerical models of direct impact and direct impact experiments clearly showed that distal end crushing stress increased with increasing velocity. The increase of the stress within the homogeneous and transient mode velocities was ascribed to the micro-inertia effect and the tested corrugated structure showed a Type II behavior.

The critical velocity for the densification was calculated based on the varying plateau and densification strain. The critical velocity for the densification velocity was found between 100 m $s^{-1}$ and 165 m $s^{-1}$, which was well accord with the experiments.

The r-p-p-l model stress–strain and velocity-strain prediction using quasi-static plateau stress and densification strain and quasi-static plateau stress and numerically determined densification strain at that specific velocity resulted higher velocities and full densification, while the r-p-p-l model based on varying plateau stress and densification strain well predicted stress-strain and velocity strain profiles in the shock mode.

# REFERENCES


[1] D. Ruan, G. Lu, B. Wang, and T. X. Yu, "In-plane dynamic crushing of honeycombs - a finite element study," *International Journal of Impact Engineering,* vol. 28, pp. 161-182, Feb 2003.

[2] Z. J. Zheng, J. L. Yu, and J. R. Li, "Dynamic crushing of 2D cellular structures: A finite element study," *International Journal of Impact Engineering,* vol. 32, pp. 650-664, Dec 2005.

[3] Y. D. Liu, J. L. Yu, Z. J. Zheng, and J. R. Li, "A numerical study on the rate sensitivity of cellular metals," *International Journal of Solids and Structures,* vol. 46, pp. 3988-3998, Nov 2009.

[4] Z. Zou, S. R. Reid, P. J. Tan, S. Li, and J. J. Harrigan, "Dynamic crushing of honeycombs and features of shock fronts," *International Journal of Impact Engineering,* vol. 36, pp. 165-176, Jan 2009.

[5] S. Lee, F. Barthelat, J. W. Hutchinson, and H. D. Espinosa, "Dynamic failure of metallic pyramidal truss core materials - Experiments and modeling," *International Journal of Plasticity,* vol. 22, pp. 2118-2145, 2006.

[6] P. J. Tan, S. R. Reid, J. J. Harrigan, Z. Zou, and S. Li, "Dynamic compressive strength properties of aluminium foams. Part I - experimental data and observations," *Journal of the Mechanics and Physics of Solids,* vol. 53, pp. 2174-2205, Oct 2005.

[7] S. R. Reid and C. Peng, "Dynamic uniaxial crushing of wood," *International Journal of Impact Engineering,* vol. 19, pp. 531-570, May-Jul 1997.

[8] J. J. Harrigan, S. R. Reid, P. J. Tan, and T. Y. Reddy, "High rate crushing of wood along the grain," *International Journal of Mechanical Sciences,* vol. 47, pp. 521-544, Apr-May 2005.

[9] A. Chen, H. Kim, R. J. Asaro, and J. Bezares, "Non-explosive simulated blast loading of balsa core sandwich composite beams," *Composite Structures,* vol. 93, pp. 2768-2784, 2011.

[10] D. D. Radford, V. S. Deshpande, and N. A. Fleck, "The use of metal foam projectiles to simulate shock loading on a structure," *International Journal of Impact Engineering,* vol. 31, pp. 1152-1171, 2005.

[11] I. K. Odac, M. Guden, C. Klcaslan, and A. Tasdemirci, "The varying densification strain in a multi-layer aluminum corrugate structure: Direct impact testing and layer-wise numerical modelling," *International Journal of Impact Engineering,* vol. 103, pp. 64-75, May 2017.

[12] P. J. Tan, S. R. Reid, J. J. Harrigan, Z. Zou, and S. Li, "Dynamic compressive strength properties of aluminium foams. Part II - 'shock' theory and comparison with experimental data and numerical models," *Journal of the Mechanics and Physics of Solids,* vol. 53, pp. 2206-2230, Oct 2005.

[13] P. J. Tan, J. J. Harrigan, and S. R. Reid, "Inertia effects in uniaxial dynamic compression of a closed cell aluminium alloy foam," *Materials Science and Technology,* vol. 18, pp. 480-488, May 2002.

[14] P. J. Tan, S. R. Reid, and J. J. Harrigan, "On the dynamic mechanical properties of open-cell metal foams - A re-assessment of the 'simple-shock theory'," *International Journal of Solids and Structures,* vol. 49, pp. 2744-2753, Oct 2012.

[15] A. T. Barnes, K. Ravi-Chandar, S. Kyriakides, and S. Gaitanaros, "Dynamic crushing of aluminum foams: Part I - Experiments," *International Journal of Solids and Structures,* vol. 51, pp. 1631-1645, May 2014.

[16] S. Gaitanaros and S. Kyriakides, "Dynamic crushing of aluminum foams: Part II - Analysis," *International Journal of Solids and Structures,* vol. 51, pp. 1646-1661, May 2014.

[17] S. Gaitanaros and S. Kyriakides, "On the effect of relative density on the crushing and energy absorption of open-cell foams under impact," *International Journal of Impact Engineering,* vol. 82, pp. 3-13, Aug 2015.

[18] P. W. Zhang, Z. H. Wang, and L. M. Zhao, "Dynamic crushing behavior of open-cell aluminum foam with negative Poisson's ratio," *Applied Physics a-Materials Science & Processing,* vol. 123, p. 11, May 2017.

[19] S. L. Wang, Y. Y. Ding, C. F. Wang, Z. J. Zheng, and J. L. Yu, "Dynamic material parameters of closed-cell foams under high-velocity impact," *International Journal of Impact Engineering,* vol. 99, pp. 111-121, Jan 2017.

[20] H. Liu, Z. Q. Zhang, H. Liu, J. L. Yang, and H. Lin, "Theoretical investigation on impact resistance and energy absorption of foams with nonlinearly varying density," *Composites Part B-Engineering,* vol. 116, pp. 76-88, May 2017.

[21] B. Y. Zhang, Y. F. Lin, S. Li, D. X. Zhai, and G. H. Wu, "Quasi-static and high strain rates compressive behavior of aluminum matrix syntactic foams," *Composites Part B-Engineering,* vol. 98, pp. 288-296, Aug 2016.

[22] H. Liu, Z. Q. Zhang, H. Liu, and J. L. Yang, "Effect of elastic target on Taylor-Hopkinson impact of low-density foam material," *International Journal of Impact Engineering,* vol. 94, pp. 109-119, Aug 2016.

[23] V. S. Deshpande and N. A. Fleck, "High strain rate compressive behaviour of aluminium alloy foams," *International Journal of Impact Engineering,* vol. 24, pp. 277-298, Mar 2000.

[24] S. L. Lopatnikov, B. A. Gama, M. J. Haque, C. Krauthauser, J. W. Gillespie, M. Guden*, et al.*, "Dynamics of metal foam deformation during Taylor cylinder-Hopkinson bar impact experiment," *Composite Structures,* vol. 61, pp. 61-71, Jul-Aug 2003.

[25] I. Elnasri, S. Pattofatto, H. Zhao, H. Tsitsiris, F. Hild, and Y. Girard, "Shock enhancement of cellular structures under impact loading: Part I experiments," *Journal of the Mechanics and Physics of Solids,* vol. 55, pp. 2652-2671, Dec 2007.

[26] H. Liu, Z. K. Cao, G. C. Yao, H. J. Luo, and G. Y. Zu, "Performance of aluminum foam–steel panel sandwich composites subjected to blast loading," *Materials & Design,* vol. 47, pp. 483-488, 2013.

[27] H. Zhao and G. Gary, "Crushing behaviour of aluminium honeycombs under impact loading," *International Journal of Impact Engineering,* vol. 21, pp. 827-836, Nov 1998.

[28] D. H. Zhang, Q. G. Fei, and P. W. Zhang, "In-plane dynamic crushing behavior and energy absorption of honeycombs with a novel type of multi-cells," *Thin-Walled Structures,* vol. 117, pp. 199-210, Aug 2017.

[29] J. X. Qiao and C. Q. Chen, "In-plane crushing of a hierarchical honeycomb," *International Journal of Solids and Structures,* vol. 85-86, pp. 57-66, May 2016.

[30] Y. Tao, M. J. Chen, H. S. Chen, Y. M. Pei, and D. N. Fang, "Strain rate effect on the out-of-plane dynamic compressive behavior of metallic honeycombs: Experiment and theory," *Composite Structures,* vol. 132, pp. 644-651, Nov 2015.

[31] S. F. Liao, Z. J. Zheng, and J. L. Yu, "Dynamic crushing of 2D cellular structures: Local strain field and shock wave velocity," *International Journal of Impact Engineering,* vol. 57, pp. 7-16, Jul 2013.

[32] S. Heimbs, "Virtual testing of sandwich core structures using dynamic finite element simulations," *Computational Materials Science,* vol. 45, pp. 205-216, Apr 2009.

[33] D. Asprone, F. Auricchio, C. Menna, S. Morganti, A. Prota, and A. Reali, "Statistical finite element analysis of the buckling behavior of honeycomb structures," *Composite Structures,* vol. 105, pp. 240-255, 2013/11/01/ 2013.

[34] H. Kanahashi, T. Mukai, Y. Yamada, K. Shimojima, M. Mabuchi, T. G. Nieh*, et al.*, "Dynamic compression of an ultra-low density aluminium foam," *Materials Science and Engineering a-Structural Materials Properties Microstructure and Processing,* vol. 280, pp. 349-353, Mar 2000.

[35] J. L. Grenestedt, "On interactions between imperfections in cellular solids," *Journal of Materials Science,* vol. 40, pp. 5853-5857, Nov 2005.

[36] K. Li, X. L. Gao, and J. Wang, "Dynamic crushing behavior of honeycomb structures with irregular cell shapes and non-uniform cell wall thickness," *International Journal of Solids and Structures,* vol. 44, pp. 5003-5026, Jul 2007.

[37] X. C. Zhang, Y. Liu, B. Wang, and Z. M. Zhang, "Effects of defects on the in-plane dynamic crushing of metal honeycombs," *International Journal of Mechanical Sciences,* vol. 52, pp. 1290-1298, Oct 2010.

[38] C. Kilicaslan, M. Guden, I. K. Odaci, and A. Tasdemirci, "The impact responses and the finite element modeling of layered trapezoidal corrugated aluminum core and aluminum sheet interlayer sandwich structures," *Materials & Design,* vol. 46, pp. 121-133, Apr 2013.

[39] C. Kilicaslan, M. Guden, I. K. Odaci, and A. Tasdemirci, "Experimental and numerical studies on the quasi-static and dynamic crushing responses of multi-layer trapezoidal aluminum corrugated sandwiches," *Thin-Walled Structures,* vol. 78, pp. 70-78, May 2014.

[40] Gibson and Ashby, *Cellular Solids: Structure and Properties*. Cambridge: Cambridge University Press 1997.

[41] A. G. Evans, J. W. Hutchinson, and M. F. Ashby, "Multifunctionality of cellular metal systems," *Progress in Materials Science,* vol. 43, pp. 171-221, 1998.

[42] A. G. Evans, J. W. Hutchinson, N. A. Fleck, M. F. Ashby, and H. N. G. Wadley, "The topological design of multifunctional cellular metals," *Progress in Materials Science,* vol. 46, pp. 309-327, 2001.

[43] H. N. G. Wadley, "Multifunctional periodic cellular metals," *Philosophical Transactions of the Royal Society a-Mathematical Physical and Engineering Sciences,* vol. 364, pp. 31-68, Jan 2006.

[44] D. D. Radford, G. J. McShane, V. S. Deshpande, and N. A. Fleck, "The response of clamped sandwich plates with metallic foam cores to simulated blast loading," *International Journal of Solids and Structures,* vol. 43, pp. 2243-2259, Apr 2006.

[45] K. P. Dharmasena, H. N. G. Wadley, Z. Y. Xue, and J. W. Hutchinson, "Mechanical response of metallic honeycomb sandwich panel structures to high-intensity dynamic loading," *International Journal of Impact Engineering,* vol. 35, pp. 1063-1074, Sep 2008.

[46] C. Kilicaslan, I. K. Odaci, and M. Gueden, "Single- and double-layer aluminum corrugated core sandwiches under quasi-static and dynamic loadings," *Journal of Sandwich Structures & Materials,* vol. 18, pp. 667-692, Nov 2016.

[47] C. Kilicaslan, I. K. Odaci, A. Tasdemirci, and M. Guden, "Experimental Testing and Full and Homogenized Numerical Models of the Low Velocity and Dynamic Deformation of the Trapezoidal Aluminium Corrugated Core Sandwich," *Strain,* vol. 50, pp. 236-249, Jun 2014.

[48] E. Andrews, W. Sanders, and L. J. Gibson, "Compressive and tensile behaviour of aluminum foams," *Materials Science and Engineering a-Structural Materials Properties Microstructure and Processing,* vol. 270, pp. 113-124, Sep 1999.

[49] E. Wu and W. S. Jiang, "Axial crush of metallic honeycombs," *International Journal of Impact Engineering,* vol. 19, pp. 439-456, May-Jul 1997.

[50] J. J. Harrigan, S. R. Reid, and C. Peng, "Inertia effects in impact energy absorbing materials and structures," *International Journal of Impact Engineering,* vol. 22, pp. 955-979, Oct-Nov 1999.

[51] I. W. Hall, M. Guden, and C. J. Yu, "Crushing of aluminum closed cell foams: Density and strain rate effects," *Scripta Materialia,* vol. 43, pp. 515-521, Aug 2000.

[52] A. Honig and W. J. Stronge, "In-plane dynamic crushing of honeycomb. Part I: crush band initiation and wave trapping," *International Journal of Mechanical Sciences,* vol. 44, pp. 1665-1696, Aug 2002.

[53] H. Zhao, I. Elnasri, and S. Abdennadher, "An experimental study on the behaviour under impact loading of metallic cellular materials," *International Journal of Mechanical Sciences,* vol. 47, pp. 757-774, Apr-May 2005.

[54] H. Zhao, I. Elnasri, and H. J. Li, "The mechanism of strength enhancement under impact loading of cellular materials," *Advanced Engineering Materials,* vol. 8, pp. 877-883, Sep 2006.

[55] S. Pattofatto, I. Elnasri, H. Zhao, H. Tsitsiris, F. Hild, and Y. Girard, "Shock enhancement of cellular structures under impact loading: Part II analysis," *Journal of the Mechanics and Physics of Solids,* vol. 55, pp. 2672-2686, Dec 2007.

[56] D. Karagiozova, G. S. Langdon, and G. N. Nurick, "Propagation of compaction waves in metal foams exhibiting strain hardening," *International Journal of Solids and Structures,* vol. 49, pp. 2763-2777, Oct 2012.

[57] Z. J. Zheng, Y. D. Liu, J. L. Yu, and S. R. Reid, "Dynamic crushing of cellular materials: Continuum-based wave models for the transitional and shock modes," *International Journal of Impact Engineering,* vol. 42, pp. 66-79, Apr 2012.

[58] P. F. Wang, S. L. Xu, Z. B. Li, J. L. Yang, C. Zhang, H. Zheng*, et al.*, "Experimental investigation on the strain-rate effect and inertia effect of closed-cell aluminum foam subjected to dynamic loading," *Materials Science and Engineering a-Structural Materials Properties Microstructure and Processing,* vol. 620, pp. 253-261, Jan 2015.

[59] Y. Alvandi-Tabrizi, D. A. Whisler, H. Kim, and A. Rabiei, "High strain rate behavior of composite metal foams," *Materials Science and Engineering a-Structural Materials Properties Microstructure and Processing,* vol. 631, pp. 248-257, Apr 2015.

[60] A. Jung, A. D. Pullen, and W. G. Proud, "Strain-rate effects in Ni/Al composite metal foams from quasi-static to low-velocity impact behaviour," *Composites Part a-Applied Science and Manufacturing,* vol. 85, pp. 1-11, Jun 2016.

[61] K. Myers, B. Katona, P. Cortes, and I. N. Orbulov, "Quasi-static and high strain rate response of aluminum matrix syntactic foams under compression," *Composites Part a-Applied Science and Manufacturing,* vol. 79, pp. 82-91, Dec 2015.

[62] J. Zhang, G. P. Zhao, T. J. Lu, and S. Y. He, "Strain Rate Behavior of Closed-Cell Al-Si-Ti Foams: Experiment and Numerical Modeling," *Mechanics of Advanced Materials and Structures,* vol. 22, pp. 556-563, 2015.

[63] Lindholm US, Bessey RL, and S. GV., "Effect of strain rate on yield strength, tensile strength and elongation of three aluminium alloys.," *J Mater JMLSA,* vol. 6, p. 119, 1971.

[64] O. Sadot, O. Ram, I. Anteby, S. Gruntman, and G. Ben-Dor, "The trapped gas effect on the dynamic compressive strength of light aluminum foams," *Materials Science and Engineering a-Structural Materials Properties Microstructure and Processing,* vol. 659, pp. 278-286, Apr 2016.

[65] C. R. Calladine and R. W. English, "STRAIN-RATE AND INERTIA EFFECTS IN THE COLLAPSE OF 2 TYPES OF ENERGY-ABSORBING STRUCTURE," *International Journal of Mechanical Sciences,* vol. 26, pp. 689-&, 1984.

[66] M. Langseth and O. S. Hopperstad, "Static and dynamic axial crushing of square thin-walled aluminium extrusions," *International Journal of Impact Engineering,* vol. 18, pp. 949-968, Oct-Dec 1996.

[67] A. Paul and U. Ramamurty, "Strain rate sensitivity of a closed-cell aluminum foam," *Materials Science and Engineering a-Structural Materials Properties Microstructure and Processing,* vol. 281, pp. 1-7, Apr 2000.

[68] V. L. Tagarielli, V. S. Deshpande, and N. A. Fleck, "The high strain rate response of PVC foams and end-grain balsa wood," *Composites Part B-Engineering,* vol. 39, pp. 83-91, 2008.

[69] M. T. Tilbrook, D. D. Radford, V. S. Deshpande, and N. A. Fleck, "Dynamic crushing of sandwich panels with prismatic lattice cores," *International Journal of Solids and Structures,* vol. 44, pp. 6101-6123, Sep 2007.

[70] Y. C. Zhang, S. L. Zhang, and Z. L. Wang, "Crush Behavior of Corrugated Cores Sandwich Panels," in *High Performance Structures and Materials Engineering, Pts 1 and 2*. vol. 217-218, M. Zhou, Ed., ed Durnten-Zurich: Trans Tech Publications Ltd, 2011, pp. 1584-+.

[71] L. L. Tam and C. R. Calladine, "INERTIA AND STRAIN-RATE EFFECTS IN A SIMPLE PLATE-STRUCTURE UNDER IMPACT LOADING," *International Journal of Impact Engineering,* vol. 11, pp. 349-377, 1991.

[72] X. Y. Su, T. X. Yu, and S. R. Reid, "INERTIA-SENSITIVE IMPACT ENERGY-ABSORBING STRUCTURES .2. EFFECT OF STRAIN-RATE," *International Journal of Impact Engineering,* vol. 16, pp. 673-689, Aug 1995.

[73] X. Y. Su, T. X. Yu, and S. R. Reid, "INERTIA-SENSITIVE IMPACT ENERGY-ABSORBING STRUCTURES .1. EFFECTS OF INERTIA AND ELASTICITY," *International Journal of Impact Engineering,* vol. 16, pp. 651-672, Aug 1995.

[74] D. G. Vaughn, J. M. Canning, and J. W. Hutchinson, "Coupled plastic wave propagation and column buckling," *Journal of Applied Mechanics-Transactions of the Asme,* vol. 72, pp. 139-146, Jan 2005.

[75] H. Kolsky, " An Investigation of the Mechanical Properties of Materials at Very High Rates of Loading," *Proceedings of the Physical Society Section B,* vol. 62(11), pp. 676-700, 1949.

[76] B. Hopkinson, "A method of measuring the pressure produced in the detonation of high explosives or by the impact of bullets,". *Phil. Trans. R. Soc. Lond. A. ,* vol. 213, pp. 437-456 1914.

[77] H. Couque, "The use of the direct impact Hopkinson pressure bar technique to describe thermally activated and viscous regimes of metallic materials," *Philosophical Transactions of the Royal Society a-Mathematical Physical and Engineering Sciences,* vol. 372, p. 10, Aug 2014.

[78] R. Gumruk and S. Karadeniz, "A numerical study of the influence of bump type triggers on the axial crushing of top hat thin-walled sections," *Thin-Walled Structures,* vol. 46, pp. 1094-1106, Oct 2008.

[79] G. R. Johnson and C. W.H., "A constitutive model and data for metals subjected to large strains, high strain rates and high temperatures " in *Proceedings of the 7th International Symposium on Ballistics,*, The Hague, The Netherlands, 1983, p. 541.

[80] C. Kılıçaslan, M. Güden, İ. K. Odacı, and A. Taşdemirci, "The impact responses and the finite element modeling of layered trapezoidal corrugated aluminum core and aluminum sheet interlayer sandwich structures," *Materials & Design,* vol. 46, pp. 121-133, 2013.

[81] S. P. Santosa, T. Wierzbicki, A. G. Hanssen, and M. Langseth, "Experimental and numerical studies of foam-filled sections," *International Journal of Impact Engineering,* vol. 24, pp. 509-534, May 2000.